

Studies of Phonon Anharmonicity in Solids

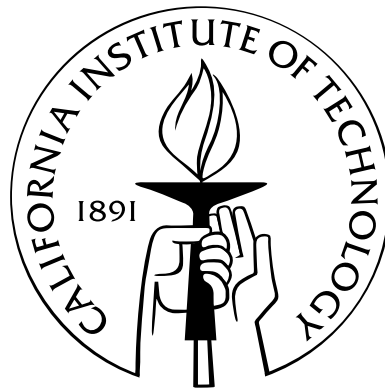
Thesis by

Tian Lan

In Partial Fulfillment of the Requirements

for the Degree of

Doctor of Philosophy



California Institute of Technology

Pasadena, California

2014

(Defended May 6, 2014)

Acknowledgements

It is almost mission impossible to express my gratitude to all the wonderful people I have had the pleasure of meeting and knowing during my time at Caltech.

I have been so fortunate to have Brent Fultz as my research advisor. Brent has provided enormous encouragement, guidance, patience and support for my study. This work would not have been possible without his mentorship.

I appreciate the support from my committee: Bill Johnson, Bill Goddard, George Rossman, Keith Schwab and Rudy Marcus. In particular, I thank George for his guidance in my experimental work and kindness in sharing with me wonderful equipments from his lab.

I would like to thank all current and former members of the Fultz group, who have been a constant source of thoughts and support: Olivier Delaire, Jiao Lin, Channing Ahn, Hongjin Tan, Xiaoli Tang, Jorge Muñoz, Nick Stadie, David Abrecht, Lisa Mauger, Hillary Smith, Sally Tracy, Dennis Kim, Max Murialdo, Jane Herriman, and Nick Weadock. Special thanks to Chen Li, who gave me the initiation class on Raman spectrometry and computational physics.

I also wish to thank all the members of the Caltech community who have helped me over the years: especially, Sandra Troian, for her support when I met difficulties in the beginning of my graduate research; Mike Vondrus, for his dexterousness in building the crazy things I designed; Avalon Johnson, for maintaining the group cluster, and helping me solve problems in running the computation scripts; Ali Ghaffari, for teaching me nano-fabrication; Qi An, for his informative suggestions about first principles calculations; Pam Albertson and many other staff in Department of Applied Physics and Materials Science, for their efforts to keep everything

running.

I wish to acknowledge the generous help and support of our collaborators at Oak Ridge National Laboratory: Doug Abernathy, Jen Niedziela and Matthew Stone, among many others. They made our inelastic neutron scattering experiments possible.

Finally, I wish to express my gratitude to my dear family, my parents, Jiasheng and Fang, and my wife, Zhaoyan, for their unconditional support and love through the years. And Raymond, you bring us the paramount joy.

Abstract

Today our understanding of the vibrational thermodynamics of materials at low temperatures is emerging nicely, based on the harmonic model in which phonons are independent. At high temperatures, however, this understanding must accommodate how phonons interact with other phonons or with other excitations. We shall see that the phonon-phonon interactions give rise to interesting coupling problems, and essentially modify the equilibrium and non-equilibrium properties of materials, e.g., thermodynamic stability, heat capacity, optical properties and thermal transport of materials. Despite its great importance, to date the anharmonic lattice dynamics is poorly understood and most studies on lattice dynamics still rely on the harmonic or quasiharmonic models. There have been very few studies on the pure phonon anharmonicity and phonon-phonon interactions. The work presented in this thesis is devoted to the development of experimental and computational methods on this subject.

Modern inelastic scattering techniques with neutrons or photons are ideal for sorting out the anharmonic contribution. Analysis of the experimental data can generate vibrational spectra of the materials, i.e., their phonon densities of states or phonon dispersion relations. We obtained high quality data from laser Raman spectrometer, Fourier transform infrared spectrometer and inelastic neutron spectrometer. With accurate phonon spectra data, we obtained the energy shifts and lifetime broadenings of the interacting phonons, and the vibrational entropies of different materials. The understanding of them then relies on the development of the fundamental theories and the computational methods.

We developed an efficient post-processor for analyzing the anharmonic vibra-

tions from the molecular dynamics (MD) calculations. Currently, most first principles methods are not capable of dealing with strong anharmonicity, because the interactions of phonons are ignored at finite temperatures. Our method adopts the Fourier transformed velocity autocorrelation method to handle the big data of time-dependent atomic velocities from MD calculations, and efficiently reconstructs the phonon DOS and phonon dispersion relations. Our calculations can reproduce the phonon frequency shifts and lifetime broadenings very well at various temperatures.

To understand non-harmonic interactions in a microscopic way, we have developed a numerical fitting method to analyze the decay channels of phonon-phonon interactions. Based on the quantum perturbation theory of many-body interactions, this method is used to calculate the three-phonon and four-phonon kinematics subject to the conservation of energy and momentum, taking into account the weight of phonon couplings. We can assess the strengths of phonon-phonon interactions of different channels and anharmonic orders with the calculated two-phonon DOS. This method, with high computational efficiency, is a promising direction to advance our understandings of non-harmonic lattice dynamics and thermal transport properties.

These experimental techniques and theoretical methods have been successfully performed in the study of anharmonic behaviors of metal oxides, including rutile and cuprite structures, and will be discussed in detail in Chapters 4 to 6. For example, for rutile titanium dioxide (TiO_2), we found that the anomalous anharmonic behavior of the B_{1g} mode can be explained by the volume effects on quasiharmonic force constants, and by the explicit cubic and quartic anharmonicity. For rutile tin dioxide (SnO_2), the broadening of the B_{2g} mode with temperature showed an unusual concave downwards curvature. This curvature was caused by a change with temperature in the number of down-conversion decay channels, originating with the wide band gap in the phonon dispersions. For silver oxide (Ag_2O), strong anharmonic effects were found for both phonons and for the negative thermal expansion.

Contents

Acknowledgements	iii
Abstract	v
1 Lattice Dynamics and Phonon-Phonon Interactions	1
1.1 Bravais Lattices	2
1.2 Harmonic Lattice Dynamics	3
1.3 Quasiharmonic Approximation	5
1.4 Anharmonic Lattice Dynamics	6
1.5 Green's Function Method	7
1.5.1 The Retarded Green's Function and Lehmann Representation	7
1.5.2 Perturbation Theory and Wick's Theorem For Finite Temperatures	9
1.6 Phonon-Phonon Interactions and Phonon Lifetime	13
1.7 Self-Consistent Lattice Dynamics	15
2 Experimental Methods	17
2.1 Raman Scattering	18
2.1.1 Introduction	18
2.1.2 The Frequency Resolved Raman Spectroscopy	19
2.1.2.1 Classical Theory	19
2.1.2.2 Quantum Theory and Placzek's Approximation	21
2.1.2.3 Loudon's Third Order Perturbation Theory	25
2.1.3 Group Theory and Selection Rules	27

2.1.3.1	Classical Approach	27
2.1.3.2	Group Theoretical Approach	28
2.1.3.3	The Correlation Method	30
2.2	Time of Flight Inelastic Neutron Scattering	33
2.2.1	Introduction	33
2.2.2	Basic Principles	33
2.2.2.1	Scattering Cross Section	33
2.2.2.2	Coherent and Incoherent Scattering	34
2.2.3	Wide Angular-Range Chopper Spectrometer (ARCS)	36
2.2.4	Data Reduction	37
3	Computational Methodologies	39
3.1	Density Functional Theory	40
3.1.1	Introduction	40
3.1.2	Hohenberg-Kohn Theorems	40
3.1.3	Kohn-Sham Theory	41
3.1.4	Functionals for Exchange and Correlation	42
3.1.5	Pseudopotentials	44
3.2	Molecular Dynamics Methods	45
3.2.1	Introduction	45
3.2.2	Solving Equations of Motion	46
3.2.3	Ensembles	47
3.3	Phonon Calculations	48
3.3.1	Introduction	48
3.3.2	Lattice Dynamics Approach	48
3.3.2.1	Small Displacement Method	48
3.3.2.2	Density Functional Perturbation Method	50
3.3.3	Molecular Dynamics Approach	51
3.3.3.1	Time-Correlation Method	51
3.3.3.2	Fourier-Transformed Velocity Autocorrelation Method	52

3.4	Anharmonic Fitting Algorithm	55
4	Phonon Anharmonicity of Rutile TiO₂	57
4.1	Introduction	58
4.2	Experiments	60
4.3	Molecular Dynamics Calculations	61
4.4	Results	63
4.4.1	Experiment	63
4.4.2	MD Simulations	66
4.5	Experimental Data Analysis	67
4.5.1	Analysis of Quasiharmonicity and Anharmonicity	67
4.5.2	Analysis of Cubic and Quartic Anharmonicity	70
4.6	Discussion	80
4.6.1	Anharmonicities from Experimental Trends	80
4.6.2	Anharmonicities from MD Simulations	82
4.6.3	Vibrational Entropy of Rutile TiO ₂	89
4.7	Conclusions	90
5	Phonon Anharmonicity of Rutile SnO₂	92
5.1	Introduction	93
5.2	Experimental Procedures	95
5.3	Results	96
5.4	Calculations	100
5.4.1	First Principles Lattice Dynamics	100
5.4.2	The Kinematic Functionals $D^\omega(\Omega)$ and $P^\omega(\Omega)$	102
5.5	Analysis	103
5.5.1	Separating Anharmonicity from Quasiharmonicity	103
5.5.2	Cubic and Quartic Anharmonicity	105
5.6	Discussion	110
5.7	Conclusions	112

6	Phonon Anharmonicity of Ag₂O with Cuprite Structure	113
6.1	Introduction	114
6.2	Experiments	118
6.2.1	Inelastic Neutron Scattering	118
6.2.2	Fourier Transform Far-Infrared Spectrometer	118
6.2.3	Results	120
6.3	First-Principles Molecular Dynamics Simulations	121
6.3.1	Methods	121
6.3.2	Results	126
6.4	Anharmonic Perturbation Theory	131
6.4.1	Computational Methodology	131
6.4.2	Results	132
6.5	Discussion	135
6.5.1	Quasiharmonic Approximation	135
6.5.2	Negative Thermal Expansion	139
6.5.3	Explicit Anharmonicity	140
6.6	Conclusions	141
7	Conclusions	143
7.1	Summary	143
7.2	Future Work	145
A	The evaluation of the 2nd order Feynman diagram of phonon-phonon interactions	150
B	The Correlation method: an example for Ag₂O with cuprite structure	154
C	Raman spectra of two-phase and solid solution phase of Li_{0.6}FePO₄ at elevated temperatures	158
	Bibliography	161

List of Figures

1.1	Dyson's equation	12
1.2	The lowest order terms of the proper self energy	13
2.1	Schematic energy level diagram showing the states involved in Raman signal.	24
2.2	Schematic overview of the ARCS design with components labeled [13]	37
3.1	The flow chart implementing the Fourier-transformed velocity auto-correlation method	55
4.1	Rutile structure and oxygen atom displacements for Raman-active modes.	60
4.2	Raman spectra of rutile TiO ₂ at selected temperatures from 100 K to 1150 K.	64
4.3	Temperature dependence of (a) frequency shifts, (b) FWHM, of the Raman modes B_{1g} , E_g and A_{1g} . Data of Ref. [[59]] are shown as open triangles in panel a.	65
4.4	(a) The B_{1g} Raman peak calculated from the velocity trajectories of MD simulations, at temperatures as labeled and constant pressure of 0 GPa, and at pressures from 0 to 6 GPa at 300 K. (b) Calculated E_g Raman peak, and (c) Calculated A_{1g} Raman peak at temperatures as labeled and constant pressure of 0 GPa. Solid red curves are the Lorentzian fits.	68

- 4.5 (a) Two-phonon density of states $D(\Omega)$ of Eq. 4.9 for 300 K (black) and 1000 K (red). The up-conversion and down-conversion contributions to $D(\Omega)$ at 1000 K are shown in green dash and red dash curves, respectively. The overtone process at 1000 K is highlighted as the filled area under the blue curve. (b) $P(\Omega)$ of Eq. 5.2 at 300 K (black) and 1000 K (red). 76
- 4.6 Temperature dependence of parameters for fittings to Raman peaks of mode B_{1g} (a) frequency shift, and (b) FWHM. Solid circles are experimental data. Solid curves are the fittings of the experimental points to Eq. 4.5 and Eq. 4.11d. Dotted line is the quasiharmonic contribution to the frequency shift. Dash-dot line is the explicit anharmonicity $\omega_0 + \Delta^{(4)} + \Delta^{(3)}$, and dashed line is $\omega_0 + \Delta^{(3)}$ 77
- 4.7 Temperature dependence of parameters for fittings to Raman peaks of mode E_g (a) frequency shift, and (b) FWHM. Dotted line is the quasiharmonic contribution to the frequency shifts. Dash-dot line is the explicit anharmonicity $\omega_0 + \Delta^{(4)} + \Delta^{(3)}$ and dashed line is $\omega_0 + \Delta^{(3)}$. 78
- 4.8 Temperature dependence of parameters for fittings to Raman peaks of mode A_{1g} (a) frequency shift, and (b)FWHM. Dotted line represents the quasiharmonic contribution to the frequency shifts. Dash-dot line is the explicit anharmonicity $\omega_0 + \Delta^{(4)} + \Delta^{(3)} + \Delta^{(3')}$, short dash line corresponds to $\omega_0 + \Delta^{(3)} + \Delta^{(3')}$ and dashed line is $\omega_0 + \Delta^{(3)}$ 79
- 4.9 (a) Temperature dependent frequency shift, (b) FWHM broadening, and (c) pressure dependent frequency shift, of the B_{1g} mode from MD calculations (red), compared with experiment data (black). 84

4.10	Frozen phonon potential of the B_{1g} mode calculated with the MW shell model, and its response to the volume increase (indicated as the dash arrow). The potential is decomposed into the harmonic component and quartic component. The three potentials are for lattice parameters corresponding to 300 K at 0 GPa (black), 300 K at 6 GPa (blue), and 800 K at 0 GPa (red). The inset shows the B_{1g} mode of rutile TiO_2 structure projected along the c-axis. Small arrows indicate the polarization vectors of this mode.	86
4.11	Temperature dependence of the (a) frequency shift, and (b) FWHM broadening, of the E_g mode from MD simulations (red) and experimental data (black).	87
4.12	Temperature dependence of the (a) frequency shift, and (b) FWHM broadening, of the A_{1g} mode from MD simulations (red) and experimental data (black).	88
4.13	Ratio of the mode anharmonic potential and harmonic potential, with increasing temperature.	89
5.1	Rutile structure and oxygen atom displacements for Raman-active modes.	94
5.2	Raman spectra of powder samples of rutile SnO_2 at selected temperatures.	98
5.3	Temperature dependence of (a) frequency shifts, (b) breadths as FWHMs, of the Raman modes E_g , A_{1g} and B_{2g} . The solid and open symbols represent the experimental data from powder and single crystal samples, respectively. Solid curves are the theoretical fittings with a full calculation of the kinematics of three- phonon and four-phonon processes. The dashed curve was calculated without considering the frequency dependence of $D_{0\downarrow}(\Omega)$, the number of decay channels, at elevated temperatures.	99

- 5.4 (a) Calculated phonon dispersion along high symmetry directions of rutile SnO_2 . Γ (0, 0, 0), X (0.5, 0, 0), M (0.5, 0.5, 0), Z (0, 0, 0.5), R (0.5, 0, 0.5) and A (0.5, 0.5, 0.5). At the Γ point, the frequencies from Table 6.1 are presented as up triangles (Raman) and down triangles (infrared). At the X , M , Z , R and A points, the mode frequencies from Ref. [[103]] (all doubly degenerate) are presented as squares. (b) Total phonon DOS (black curve) and oxygen-projected DOS (filled green). 102
- 5.5 (a) Two-phonon density of states $D^\omega(\Omega)$ for 0 K and 800 K. The arrowheads mark the positions of the three Raman modes, E_g , A_{1g} and B_{2g} , respectively. The up-conversion and down-conversion contributions at 800 K are shown in green and black dash curves, respectively. There is no up-conversion process at 0 K. (b) $P^\omega(\Omega)$ at 800 K. 108
- 5.6 Fittings of the temperature dependence of frequency shift of (a) the E_g mode, (b) the A_{1g} mode and (c) the B_{2g} mode. Solid curves are the final fittings to $\Delta^Q + \Delta^{(3)} + \Delta^{(3')} + \Delta^{(4)}$. Different contributions are indicated individually in these figures. 109
- 6.1 Cuprite structure of Ag_2O , showing standard cubic fcc unit cell and O-Ag-O links that pass between cubes. 115
- 6.2 Neutron weighted phonon DOS of Ag_2O with the cuprite structure from ARCS experimental data (black dots) and MD simulations (red curves) at temperatures from 40 to 400 K. The dashed spectrum corresponds to the 40 K experimental result, shifted vertically for comparison at each temperature. Vertical dashed lines are aligned to the major peak centers at 40 K from experiments, and are numbered at top. The incident energy was 100 meV for panel (a), and 30 meV for panel (b). 119

6.3	Shifts of centers of peaks in the phonon DOS, relative to data at 40 K. The filled symbols are experimental data, open symbols (green) are from MD-based QHA calculations and solid curves (red) are from MD calculations. Indices 1, 2, 3 correspond to the peak labels in Fig. 6.2, and are also represented by the triangle, square and circle respectively for experimental data and QHA calculations.	120
6.4	(a) FT-IR absorption spectra of Ag_2O with the cuprite structure at 300 K. (b), (c) Enlargement of two bands at selected temperatures. . . .	122
6.5	The phonon densities of states for two different cells used in molecular dynamics simulations at 400 K.	125
6.6	The simulated phonon densities of states for 12, 18 and 30 ps at 40 K .	125
6.7	Temperature dependence of lattice parameter from experimental data in Ref. [[111]], quasiharmonic calculations and MD calculations, expressed as the relative changes with respect to their 40 K values, i.e., $a(T)/a(40\text{ K}) - 1$	127
6.8	Phonon modes simulated by MD and projected on the Γ -point, at temperatures and pressures as labeled. The normal-mode frequencies calculated from harmonic lattice dynamics are shown as vertical dashed lines in red. The group symmetry for each mode is shown at the bottom.	129
6.9	(a) Temperature dependent frequency shifts of the Ag-dominated $F_{1u}^{(1)}$ mode and the O-dominated F_{2g} and $F_{1u}^{(2)}$ modes from FT-IR (black), compared with the MD simulated peaks (red) such as in Fig. 6.8. (b) The lifetimes of the corresponding modes at temperatures from 40 to 400 K, from FT-IR (black) and the MD simulated peaks (red).	130
6.10	(a) Calculated phonon dispersion along high-symmetry directions of Ag_2O with the cuprite structure. $\Gamma(0,0,0)$, $M(0.5,0.5,0)$, $X(0.5,0,0)$, $R(0.5,0.5,0.5)$. (b) The TDOS spectra, $D(\omega)$, at 40 K (dashed) and 400 K (solid). The down-conversion and up-conversion contributions are presented separately as black and green curves, respectively. . . .	134

6.11	Temperature dependence of the inverse of the quality factors $1/Q$ for the $F_{1u}^{(1)}$, A_{2u} , F_{2g} and $F_{1u}^{(2)}$ phonon modes from FT-IR (black squares), MD calculations (red circles) and the theoretical fittings with a full calculation of the TDOS. The unit of the fitting parameter $ C_j^{(3)} ^2$ is 10^{-1} eV^{-1}	135
6.12	Neutron weighted phonon DOS of Ag_2O with the cuprite structure from MD simulations. The green spectrum is the MD simulated phonon DOS at 40 K and 0.45 GPa. Vertical dashed lines are aligned to the major peak centers at 40 K and labeled by numbers. The incident energy was 100 meV for panel (a), and 30 meV for panel (b). The spectra were convoluted with the resolution function characteristic of ARCS for the different energies of the incident neutron beam.	138
A.1	Contour of evaluation for energy sums	150
C.1	Raman spectra at elevated temperatures of two-phase $\text{Li}_{0.6}\text{FePO}_4$ (left panel) and solid solution phase quenched at 400 °C (right panel)	159
C.2	Raman spectra of two-phase $\text{Li}_{0.6}\text{FePO}_4$ right above the phase transition temperature at 260 °C but with different heating times.	160

List of Tables

4.1	Properties of rutile TiO ₂ from present calculations, compared to experimental data. Units: lattice parameters in Å, Raman frequencies in cm ⁻¹ , thermal expansion coefficients in 10 ⁻⁶ K ⁻¹ , volume compressibility in 10 ⁻³ GPa ⁻¹	66
4.2	Frequencies of the three Raman modes, their logarithmic pressure and temperature derivatives, and mode Grüneisen parameters. The measured isobaric temperature derivatives are separated into the pure volume and pure temperature contributions. Samara and Peercy's results are listed in the lower row for each mode. And mode Grüneisen parameters are from Ref. [59]	70
4.3	Fitting parameters for the temperature dependent Raman modes (unit: 10 ¹¹ erg ⁻¹)	80
4.4	Entropy in J/(mol K) of rutile TiO ₂ from MD calculations and experimental data of Ref. [95].	90
5.1	Comparison of the mode frequencies (cm ⁻¹) at the Γ point for rutile SnO ₂ . Calc1. is from the first principles LDA calculation from Borges, <i>et al.</i> , Ref. [105]; Calc2. is from Force field calculation by Katiyar, <i>et al.</i> , Ref. [97]. For expt., the data of infrared active modes at 100 K are from Katiyar, <i>et al.</i> , Ref. [97], and The data for Raman-active modes at 83 K are from the present measurement.	101

5.2	Frequencies of the three Raman modes, mode Grüneisen parameters, and the logarithmic pressure and temperature derivatives of frequency. Grüneisen parameters data from Hellwig, <i>et al.</i> , Ref. [98]. Thermal expansion data from Peercy and Morosin, Ref. [65]	105
5.3	Fitting parameters for the temperature dependent Raman modes (unit: 10^{10} erg^{-1})	109
6.1	Properties of Ag_2O with the cuprite structure from present MD calculations, compared to experimental data. Units: lattice parameters in Å, bulk modulus in GPa, thermal expansion coefficients in 10^{-6}K^{-1} , vibrational frequencies in meV. Lattice parameter at 40 K is from neutron scattering measurements in the present work, which is in good agreement with Refs. [[111, 112]]. Bond linear thermal expansion (LTE) and variance data are from Refs. [[121, 122]]. The IR active mode frequencies are from FT-IR measurements in the present work, and the frequencies of the lowest two modes are from the luminescence spectra in Ref. [141].	128
B.1	Derivation of the correlation table between point group O_h and D_{3d}	155
B.2	Derivation of the correlation table between point group O_h and T_d	155
B.3	Irreducible representation of Ag atoms	156
B.4	Irreducible representation of O atoms	156

Chapter 1

Lattice Dynamics and Phonon-Phonon Interactions

1.1 Bravais Lattices

A fundamental concept in the description of a crystalline solid is the Bravais lattice, which specifies the long-range periodicity. A crystal lattice can be generated by the infinite repetition in 3-dimensional space of a unit cell defined by three noncoplanar vectors: \vec{a}_1 , \vec{a}_2 , and \vec{a}_3 , which are called the primitive lattice vectors of the crystal. Labeling each unit cell by a triplet of integers $l = (l_1, l_2, l_3)$, the equilibrium position of the origin of the unit cell l is

$$\vec{R}_l = l_1 \vec{a}_1 + l_2 \vec{a}_2 + l_3 \vec{a}_3 \quad (1.1)$$

There are 14 Bravais lattices in 3 dimensions. A crystal can be described by its underlying Bravais lattice, together with the arrangement of atoms within a particular unit cell. The equilibrium position of each atom in the unit cell can be assigned a basis vector \vec{b} with respect to the origin of the unit cell \vec{R}_l . The term "lattice with a basis" is usually used to describe the combination of these two vectors.

Sometimes it is convenient to study a Bravais lattice by its reciprocal lattice, which is the Fourier transform of the real space domain of the original lattice to its momentum k -space.

$$\exp(i\vec{K} \cdot \vec{R}_l) = 1 \quad (1.2)$$

In this case, the reciprocal lattice vectors \vec{K} are essentially the set of all wave vectors that yield plane waves with the periodicity of a given Bravais lattice, i.e., the reciprocal lattice consists of the equiphase planes of the plane wave for a given Bravais lattice, and they are one-to-one maps to each other. Like the Wigner-Seitz cell in real space, the volume included by surfaces at the same distance from one site of the reciprocal lattice and its neighbors is defined to be the first Brillouin zone.

1.2 Harmonic Lattice Dynamics

In the model of harmonic lattice dynamics, the interatomic potentials are assumed to be quadratic function of atom displacements. We shall see that the properties of a lattice are not given accurately by a harmonic model in which phonons are assumed to be a set of independent oscillators, however, this approximation gives rise to a good quantum number, n , the number of excitation of a vibrational normal mode, or equivalently, n phonons, based upon which most of anharmonic theories are being developed.

In a periodic lattice, the basis functions for atom displacements should satisfy the Bloch condition, therefore the displacement of atom in the l th unit cell and basis b can be expressed as a Fourier transformation as

$$\vec{u}\left(\begin{matrix} l \\ \vec{b} \end{matrix}\right) = \sum_{\vec{q}} \vec{U}\left(\begin{matrix} \vec{q} \\ \vec{b} \end{matrix}\right) e^{i\vec{q}\cdot\vec{l}} \quad (1.3)$$

This reduces the periodic system with infinite unit cells to just one cell with displacement $\vec{U}\left(\begin{matrix} \vec{q} \\ \vec{b} \end{matrix}\right)$. Therefore we need to solve a standard small vibration problem within one cell, but keeping in mind the \vec{q} dependence in this cell.

$$\frac{d^2}{dt^2} \vec{U}\left(\begin{matrix} \vec{q} \\ \vec{b} \end{matrix}\right) = - \sum_{b'} \frac{\hat{D}\left(\begin{matrix} \vec{q} \\ \vec{b} \vec{b}' \end{matrix}\right)}{\sqrt{M_b M_{b'}}} \vec{U}\left(\begin{matrix} \vec{q} \\ \vec{b}' \end{matrix}\right) = - \sum_{b'} K\left(\begin{matrix} \vec{q} \\ \vec{b} \vec{b}' \end{matrix}\right) \vec{U}\left(\begin{matrix} \vec{q} \\ \vec{b}' \end{matrix}\right) \quad (1.4)$$

where the dynamical matrix \hat{D} is the Fourier transform of the harmonic force constants

$$\hat{D}\left(\begin{matrix} \vec{q} \\ \vec{b} \vec{b}' \end{matrix}\right) = \sum_{\vec{h}} \Phi\left(\begin{matrix} \vec{h} \\ \vec{b} \vec{b}' \end{matrix}\right) e^{i\vec{q}\cdot\vec{h}} \quad (1.5)$$

and the renormalized displacement, $\vec{U} = \sqrt{NM_b} \vec{U}$. Since the dynamical matrix is Hermitian, we can always find a unitary transformation matrix $[C]$, such that $[C]^\dagger [K] [C]$ is diagonal. This is equivalent to an eigenvalue problem $[K] \vec{e}_s = \lambda \vec{e}_s$, where $\vec{e}_s\left(\begin{matrix} \vec{q} \\ \vec{b} \end{matrix}\right)$ is the column vector of $[C]$. At same time, \vec{U} is automatically decomposed to a set of uncoupled eigenstates X_s as

$$\vec{u} \begin{pmatrix} \vec{q} \\ \vec{b} \end{pmatrix} = \sum_s \vec{e}_s \begin{pmatrix} \vec{q} \\ \vec{b} \end{pmatrix} X_s \quad (1.6)$$

For our problem, we can seek the simple solution of $X_s = e^{i\omega_s t}$, then Eq. (1.4) becomes

$$\omega_s^2 \vec{e}_s = [K] \vec{e}_s \quad (1.7)$$

The solution gives the normal modes and the vector \vec{e}_s . In lattice dynamics, $\vec{e}_s \begin{pmatrix} \vec{q} \\ \vec{b} \end{pmatrix}$ is usually called the polarization vector due to its physical meaning, i.e., projecting the normal mode to the atomic displacements. As we can see from Eq. (1.7), the mass renormalization is necessary because otherwise a mass matrix will be re-diagonalized and this will lead to the inconvenient couplings of masses M_b .

With the normal modes known, we can simply obtain the well-known second quantization expression for X_s in terms of the creation and annihilation operators of phonons, a^\dagger and a ,

$$X_s(\vec{q}) = \sqrt{\frac{\hbar}{2\omega_s(\vec{q})}} (a_{-\vec{q}s}^\dagger + a_{\vec{q}s}) = \sqrt{\frac{\hbar}{2\omega_s(\vec{q})}} \hat{A}_{\vec{q}s} \quad (1.8)$$

Introducing the second quantization is a powerful way to deal with interactions of excitations, such as phonons and electrons, because the interaction can be depicted physically as the creation and annihilation of propagators, which will be discussed in the following sections.

Combining Eq. (1.3), (1.6) and (1.8), it can be shown that the second quantization expression for the atomic displacement is

$$\vec{u} \begin{pmatrix} \vec{l} \\ \vec{b} \end{pmatrix} = \sum_{\vec{q},s} \frac{\vec{e}_s \begin{pmatrix} \vec{q} \\ \vec{b} \end{pmatrix}}{\sqrt{\omega_s(\vec{q})}} e^{i\vec{q}\cdot\vec{l}} \hat{A}_{\vec{q}s} \quad (1.9)$$

1.3 Quasiharmonic Approximation

The quasiharmonic approximation (QHA) assumes that phonon frequencies depend on volume alone, and the lattice dynamics at elevated temperatures can be approximated as harmonic normal modes with frequencies that are altered by thermal expansion. The usual trend is for phonons to soften with lattice expansion, increasing the phonon entropy and stabilizing the expanded lattice at elevated temperatures.

A mode Grüneisen parameter γ_j is defined as the ratio of the fractional change of the mode frequency ω_j to the fractional change of volume V at constant temperature.

$$\gamma_j = -\frac{\partial(\ln \omega_j)}{\partial(\ln V)} \quad (1.10)$$

In the QHA method, the thermal expansion is evaluated by optimizing the vibrational free energy as a function of volume.

$$F(T, V) = E_s + \int g(\omega) \left(\frac{\hbar\omega}{2} + k_B T \ln(1 - e^{-\hbar\omega/(k_B T)}) \right) \quad (1.11)$$

where the static energy E_s is the energy of the cell when all atoms are at their equilibrium positions. The vibrational free energy in the QHA is minimized to obtain both ω_j and V at different temperatures, and together with the bulk modulus B and mode specific heat, C_{Vj} it is straightforward to calculate the thermal expansion coefficient within the QHA as

$$\alpha = \frac{1}{B} \sum_j \gamma_j C_{Vj} . \quad (1.12)$$

As we can see, all non-harmonic behavior is included in the Grüneisen parameters, which depend only on volume.

1.4 Anharmonic Lattice Dynamics

The anharmonic parts of atomic potentials are those involving terms higher than second-order terms in the atomic displacements. When the anharmonicity is not large, for example at very low temperature, we can still linearize the system with the original harmonic phonons as we do in the quasiharmonic approximation. However, especially at high temperatures, with more and more anharmonic part of the atomic potential being explored, the harmonic theory breaks down because a set of anharmonic oscillators cannot be uncoupled. Transition probabilities, or interactions, exist among them and depend on the strength of the anharmonic couplings.

With the second quantization expression for the atomic displacement as derived in Eq. 1.9, we can conveniently obtain the Hamiltonian of any order in the second quantization form. For example, the cubic anharmonic Hamiltonian can be expanded as

$$H^{(3)} = \sum_{\vec{q}s, \vec{q}'s', \vec{q}''s''} \left[\left(\frac{\hbar}{2N} \right)^{\frac{3}{2}} \frac{1}{6 \sqrt{\omega_s(\vec{q})\omega_{s'}(\vec{q}')\omega_{s''}(\vec{q}'')}} N \delta_{\vec{q}+\vec{q}'+\vec{q}'', \vec{G}} \sum_{\vec{b}\alpha} \sum_{\vec{h}'\vec{b}'\beta} \sum_{\vec{h}''\vec{b}''\gamma} \Phi_{\alpha\beta\gamma}(\vec{h}', \vec{h}'', \vec{b}, \vec{b}', \vec{b}'') \right. \\ \left. \frac{e_s^\alpha(\vec{q}) e_{s'}^\beta(\vec{q}') e_{s''}^\gamma(\vec{q}'')}{\sqrt{M_b M_{b'} M_{b''}}} e^{i\vec{q}' \cdot \vec{h}'} e^{i\vec{q}'' \cdot \vec{h}''} \right] \hat{A}_{\vec{q}s} \hat{A}_{\vec{q}'s'} \hat{A}_{\vec{q}''s''} \quad (1.13)$$

$$= V^{(3)}(\vec{q}, s; \vec{q}', s'; \vec{q}'', s'') \hat{A}_{\vec{q}s} \hat{A}_{\vec{q}'s'} \hat{A}_{\vec{q}''s''} \quad (1.14)$$

where, $\Phi_{\alpha\beta\gamma}(\vec{h}', \vec{h}'', \vec{b}, \vec{b}', \vec{b}'')$ is the third order force constant, and all other symbols and indices stand for the same physical quantities as those in the preceding sections about harmonic lattice dynamics.

This second quantization form of Hamiltonian of higher orders shows vividly how phonons interact with each other by the creation and annihilation operators \hat{A} . More importantly, this form is convenient for us to construct Green's functions for higher order terms in the many-body interactions. The Green's function method for phonon-phonon interactions is discussed in the next section.

1.5 Green's Function Method

Condensed matter physics has evolved from traditional solid state physics that largely focuses on the effective single particle picture in solids to the description of many-body interactions and collective phenomena in matter. The understanding of frequencies and lifetimes of interacting quasi-particles at ground or excited states is one of the most important and interesting topics, and the anharmonic phonon lifetime and frequency shift are such examples.

The essential feature is that interactions can only be treated correctly by taking into account the infinite order of "weak" perturbations. A systematic mathematical formulation of the many-body interaction is called the Green's function method, which is the fundamental theory of the modern condensed matter physics and is the primary concept of non-relativistic quantum field theory. Some important concepts and conclusions will be discussed in this section, and in the next section we will discuss phonon-phonon interactions using this method. More detailed presentations of the Green's function method can be found in [1–3].

1.5.1 The Retarded Green's Function and Lehmann Representation

We can define a correlation between two Heisenberg operators $A(t)$ and $B(t)$,

$$G_R(t, t') = -\frac{i}{\hbar} \theta(t - t') \langle [A(t), B(t')]_{\pm} \rangle \quad (1.15)$$

where $A(t) = e^{iHt/\hbar} A e^{-iHt/\hbar}$ is an operator in the Heisenberg picture with the full Hamiltonian H . The symbol $\langle \rangle$ represents the ensemble average and $[\]_{\pm}$ chooses commutators for Fermions or anticommutators for Bosons. It is called the retarded Green's function because it works only in the time regime $t > t'$. To understand the Green's function, we may first notice that

$$G_R(t, t') = G_R(t - t') = -\frac{i}{\hbar} \theta(t - t') \langle [A(t - t'), B]_{\pm} \rangle \quad (1.16)$$

The Green's function therefore has the fundamental property of a propagator which characterizes a propagating process of a state containing one additional particle. For example, we usually specify $A(t) = \hat{\Psi}(t)$ and $B(t') = \hat{\Psi}^\dagger(t')$ where $\hat{\Psi}$ and $\hat{\Psi}^\dagger$ are the field operators for destruction and creation. Then the above definition depicts a propagator which adds a quasiparticle at time t' and removes it at time t .

The retarded Green's function contains all necessary information for a interacting system. By Fourier transforming G_R , we can obtain

$$G_R(\omega) = \frac{1}{Z} \sum_{n,m} e^{-\beta E_n} \langle n|B|m\rangle \langle m|A|n\rangle \frac{e^{\beta \hbar \omega_{nm}} \pm 1}{\omega - \omega_{nm} + i\eta} \quad (1.17)$$

where $\omega_{nm} = \hbar^{-1}(E_n - E_m)$ is the energy difference of two excited states n and m in the interacting system, and η is a positive infinitesimal. Here an integral representation for the step function is used:

$$\theta(t - t') = - \int_{-\infty}^{\infty} \frac{d\omega}{2\pi i} \frac{e^{-i\omega(t-t')}}{\omega + i\eta} \quad (1.18)$$

Eq. 1.17 is the well-known Lehmann representation. $G_R(\omega)$ is analytic in the upper half plane and the poles in the lower half plane determine the energy spectrum of excitations of the interacting system. $G_R(\omega)$ may contain even deeper physical meaning, in that according to the linear response theory,

$$\Delta A = G_R(\omega) e^{-i\omega t + \eta t} \quad (1.19)$$

This implies that the retarded Green's function is the amplitude of the system's response to the external disturbance ω . The amplitude will reach infinity when the external disturbance is in resonance with the intrinsic frequency ω_{nm} , and hence gives mathematical poles. On the other hand, the retarded Green's function is naturally related to the thermodynamic observables, due to the fact that in second quantization thermodynamic observables can be expressed as the product of field operators, and the Green's function itself is also defined in this way.

In the similar manner, we can define the so called advanced Green's function

$G_A(\omega)$ by flipping the poles of $G_R(\omega)$ with respect to the real axis to the upper half plane. Combining these two Green's function G_R and G_A we can obtain the real-time Green's function $G(\omega)$ which is analytic all over the complex plane except the real axis. The Green's function in real space is hence defined as

$$G(t, t') = -\frac{i}{\hbar} \langle T [A(t), B(t')] \rangle \quad (1.20)$$

where the time ordering operator T orders the operators with the latest time t on the left and includes an additional factor -1 for each interchange of Fermion operators.

The functions have a common generating function

$$\Gamma(z) = \int_{-\infty}^{\infty} \frac{d\omega'}{2\pi} \frac{\rho(\omega')}{z - \omega'} \quad (1.21)$$

This is easily proved to be true by defining $\rho(\omega)$ as the imaginary part of $G_R(\omega)$, and this quantity can be identified as the density of states. It is then straightforward to see that $z = \omega$ for G and $z = \omega \pm i\eta$ for G_R and G_A respectively.

1.5.2 Perturbation Theory and Wick's Theorem For Finite Temperatures

All the above discussions are based on one assumption that we have known the eigenstates and energies of the interacting systems $H = H_0 + H_1$, which, however, is what we are trying to resolve in the first place. Therefore, although the Lehmann representation of Green's functions shows its power to derive the relationships of physical observables and obtain the energy spectrum of excited states, we have to figure out a way to calculate the Green's function as defined in the Heisenberg picture in terms of some functions that are already known. Usually, this is done by perturbation theory.

For finite temperatures (for the zero temperature condition, a similar but much simpler calculation can be performed in accordance with the Gell-Mann and Low theorem), we need to first generalize the real time t in the Heisenberg picture

and interaction picture to be a complex or pure imaginary time τ , i.e, $\hat{\Psi}(\tau) = e^{H\tau/\hbar} \hat{\Psi} e^{-H\tau/\hbar}$ and $\hat{\Psi}_I(\tau) = e^{H_0\tau/\hbar} \hat{\Psi} e^{-H_0\tau/\hbar}$. In this manner, we define the temperature Green's function

$$g(\tau, \tau') = -\langle T_\tau[\hat{\Psi}(\tau) \hat{\Psi}^\dagger(\tau')] \rangle \quad (1.22)$$

where T_τ is the time ordering operator with respect to τ . The Green's function consists of a matrix element of Heisenberg operators. This form is inconvenient for perturbation theory. It can be shown (with the Gell-Mann and Low theorem) that this Green's function can be related to the corresponding (generalized) interaction picture for the field operators and perturbation Hamiltonian H_1 in the following way

$$g(\tau, \tau') = -\frac{\langle \sum_{n=0}^{\infty} \frac{1}{(-\hbar)^n} \frac{1}{n!} \int_0^{\beta\hbar} \cdots \int_0^{\beta\hbar} d\tau_n T_\tau[H_1(\tau_1) \cdots H_1(\tau_n) \hat{\Psi}_I(\tau) \hat{\Psi}_I^\dagger(\tau')] \rangle_0}{\langle \sum_{n=0}^{\infty} (-\hbar)^{-n} (n!)^{-1} \int_0^{\beta\hbar} \cdots \int_0^{\beta\hbar} d\tau_n T_\tau[H_1(\tau_1) \cdots H_1(\tau_n)] \rangle_0} \quad (1.23)$$

where $\langle \rangle_0$ represents the non-interacting H_0 ensemble average. That the integral extends from 0 to $\beta\hbar$ is reasonable because of the $\beta\hbar$ periodicity of $g(\tau, \tau')$, and this magic periodicity also guarantees the transformation of temperature Green's function from the τ domain to the frequency domain, which is quite crucial because it connects with the real-time Green's function as we will see soon.

Eq. (1.23) shows that we must evaluate the expectation value of time ordering T_τ products of creation and destruction operators, like $\langle ABC \cdots F \rangle_0$. The straightforward approach of classifying all possible contributions is very lengthy. Instead, we shall rely on Wick's theorem, which provides a general procedure for this calculation. The main idea is to define a contraction

$$A \bullet B \bullet = T[AB] - N[AB] \quad (1.24)$$

where A, B are field operators in the (generalized) interaction picture. The normal ordering N represents a different order in which all the annihilation operators are

placed to the right of all the creation operators. Thus a T product may be evaluated by reducing it to the corresponding N product. N product is convenient because its expectation in the non-interacting ensemble average is mostly zero. For example, according to the definition of g in Eq. (1.22) and the corresponding interaction picture, $\hat{\Psi}(\tau)_I \hat{\Psi}_I^\dagger(\tau')$ equals $-g^0(\tau, \tau')$, the non-interacting temperature Green's function or free propagator, which is easy to evaluate. Then Wick's theorem asserts that $\langle ABC \cdots F \rangle_0$ is equal to the sum over all possible fully contracted terms, i.e., the exact temperature Green's function g can be expanded in a series containing the simple products of g^0 and perturbation potential. The complete proof can be found in Ref. [1]. Due to the $\beta\hbar$ periodicity of $g(\tau, \tau')$ for each of its argument, for temperature Green's function, this expansion can be analyzed in energy space at a discrete set of points ω_n , and $\omega_n = 2n\pi/\beta\hbar$ for bosons, or $(2n + 1)\pi/\beta\hbar$ for fermions, and the corresponding Fourier transformation is

$$g(\omega_n) = \int_0^{\beta\hbar} d\tau e^{i\omega_n\tau} g(\tau) \quad (1.25)$$

We can associate a picture, called a Feynman diagram, with each of the terms in the series expansion. Conventionally, the Green's function G or g is denoted by a bold or double solid line with an arrow. The free propagator g^0 is denoted by a solid line with an arrow while the interaction potential is denoted by a wavy line (or equivalently, by a vertex). These diagrams appearing in the perturbation analysis form a convenient way of classifying the terms obtained with Wick's theorem. One may begin with a few simple diagrams, then all possible summations of lines and vertices are constructed based on the geometry (called "putting flesh on the skeletons"). Finally, a particular compact form of this expansion yields Dyson's equation

$$g(\omega_n) = g^0(\omega_n) + g^0(\omega_n)\Sigma^*(\omega_n)g(\omega_n) \quad (1.26)$$

where Σ^* is the proper self-energy, in which all the interaction are involved. The Feynman diagram of Dyson's equation is shown in Fig. 1.1

In the next section, we will focus on the calculation of the proper self-energy of

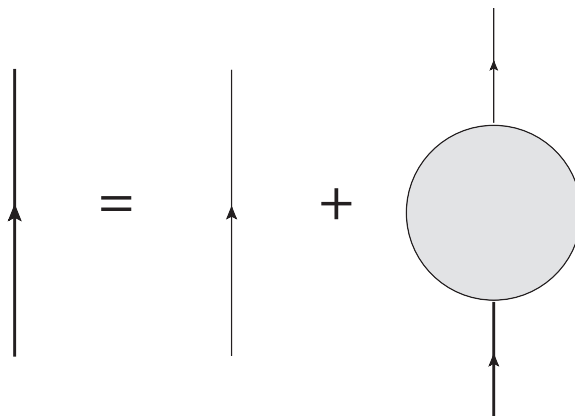


Figure 1.1: Dyson's equation

phonons, thereby obtaining the quantitative result of phonon-phonon interactions; similar evaluations can be done for the correlation energy of electron interactions (e.g., random phase approximation) and electron-phonon interactions (e.g., BCS theorem).

Finally, we should note that although the temperature Green's function is convenient for performing mathematical calculations, it cannot be directly related to the frequencies and lifetimes of excited states at finite temperature. Those quantities are contained in the real-time retarded Green's function G_R as we discussed in the previous section. Fortunately, similar to G , we can show that the temperature Green's function $g(\omega_n)$ can be expressed by the generating function $\Gamma(z)$ of Eq. (1.21) as well, and $z = i\omega_n$ in this case. Therefore the analytical continuation, in which z changes from $i\omega_n$ to $\omega \pm i\eta$ simply offers a remarkable connection between g and G . In any practical calculation, we first evaluate $g(\omega_n)$ via the expansion process discussed above, and therefore know $\Gamma(z)$ at discrete set of points. Then it is necessary to perform an analytic continuation to the whole complex plane with the restriction $\Gamma(z) \sim z^{-1}$ as $|z| \rightarrow \infty$.

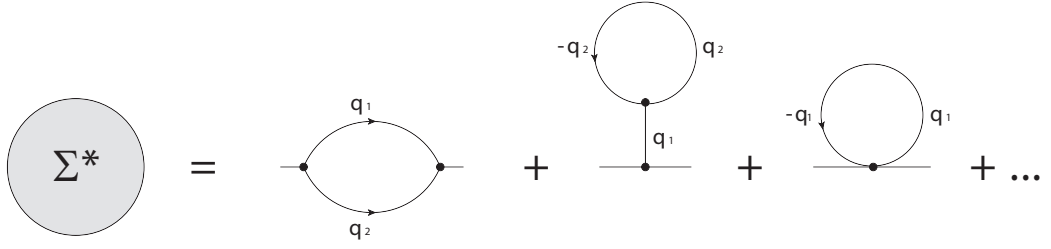


Figure 1.2: The lowest order terms of the proper self energy

1.6 Phonon-Phonon Interactions and Phonon Lifetime

We define the phonon temperature Green's function g , in which, $q = (\vec{q}, s)$ is the short notation for the branch s and \vec{q} vector for an anharmonic phonon

$$g_{qq'}(\tau, \tau') = - \langle T_\tau [\hat{A}_q(\tau) \hat{A}_{q'}^\dagger(\tau')] \rangle \quad (1.27)$$

It is exactly the same definition as in the general case, with the interaction Hamiltonian (or vertex in Feynman diagram) in this case a form shown in Eq. 1.13. We can then follow the well established procedure discussed previously to derive the phonon interactions quantitatively.

Step 1: The free propagator

This provides the concrete expression of solid lines in the diagram

$$g_{qq'}^0(\tau - \tau') = - \langle T_\tau [\hat{A}_{qI}(\tau) \hat{A}_{q'I}^\dagger(\tau')] \rangle_0 \quad (1.28)$$

$$= \langle T[a_{-q}^\dagger(\tau) a_{-q}(\tau') + a_q(\tau) a_q^\dagger(\tau')] \rangle_0 \quad (1.29)$$

Here only $q = q'$ will have nonzero values. We can then transform it to the corresponding frequency domain, and the result is

$$g^0(q, \omega_n) = \frac{1}{i\omega_n - \omega_q} - \frac{1}{i\omega_n + \omega_q} = \frac{2\omega_q}{\omega_n^2 + \omega_q^2} \quad (1.30)$$

Step 2: Dyson's equation

$$g_{\vec{q}ss'}(\omega_n) = g^0(\vec{q}s, \omega_n) + g^0(\vec{q}s, \omega_n) \sum_{s''} \Sigma_{\vec{q}ss''}^*(\omega_n) g_{\vec{q}s''s'}(\omega_n) \quad (1.31)$$

We can write the free phonon propagators in Eq. (1.31) in explicit form using Eq. (1.30) and neglect the non-diagonal terms. We get

$$g_{\vec{q}ss}(\omega_n) = \frac{2\omega_s(\vec{q})}{\omega_s^2(\vec{q}) + \omega_n^2 - 2\omega_s^2(\vec{q})\Sigma_{\vec{q}ss}^*(\omega_n)} \quad (1.32)$$

We see the anharmonic Green's function is of the same form as Eq. (1.30) for the free propagator in the harmonic approximation. All the effects of anharmonic interactions are included in Σ^* . If we write the self energy as a real and imaginary part, then the frequency shift and lifetime of the phonons are explicitly identified.

$$\Sigma_{\vec{q}ss}^*(\omega_n) = -\Delta_{\vec{q}ss}(\omega_n) + i\Gamma_{\vec{q}ss}(\omega_n) \quad (1.33)$$

Step 3: The diagrams of the lowest order terms of the proper self energy are presented in Fig. 1.2. The mathematical derivation of the 2nd order diagram (the first diagram on the left) is shown in Appendix A, which is a concrete practice of the temperature Green's function approach discussed in this chapter.

The resulting mathematical expressions for these lowest orders diagrams are

$$\Delta_s^{(3)}(\Omega) = -\frac{18}{\hbar^2} \sum_{\vec{q}_1 s_1} \sum_{\vec{q}_2 s_2} |V(s; \vec{q}_1 s_1; \vec{q}_2 s_2)|^2 \times \wp \left[\frac{n_1 + n_2 + 1}{\Omega + \omega_1 + \omega_2} - \frac{n_1 + n_2 + 1}{\Omega - \omega_1 - \omega_2} + \frac{n_1 - n_2}{\Omega - \omega_1 + \omega_2} - \frac{n_1 - n_2}{\Omega + \omega_1 - \omega_2} \right] \quad (1.34a)$$

$$\Delta_s^{(3')} = -\frac{72}{\hbar^2} \sum_{s_1} \sum_{\vec{q}_2, s_2} V(s; s; \vec{0} s_1) V(\vec{0} s_1; -\vec{q}_2 s_2; \vec{q}_2 s_2) \times \wp \left(\frac{1}{\omega_1} \right) \left(n_2 + \frac{1}{2} \right) \quad (1.34b)$$

$$\Delta_s^{(4)} = \frac{24}{\hbar} \sum_{\vec{q}_1, s_1} V(s; s; \vec{q}_1 s_1; -\vec{q}_1 s_1) \left(n_1 + \frac{1}{2} \right) \quad (1.34c)$$

$$\Gamma_s^{(3)}(\Omega) = \frac{18\pi}{\hbar^2} \sum_{\vec{q}_1 s_1} \sum_{\vec{q}_2 s_2} |V(s; \vec{q}_1 s_1; \vec{q}_2 s_2)|^2 \times \left[(n_1 + n_2 + 1) \delta(\Omega - \omega_1 - \omega_2) + 2(n_1 - n_2) \delta(\Omega + \omega_1 - \omega_2) \right] \quad (1.34d)$$

1.7 Self-Consistent Lattice Dynamics

Consider a crystal with Hamiltonian

$$H = T_k + V \quad (1.35)$$

where T_k is the kinetic energy and the potential energy is given by

$$V = \frac{1}{2} \sum_{ll'} \psi(\vec{r}_{ll'} + \vec{w}_{ll'}) \quad (1.36)$$

Here, $\vec{r}_{ll'}$ are mean position vectors joining the atoms l and l' , and $\vec{w}_{ll'}$ are the relative displacement vectors.

Instead of trying to find the perturbation expansion as we usually do in the quasiharmonic and anharmonic lattice dynamics, we now consider an effective harmonic Hamiltonian

$$\hat{H} = T_k + \hat{V} \quad (1.37)$$

where

$$\hat{V} = \frac{1}{4} \sum_{ll'} \sum_{\alpha\beta} \hat{\phi}_{\alpha\beta}(ll') w_{ll'\alpha} w_{ll'\beta} \quad (1.38)$$

and the effective force constant $\hat{\phi}$ and the mean distance $r_{ll'}$ may be determined self-consistently.

In essence, this method tries to obtain a mean field of harmonic form and keeps the field updated. In this process, we want to have the potential difference operator $\hat{E} = V - \hat{V}$ having the eigenvalue ϵ sufficiently small. Under this assumption, the density matrix operator can be written as

$$\rho(H) = e^{-\beta H} = e^{-\beta \epsilon} \rho(\hat{H}) e^{-\beta(\hat{E} - \epsilon)} \quad (1.39)$$

We may disregard the last factor if $\langle e^{-\beta(\hat{E} - \epsilon)} \rangle_{\hat{H}} = 1$. Here, $\langle \rangle_{\hat{H}}$ is the thermal

average under the effective Hamiltonian. To the first order, this requires

$$\epsilon = \langle \hat{V} \rangle_{\hat{H}} \quad (1.40)$$

We can therefore write the free energy approximately as

$$F = \hat{F} + \langle \hat{V} \rangle_{\hat{H}} \quad (1.41)$$

where

$$\hat{F} = -k_B T \ln \text{Tr}\{\rho(\hat{H})\} \quad (1.42)$$

and

$$\langle \hat{V} \rangle_{\hat{H}} = \frac{1}{2} \sum_{ll'} \langle \psi(\vec{r}_{ll'} + \vec{w}_{ll'}) \rangle_{\hat{H}} - \frac{1}{4} \sum_{ll'} \sum_{\alpha\beta} \hat{\phi}_{\alpha\beta}(ll') \langle w_{ll'\alpha} w_{ll'\beta} \rangle_{\hat{H}} \quad (1.43)$$

Note that $\langle w_{ll'\alpha} w_{ll'\beta} \rangle_{\hat{H}}$ is the displacement correlation function. Hence, the free energy can be approximated by the free energy belonging to the effective harmonic Hamiltonian, and the difference is supposed to be small. Physically speaking, it means that for a system, even very anharmonic, we may find a harmonic system that is effectively close enough to the dynamic and thermodynamic properties of the original one. If this is the case, the problem is greatly simplified because the harmonic theory is relatively complete.

With modern DFT calculations, several computational algorithms based on the self-consistent lattice dynamics are being developed. Essentially, these methods assign large displacements of atoms corresponding to the target temperature by a random assignment or molecular dynamics simulation, and then try to find the effective harmonic force constants by optimizing the thermodynamic quantities of the system [4, 5].

Chapter 2

Experimental Methods

2.1 Raman Scattering

2.1.1 Introduction

When crystal or molecule is illuminated with monochromatic light of frequency ω_L (usually from a laser in the visible, near infrared, or near ultraviolet range), it is found that the scattered spectrum of radiation consists of a very strong line at the frequency of the incident light, as well as of a series of much weaker lines with frequencies $\omega_L \pm \omega_q$, where ω_q are found to be equal to some optical phonon energies. The strong line centered at ω_L is known as Rayleigh scattering, which originates from elastic scattering of photons. The series of weak lines constitute the Raman spectrum, which originates from the inelastic scattering of photons by phonons. The Raman lines at frequencies $\omega_L - \omega_q$ are called Stokes lines, and those at frequencies $\omega_L + \omega_q$ are called anti-Stokes lines. The intensities of Stokes lines are generally much stronger than anti-Stokes lines, and as a result, Raman spectrum is usually taken on the side of Stokes lines.

Since its discovery, many variations of Raman spectroscopy have been developed. Examples include surface enhanced Raman, resonance Raman, Raman microscopy and time-resolved stimulated Raman spectroscopy. Owing to its great versatility, Raman spectroscopy has been widely used in physics, chemistry, geology, biology and many other fields of science and engineering. In chemistry and geology, for example, Raman spectra are usually used to collect a fingerprint by which the molecule or crystal can be identified, owing to the fact that vibrational information is specific to the chemical bonds and symmetry. It also provides a convenient way to perform in situ or non-destructive measurements, which is extremely important in many fields. For physicists and materials scientists, it is an excellent tool for studying excitations such as phonons, magnons and excitons in solids.

In our work, Raman spectroscopy is mainly used to investigate anharmonic phonon behavior under temperature, and we will focus on first order Raman

scattering. In first order Raman scattering, only optical phonons with momentum equal to zero are involved, as a consequence of the large momentum difference between phonons and photons. Although this is a limitation, Raman spectroscopy probes phonon modes with extremely high resolution in energy, which is of great value to study the phonon anharmonicity characterized by the energy broadening and shift, for example.

In this section, we will focus on the theories of Raman scattering. The experimental details will be discussed, along with the specific descriptions of data collection, in Chapters 4 to 6, and Appendix C, in which particular samples are in study. Here, we start with a brief discussion of the classical theory of Raman scattering. We then introduce the quantum theory to describe quantitatively how photons interact with phonons in those inelastic scattering processes. We then spend considerable efforts deriving and discussing Raman selection rule. The selection rule is established with quantum theory and group theory; it provides the fundamental information of symmetries of modes, and is therefore critical for our study in understanding phonon dynamics.

2.1.2 The Frequency Resolved Raman Spectroscopy

2.1.2.1 Classical Theory

Let $\vec{E} = \vec{E}_0 \cos \omega_L t$ be the electric field vector of the incident light and Q be the normal coordinate of small displacements of the nuclei, the dipole moment \vec{M} is contributed by two parts,

$$\vec{M} = \vec{M}_d(Q) + \alpha(Q)\vec{E} \quad (2.1)$$

where $\vec{M}_d(Q)$ is the static dipole moment of the system plus the response to the atomic displacements. When the incident light is in the infrared, the atomic displacement is the dominant mechanism for scattering light, and the moment $\vec{M}_d(Q)$ drives the infrared scattering. On the other hand, the Raman effect originates with the electric field induced dipole moment $\vec{M}_e = \alpha(Q)\vec{E}$. Here $\alpha(Q)$ is the polarizabil-

ity, in general, \vec{M}_e does not coincide with the direction of \vec{E} , and the polarizability is thus a second-order tensor. It can be shown further that it is symmetrical, i.e., $\alpha^T = \alpha$, hence only six of the nine components of α are independent.

Expanding the static dipole moment, $\vec{M}_d(Q)$, and the polarizability, $\alpha(Q)$, in terms of Q , we obtain

$$\vec{M} = \vec{M}_{d0} + \left(\frac{\partial \vec{M}_d}{\partial Q} \right)_0 Q + \alpha_0 \vec{E} + \left(\frac{\partial \alpha}{\partial Q} \right)_0 Q \vec{E} + O(Q^2) \quad (2.2)$$

In the following discussion of the fundamental principles, we will mainly focus on the Raman effect since the mathematical treatment of infrared scattering is similar. We drop the subscript e of \vec{M}_e for brevity.

If a molecule vibrates with the frequency ω_q , we have $Q = Q_0 \cos \omega_q t$ and the electric field induced dipole moment can be written

$$\vec{M}(t) = \alpha_0 \vec{E}_0 \cos \omega_L t + \frac{1}{2} \left(\frac{\partial \alpha}{\partial Q} \right)_0 Q_0 \vec{E}_0 [\cos(\omega_L - \omega_q)t + \cos(\omega_L + \omega_q)t] \quad (2.3)$$

According to the rule of electromagnetic radiation, the intensity of radiation emitted by the dipole moment $\vec{M}_e(t)$ into the solid angle $d\Omega = \sin \theta d\theta d\phi$ is given by

$$dI(t) = \frac{d\Omega}{4\pi c^3} \sin^2 \theta |\ddot{\vec{M}}(t)|^2 \quad (2.4)$$

Hence, the intensity of the scattered light per unit solid angle is give by

$$I(t) = E_0^2 \alpha_0^2 \omega_L^4 \cos^2 \omega_L t + \frac{1}{4} E_0^2 \left(\frac{\partial \alpha}{\partial Q} \right)_0^2 Q_0^2 [(\omega_L - \omega_q)^4 \cos^2(\omega_L - \omega_q)t + (\omega_L + \omega_q)^4 \cos^2(\omega_L + \omega_q)t] \quad (2.5)$$

It follows that the ratio of the intensities of the Stokes and anti-Stokes lines should be

$$\frac{I_S}{I_{AS}} = \frac{(\omega_L - \omega_q)^4}{(\omega_L + \omega_q)^4} \quad (2.6)$$

This is less than unity, which is found to be contrary to the experimental observa-

tion. This inconsistency is eliminated in the quantum theory of the Raman effect, as discussed next.

2.1.2.2 Quantum Theory and Placzek's Approximation

The fundamental problem of the classical treatment is that we ignore the quantum character of electrons and phonons, and we do not consider the occupancy factor in those quantum states. Consider a system (crystal or molecule) with Hamiltonian H obeying the time dependent Schrodinger equation

$$H_0 \psi^{(0)}(t) = i\hbar \frac{\partial}{\partial t} \psi^{(0)}(t) \quad (2.7)$$

and the general solution is a superposition of the eigenfunctions ϕ_r 's of the time independent Schrodinger equation (where $\phi_r = (e, n)$ denotes collectively the electronic quantum numbers e and the vibrational quantum numbers n .)

$$\psi^{(0)}(t) = \sum_r c_r \phi_r e^{-i\omega_r t} \quad (2.8)$$

Suppose that this system is perturbed by a light wave with the electric field vector $\vec{E} = \vec{E}^0 e^{-i\omega_L t}$. The Schrodinger equation of the perturbed system is

$$(H_0 - \vec{E} \cdot \vec{M}) \psi(t) = i\hbar \frac{\partial}{\partial t} \psi(t) \quad (2.9)$$

Qualitatively speaking, the wave functions of the perturbed system acquires a mixed character of all possible wave functions of the unperturbed system. We can regard it as a non-stationary state only for a physical description of this perturbation process, a so called "virtual state" in Raman scattering.

Rigorously, if the unperturbed system is in the state ϕ_k , using the time-dependent perturbation theory, it can be easily shown that the first order perturbed state is

$$\psi_k^{(1)} = \frac{1}{\hbar} \left(\sum_j \frac{\vec{E}^0 \cdot \vec{M}_{kj}}{\omega_{jk} - \omega_L} \phi_j \right) \exp[-i(\omega_k + \omega_L)t] + \frac{1}{\hbar} \left(\sum_j \frac{\vec{E}^{0*} \cdot \vec{M}_{kj}}{\omega_{jk} + \omega_L} \phi_j \right) \exp[-i(\omega_k - \omega_L)t] \quad (2.10)$$

where $\vec{M}_{kj} = \langle \phi_k | \vec{M} | \phi_j \rangle$ and $\omega_{jk} = \omega_k - \omega_j$. Meanwhile, the matrix element of the dipole moment of the perturbed system is

$$\begin{aligned} \vec{M}_{km}^{(p)}(t) &= \langle \psi_m^* | \vec{M} | \psi_k \rangle \\ &= \vec{M}_{km} \exp(-i\omega_{km}t) + \vec{C}_{km} \exp[-i(\omega_{km} + \omega_L)t] + \vec{D}_{km} \exp[-i(\omega_{km} - \omega_L)t] \end{aligned} \quad (2.11)$$

where

$$\vec{C}_{km} = \frac{1}{\hbar} \sum_j \frac{(\vec{E}^0 \cdot \vec{M}_{kj}) \vec{M}_{jm}}{\omega_{jk} - \omega_L} + \frac{\vec{M}_{kj} (\vec{E}^0 \cdot \vec{M}_{jm})}{\omega_{jm} + \omega_L} \quad (2.12)$$

$$\vec{D}_{km} = \frac{1}{\hbar} \sum_j \frac{(\vec{E}^{0*} \cdot \vec{M}_{kj}) \vec{M}_{jm}}{\omega_{jk} + \omega_L} + \frac{\vec{M}_{kj} (\vec{E}^{0*} \cdot \vec{M}_{jm})}{\omega_{jm} - \omega_L} \quad (2.13)$$

According to Eq. 2.4, we can obtain the intensity of the radiation by the dipole moment $\vec{M}_{km}^{(p)}(t)$.

$$I_{km} = \frac{4}{3c^3} [\omega_{km}^4 |\vec{M}_{km}|^2 + (\omega_{km} + \omega_L)^4 |\vec{C}_{km}|^2 + (\omega_{km} - \omega_L)^4 |\vec{D}_{km}|^2] \quad (2.14)$$

Using Eq. 2.12, the components of \vec{C}_{km} can be written in the form

$$(C_\mu)_{km} = \sum_\nu (c_{\mu\nu})_{km} E_\nu^0 \quad (2.15)$$

where the scattering tensor

$$(c_{\mu\nu})_{km} = \frac{1}{\hbar} \sum_j \frac{(M_\nu)_{kj} (M_\mu)_{jm}}{\omega_{jk} - \omega_L} + \frac{(M_\mu)_{kj} (M_\nu)_{jm}}{\omega_{jk} + \omega_L} \quad (2.16)$$

If the incident light is polarized in the direction of μ and the scattered light is observed with the analyzer in the direction of ν , one finds for the scattered radiation emitted per unit solid angle $d\Omega$

$$I_{km}[\mu\nu] = \frac{1}{c^4} (\omega_{km} + \omega_L)^4 |(c_{\mu\nu})_{km}|^4 I_0 \quad (2.17)$$

The direct evaluation of the scattering tensor $(c_{\mu\nu})_{km}$ is not practical in molecules and crystals due to the complexity of the energy levels and the incomplete knowledge of the excited states j 's. However, the scattering tensor of Eq. 2.16 derived by the quantum theory does provide a direct way determining the Raman-activity in terms of group symmetry.

Using Placzek's approximation, it is possible to obtain the general result about the direct relationship between the Raman scattering tensor and the electronic polarizability. The physical idea of this approximation is quite straightforward. Since in most cases of Raman scattering, $\omega_{e0} > \omega_L \gg \omega_{nn'}$, i.e., the exciting laser frequency is less than any electronic transition frequency of the system, although much larger than any vibrational frequency. In this sense, only the electrons but not the atoms can respond to the light field. Therefore, only the electronic part of the wavefunction is modified by the incident light and is the same for each atomic configuration, denoted by r , as for the system with fixed nuclei. Hence the Raman scattering tensor is equal to the electronic polarizability tensor

$$(c_{\mu\nu})_{0n,0n'} = \int \psi_{0n'}^*(r) [c_{\mu\nu}(r)]_{00} \psi_{0n}(r) dr = (\alpha_{\mu\nu})_{0n,0n'} \quad (2.18)$$

where $\psi_{0n}(r)$ is the vibrational part of wave function of configuration r and $[c_{\mu\nu}(r)]_{00}$ is the scattering tensor of the electronic ground state, which is identical with the electronic polarizability. This establishes the fundamentals of Raman selection rules; and more recently, the calculation of Raman intensity using first principles mostly relies on this approximation.

By using the same treatment as in the classical approach,

$$(\alpha_{\mu\nu})_{nn'} = (\alpha_{\mu\nu})_0 \delta_{nn'} + \left(\frac{\partial \alpha_{\mu\nu}}{\partial Q} \right)_0 Q_{nn'} \quad (2.19)$$

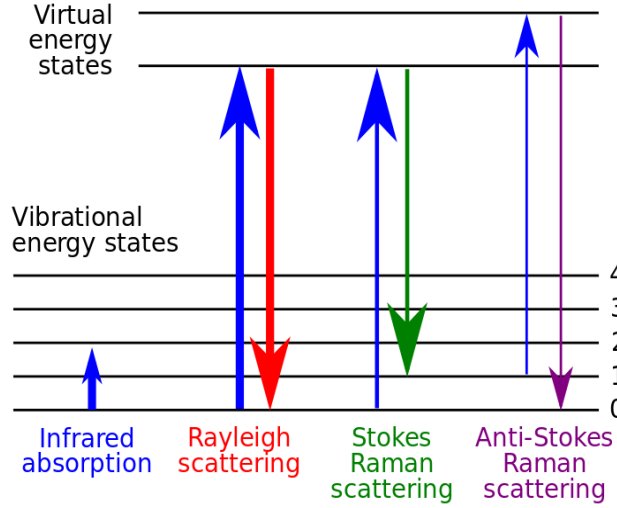


Figure 2.1: Schematic energy level diagram showing the states involved in Raman signal.

For first order Raman scattering, $n' = n \pm 1$, we can then obtain

$$I_S \propto (\omega_L - \omega_q)^4 \frac{\hbar}{2\omega_q} \alpha_{\mu\nu,Q}^2 (1 + n) \quad (2.20)$$

$$I_{AS} \propto (\omega_L + \omega_q)^4 \frac{\hbar}{2\omega_q} \alpha_{\mu\nu,Q}^2 n \quad (2.21)$$

where $\alpha_{\mu\nu,Q}$ is the short notation of $\left(\frac{\partial \alpha_{\mu\nu}}{\partial Q}\right)_0$ and the intensity ratio of Stokes and anti-Stokes scattering is

$$\frac{I_S}{I_{AS}} = \frac{(\omega_L - \omega_q)^4}{(\omega_L + \omega_q)^4} \exp(\hbar\omega_q / k_B T) \quad (2.22)$$

From Eq. 2.22 we see that the intensity of a Stokes line is larger than the intensity of the corresponding anti-Stokes line, in agreement with experiments.

The quantum perturbation theory discussed above introduces a simple and clear physical picture. As illustrated in Fig. 2.1, the photon is emitted by the perturbed system which then jumps back to its stationary state as a result. If it returns to its initial state, this gives rise to the elastic scattering, the Rayleigh scattering. With a small probability, the photon can lose or gain energy. Since the ratio of the

populations of two stationary states is proportional to $\exp(\hbar\omega_q)/k_B T$, the ratio of the intensities of a Stokes line to a corresponding anti-Stokes line is expected to be proportional to Eq. 2.22.

It should be emphasized that, the Raman scattering of light is due to the electrons of the system, and as shown in the next section, the transfer of the energy between the light and nuclei is only possible through the coupling of electrons and nuclei. It can be shown that there is no Raman scattering for a pure harmonic oscillator with frequency ω_0 . In this case, the evaluation of dipole moment matrix M_{km} only involves the phonons but not the electrons, and can be simply written as

$$(M_\mu)_{nn'} = e \left(\frac{\hbar}{2m\omega_0} \right)^{\frac{1}{2}} [(n+1)^{\frac{1}{2}} \delta_{n,n'+1} + n'^{\frac{1}{2}} \delta_{n,n'-1}] \quad (2.23)$$

It follows that the terms of Eq. 2.16 cancel off and hence the Raman scattering tensor $(c)_{n,n\pm 1}$ vanishes. It should be mentioned that Raman scattering exists for an anharmonic oscillator, however this does not mean that Raman scattering is due to anharmonic motion of the nuclei. This is only the case for the radiation which originates with the scattering from the nuclei themselves, known as the ionic Raman effect. The essential part of the normal Raman scattering by molecules and crystals, however, comes from the scattering by the electrons as presented in Eq. (2.18), and the energy transfer between the light and the motion of nuclei provides the important information of harmonicity and anharmonicity of phonons.

2.1.2.3 Loudon's Third Order Perturbation Theory

Loudon's approach explicitly assesses the scattering process of electrons, phonons and the light wave by the third-order time-dependent perturbation theory, which is theoretically equivalent to the discussion of the preceding section but more direct. [6] As proposed by Loudon, the Raman process is described by a three-step scattering process, involving three virtual electronic transitions accompanied by the energy transfer of photons and phonons. Therefore, the transition probability of the system from the state with n_i incident photons, 0 scattered photon, n_q phonons

and electron ground state (denoted by 0) to the final state with one new scattered photon and one new phonon is

$$\begin{aligned}
W(t) &= \sum_{\vec{q}, \vec{k}_s} \left| \langle n_i - 1, n_s + 1; n_q + 1; 0 | e^{-iHt/\hbar} | n_i, n_s; n_q; 0 \rangle \right|^2 \\
&= \frac{2\pi t}{\hbar^6} \sum_{\vec{q}, \vec{k}_s} \left| \sum_{m,n} \frac{\langle n_i - 1, n_s = 1; n_q + 1; 0 | H | m \rangle \langle m | H | n \rangle \langle n | H | n_i, n_s = 0; n_q; 0 \rangle}{(\omega_m - \omega_i)(\omega_n - \omega_i)} \right|^2 \\
&\quad \times \delta(\omega_i - \omega_q - \omega_s)
\end{aligned} \tag{2.24}$$

where $H = H_{ER} + H_{EP}$, the total Hamiltonian of electron–photon (radiation) and electron–phonon interactions. Followed by Eq. 2.24, the scattering ratio is

$$\frac{N_s}{N_i} \propto (n_q + 1) \frac{\omega_s}{\omega_i} \left| R_{i,s}^q(-\omega_i, \omega_s, \omega_q) \right|^2 \tag{2.25}$$

where

$$R_{i,s}^q(-\omega_i, \omega_s, \omega_q) = \frac{1}{V} \sum_{m,n} \left\{ \frac{(M_s)_{0n} (\Theta_q)_{nm} (M_i)_{m0}}{(\omega_n + \omega_q - \omega_i)(\omega_m - \omega_i)} + \text{five similar terms} \right\} \tag{2.26}$$

here the scripts of $R_{i,s}^q$ stand for the polarization directions of the incident and scattered photons i and s , and the phonon q . The two matrix elements M arise from the electron-photon Hamiltonian H_{ER} and Θ arises from the electron-phonon Hamiltonian H_{EP} . Loudon's formula is important to define some complex selection rules in the resonant Raman scattering. For example, in the case of the exciton-assisted Raman scattering on Cu_2O , the electric quadrupole and magnetic dipole transition has to be considered, and one H_{ER} term in Eq. 2.26 can be used to represent this symmetry [7, 8].

2.1.3 Group Theory and Selection Rules

2.1.3.1 Classical Approach

Selection Rule 1: A mode is Raman active only if it changes at least one of the six independent components of the polarizability tensor.

There always exists a coordinate system (x, y, z) such that the polarizability α defined in Eq. (2.1) is a diagonal matrix. Such axes are principal axes of polarizability. It is easy to find the principal axes for a symmetrical system since they must coincide with the symmetry axes.

From Eq. (2.5), we expect the normal mode Q_s will appear in the Raman spectrum if at least one of the six components of the change of polarizability, $\frac{\partial \alpha}{\partial Q_s}$, is nonzero, where the matrix form of the symmetrical tensor $\frac{\partial \alpha}{\partial Q_s}$ is

$$\left(\frac{\partial \alpha}{\partial Q_s} \right)_0 = \begin{pmatrix} \alpha_{xx,s} & \alpha_{xy,s} & \alpha_{xz,s} \\ \alpha_{yx,s} & \alpha_{yy,s} & \alpha_{yz,s} \\ \alpha_{zx,s} & \alpha_{zy,s} & \alpha_{zz,s} \end{pmatrix} \quad (2.27)$$

If for the s mode, the opposite phases of the vibration have the same bond lengths and bond angles and therefore the same charge distribution for the configurations of Q_s and $-Q_s$, the diagonal component of the polarizability, $\alpha_{\mu\mu}$ will thus have the same value for both configurations and $\alpha_{\mu\mu,s}$ is zero as a result. Take the bent XY_2 molecule, such as H_2O , for example, the anti-symmetric stretching has zero diagonal component while the other two modes, the symmetric stretching and the bending are nonzero.

For the off-diagonal component $\alpha_{\mu\nu}$ in which $\mu \neq \nu$, the handy way is to check whether the atomic 'distortion' of the mode vibration Q_s breaks the original symmetry of the system in equilibrium. If the symmetry remains the same, the property of principal axes guarantees the zero value of off-diagonal components. Otherwise, if the (x, y, z) coordinates are no longer principal, the off-diagonal components and the corresponding change will be nonzero. For H_2O molecule, the anti-symmetric stretching mode has nonzero $\alpha_{\mu\nu}$ because the x and z axes no longer remain prin-

cipal axes during the vibration of this mode, while the other two modes are zero. Therefore, all three modes in H₂O are Raman-active.

This method is simple and practical, however, for complex crystal structures, this rule is extremely difficult to apply. In the next subsection, we introduce a rigorous and systematic approach to find the selection rule, which is based on the group representation theory in quantum mechanics.

2.1.3.2 Group Theoretical Approach

Selection Rule 2: A mode s is Raman active only if the normal coordinate Q_s transforms in the same way as one of the polarizability components $\alpha_{\mu\nu}$.

Let's first present an argument that is rigorous but impractical. The intensity of the scattered light is given by Eq. (2.17), in which the component of the polarizability is explicitly calculated using Eq. (2.18). In quantum mechanics, group theory can greatly help to judge whether a given matrix element vanishes by symmetry, and in our case, the assessment of the polarizability matrix leads to the Raman selection rule. From the integral of Eq. (2.17) and unitarity of the symmetry operation group \hat{R} ,

$$\begin{aligned} \langle n' | \alpha_{\mu\nu} | n \rangle &= \int \psi_{0n'}^*(r) [\alpha_{\mu\nu}(r)]_{00} \psi_{0n}(r) dr & (2.28) \\ &= \frac{1}{g} \sum_{\hat{R}} \langle \hat{R} \psi_{0m} | \hat{R} \alpha_{\mu\nu} \hat{R}^{-1} | \hat{R} \psi_{0l} \rangle \\ &= \sum_{m', l', \mu', \nu'} \langle m' | \alpha_{\mu'\nu'} | l' \rangle \frac{1}{g} \sum_{\hat{R}} D_{mm'} D_{\mu'\nu'}^{(\alpha)} D_{ll'} & (2.29) \end{aligned}$$

where D 's are the matrix representations of the symmetry group \hat{R} with basis functions as state vectors ψ_l , where $\hat{R}\psi_l = \sum \psi_{l'} D_{l'l}$ or tensor elements $\alpha_{\mu\nu}$, where $\hat{R}\alpha_{\mu\nu}\hat{R}^{-1} = \sum \alpha_{\mu'\nu'} D_{\mu'\nu'}^{(\alpha)}$. Due to the orthogonality relation of different basis functions, a possible vibrational transition $|n\rangle$ to $|n'\rangle$ is nonzero, or Raman active, if and only if the representation $D^{(\alpha)}$ of one or more of the polarizability component

occurs in the reduction of $D^{(vib,2)} \times D^{(vib,2)}$, where the components of the polarizability tensor transform like the vector operators $x^2, y^2, z^2, xy, yz, zx$ since these tensor elements have the form of dipole \times dipole, as can be seen from Eq. (2.16). This rule is quite general, however, we have to first work out the irreducible representations of all the vibrational states and then test all possible pairs of states to see whether the transition between them is allowed. Moreover, this rule does not consider the energy difference and the order of intensity, i.e., which lines are the strong ones.

Here is a more practical approach. In accordance with Eq. (2.19), we can at least have three important conclusions for first order Raman scattering: (1) the symmetry of $\left(\frac{\partial \alpha_{\mu\nu}}{\partial Q_s}\right)_0 Q_s$ is just the symmetry of the normal mode Q_s because the derivative part is a scalar. (2) This term must always have the same symmetry of $\alpha_{\mu\nu}$ itself. (3) the Raman spectrum contains the fundamental line of frequency shift ω_s . Hence, we finally obtain the selection rule summarized on top of this section. The selection rule for infrared scattering is completely analogous, in which we can expand the dipole components in the same way. As a result, the determination of Raman-activity is reduced to testing the existence of the normal modes that transform in the same way as x^2, y^2, z^2, xy, yz or zx .

Further, since the Hamiltonian H and the symmetry operations \hat{R} commute, any group member of symmetry operations cannot transform one mode to another with a different dynamic eigenvalue, i.e., under the irreducible representations of H , and the H matrix is diagonal, the matrix of \hat{R} must be blocks of irreducible representations of the symmetry group, and the rank of each block equals to the degeneracy of the corresponding normal mode. The physical idea for this irreducibility in lattice vibration is a normal mode coordinate Q_s is decoupled from other normal coordinates. As a result, the displacement pattern of a normal mode is invariant under the symmetry operation and hence $\hat{R}Q_s$ must have the same frequency. One simple illustration of the matrix representations of H and \hat{R} under the eigenbasis of H , with one doubly degenerate and two single modes, is

$$H = \begin{pmatrix} \lambda_1 & 0 & 0 & 0 \\ 0 & \lambda_1 & 0 & 0 \\ 0 & 0 & \lambda_2 & 0 \\ 0 & 0 & 0 & \lambda_3 \end{pmatrix} \iff \hat{R} = \begin{pmatrix} \times & \times & 0 & 0 \\ \times & \times & 0 & 0 \\ 0 & 0 & \times & 0 \\ 0 & 0 & 0 & \times \end{pmatrix} \quad (2.30)$$

Accordingly, we can group the modes in accordance with the irreducible representation of the symmetry of molecules or crystals. More explicitly, since H and \hat{R} own the same eigenbasis, we can fully understand the symmetry of modes by means of \hat{R} , instead of H itself.

Combining the arguments discussed above, we obtain the following mathematical statement about how to apply the Rule 2: we need to transform the corresponding symmetry group to a sum of irreducible representations (in a form that looks like the above illustrative example), and the modes belonging to the representations that inherit the symmetry of vector products $x^2, y^2, z^2, xy, yz, zx$ are expected to be Raman active.

2.1.3.3 The Correlation Method

Although the rule derived from group theory is mathematically handy, the irreducible decomposition is still nontrivial, and sometimes complicated. The correlation method that relates the site symmetry of a system to the corresponding crystallographic point symmetry offers a convenient way generating the selection rule. In this section, we follow the approach described by Inui *et al.* [9]

To understand this method, we need some definitions and fundamental theories.

Site Group S : The site is defined as a point which is left invariant by some operations of the space group. These operations may be shown to form a group which is called the site group. Every point is thus a site, having at least the trivial site group C_1 .

Point Group G_0 : For a space group G , rotational parts of the symmetry operations will form a group G_0 , which is a crystallographic point group. Evidently, S is

a subgroup of G_0 .

Factor Group G/T : The translation group T forms an invariant subgroup of the space group G . Therefore, the cosets of the translation group T in the space group G form a factor group G/T , and it is isomorphic to the point group G_0 , though some of the cosets may contain other than pure point operations combined with screws or glides.

This is indeed the group theoretical counterpart of the Bloch theorem, in which, the Bloch functions are actually the basis functions for the irreducible representation of T and inherit all the translational symmetry of the crystal. The wavevector \vec{k} designates the representation of the translation group with the character $\exp(i\vec{k} \cdot \vec{r})$. At Γ point, the G_0 symmetry is maintained for the obvious reason, in consequence, for 1st order Raman scattering, the G_0 symmetry determines the activity of spectra. However, it should be noted that \vec{k} generally cannot have the whole symmetry of G_0 but constitutes a subgroup, this explains the change of Raman activity when going to higher order Raman scattering in which \vec{k} is not at the Γ point, for example, overtone or combinational bands in Raman.

Since the normal coordinates are linear combinations of the $3N$ atomic displacements, the correlation method starts with the irreducible representation of the site group S , and tries to transform to the point group symmetry of the system. Obviously, under the site group's operation, one atom will never be moved away to another position, the 'mutual exclusion' implies that the bases for the irreducible representations are simply composed of the xyz coordinates (or displacements) of each individual atom, with no superposition of other atoms. Therefore, the irreducible representations of the site group are easily identified by picking out those representations with T_x , T_y or T_z symmetry, which are followed by the basis vectors x , y and z . Then, we can relate the site representation to the factor representation by examining the character χ (the trace of the group representation). Under the transformation between these two representations, the trace of the matrix is a constant. As a result, the character of i th irreducible representation of the factor group is just the same as that of the site group, or the sum of several irreducible representations

of the site group (because the symmetry of factor group is higher, the degeneracy of the factor group can be lifted), i.e.,

$$\chi_f^{(\beta)}(\hat{R}) = \sum_{(\alpha)} a_{\beta\alpha} \chi_s^\alpha(\hat{R}) \quad (2.31)$$

where s and f stand for site and factor respectively. This provides a straightforward way to construct the correlation between two groups by comparing the character tables.

When irreducible matrices of a representation is derived, we can define a projection operator

$$P^{(\beta)} f = \frac{d_\beta}{g} \sum_{\hat{R}} \chi^{(\beta)}(\hat{R})^* \hat{R} \quad (2.32)$$

Consider an arbitrary function f , it will contain in general, basis functions of various irreducible representations

$$f = \sum_{\beta} \sum_m c_m^{(\beta)} \phi_m^{(\beta)} \quad (2.33)$$

where $\phi_m^{(\beta)}$ are basis functions for the irreducible representation $D^{(\beta)}$, and $c_m^{(\beta)}$ are coefficients of the expansion. For the vibration spectra, $\phi_m^{(\beta)}$'s are the normal coordinates Q 's for the mode β .

When applied to f , $P^{(\beta)}$ will project f onto the subspace of the representation $D^{(\beta)}$.

$$P^{(\beta)} f = \sum_m c_m^{(\beta)} \phi_m^{(\beta)} \quad (2.34)$$

In practice, for the Raman spectra, we can take f as the displacement of one atom. Examples of the rutile and cuprite structures are presented in Appendix B. More examples can be found in the manual book written by Fateley *et al.* [10]

2.2 Time of Flight Inelastic Neutron Scattering

2.2.1 Introduction

Neutron scattering is a powerful technique for studying lattice dynamics. One advantage stems from the fact that the wavelength of a neutron is of the same order of magnitude as the interatomic distances in crystals. Therefore, it has good resolution in reciprocal space and is able to probe phonons in the whole Brillouin zone. A historical disadvantage of neutron scattering is the relatively poor energy resolution, due to the low intensity of available neutron beams. This situation has changed with low background and high neutron flux at the Spallation Neutron Source (SNS) at the Oak Ridge National Laboratory.

In our work, inelastic neutron scattering is used to investigate the phonon densities of states. The measurements were performed with the wide angular-range chopper spectrometer (ARCS) at SNS at the Oak Ridge National Laboratory. In this section, we briefly review the basic principles and experimental techniques of inelastic neutron scattering and its applications in the study of lattice dynamics. More detailed discussions about theories of inelastic neutron scattering can be found, for example, in [11,12].

2.2.2 Basic Principles

2.2.2.1 Scattering Cross Section

When a beam of monoenergetic thermal neutrons is incident on a sample, the neutrons may be either scattered, absorbed or pass with no interaction. The process of neutron scattering is characterized by the cross section σ . The scattered intensity is usually described by the partial differential cross section, which is defined to be

$$\frac{d^2\sigma}{d\Omega dE} = \frac{\text{number of neutrons scattered per second into solid angle } d\Omega \text{ with energy } E}{\text{incident neutron flux}} \quad (2.35)$$

The strength of the a neutron-nucleus interaction is described by the scattering

length b , which in general is a complex quantity (the imaginary part gives the neutron absorption). Since nuclear forces are short in range compared to the neutron wavelength, in the first order Born approximation the interaction potential between the neutron and the nucleus at \vec{R} can be approximated by the Fermi pseudopotential

$$V(\vec{r}) = \frac{2\pi\hbar^2 b}{m} \delta(\vec{r} - \vec{R}) \quad (2.36)$$

The cross section is evaluated in the Born approximation. The incoming neutrons are represented by plane wave functions, and the transition probability is given by Fermi Golden rule, together with the Fermi pseudopotential, we can obtain

$$\frac{d^2\sigma}{d\Omega dE} = \frac{k_f}{k_i} \frac{1}{2\pi\hbar} \sum_{l,l'} b_l b_{l'} \times \int_{-\infty}^{\infty} \langle \exp[-i\vec{Q} \cdot \vec{R}_{l'}(0)] \exp[i\vec{Q} \cdot \vec{R}_l(t)] \rangle \exp(-i\omega t) dt \quad (2.37)$$

where $\vec{Q} = \vec{k}_i - \vec{k}_f$ is the momentum transfer to the sample, and $\omega = (E_i - E_f)/\hbar$ is the energy transfer to the sample.

2.2.2.2 Coherent and Incoherent Scattering

The cross section in Eq. 2.37 contains products of pairs of scattering lengths, which can be written as the sum of a correlated part and an uncorrelated part

$$\overline{b_l b_{l'}} = \overline{b}^2 + \delta_{ll'} (\overline{b^2} - \overline{b}^2) \quad (2.38)$$

The coherent scattering is proportional to the average value \overline{b} , and incoherent scattering arises from the distribution of the deviations from \overline{b} . Only a system with an average scattering length can give interference effects.

As a result, the cross section can be split in a coherent part

$$\left(\frac{d^2\sigma}{d\Omega dE} \right)_{coh} = \overline{b}^2 \frac{k_f}{k_i} \sum_{l,l'} \int_{-\infty}^{\infty} \langle \exp[-i\vec{Q} \cdot \vec{R}_{l'}(0)] \exp[i\vec{Q} \cdot \vec{R}_l(t)] \rangle \exp(-i\omega t) dt \quad (2.39)$$

and an incoherent part

$$\left(\frac{d^2\sigma}{d\Omega dE}\right)_{inc} = (\bar{b}^2 - \bar{b}^2) \frac{k_f}{k_i} \sum_l \int_{-\infty}^{\infty} \langle \exp[-i\vec{Q} \cdot \vec{R}_l(0)] \exp[i\vec{Q} \cdot \vec{R}_l(t)] \rangle \exp(-i\omega t) dt \quad (2.40)$$

These equations show that coherent scattering depends on the correlations between different scatterers at different times, while the incoherent scattering involves only the correlations between the positions of the same scatterer at different times. The coherent and incoherent scattering for different elements can be quite different. For example, the scattering is mostly coherent for vanadium-50 but incoherent for vanadium-51.

Consider a crystal as a target for the thermal neutron beam. The position of a nucleus at time t is given by $\vec{R}_l = \vec{r}_l + \vec{u}_l(t)$, in which \vec{r}_l is the equilibrium position of the atom in the Bravais lattice, and $\vec{u}_l(t)$ is the displacement. Insert the expression for \vec{R}_l into Eq. 2.39 and notice that the correlation between atoms at \vec{r}_l and $\vec{r}_{l'}$ in a Bravais lattice depends only on $\vec{r}_l - \vec{r}_{l'}$, we get

$$\left(\frac{d^2\sigma}{d\Omega dE}\right)_{coh} = \bar{b}^2 \frac{k_f}{k_i} \sum_l \exp(i\vec{Q} \cdot \vec{r}_l) \times \int_{-\infty}^{\infty} \langle \exp[-i\vec{Q} \cdot \vec{u}_0(0)] \exp[i\vec{Q} \cdot \vec{u}_l(t)] \rangle \exp(-i\omega t) dt \quad (2.41)$$

Expressing the displacements \vec{r}_l in the second quantization form as derived in Eq. 1.9, one can show that [11]

$$\langle \exp[-i\vec{Q} \cdot \vec{u}_0(0)] \exp[i\vec{Q} \cdot \vec{u}_l(t)] \rangle = \exp[\langle Q^2 u_0^2(0) \rangle] \exp[\langle \vec{Q} \cdot \vec{u}_0(0) \vec{Q} \cdot \vec{u}_l(t) \rangle] \quad (2.42)$$

where the first factor $\exp[\langle Q^2 u_0^2(0) \rangle]$ corresponds to the Debye-Waller factor, $\exp(-2W)$.

The partial cross section of Eq. 2.41 can be rewritten as

$$\left(\frac{d^2\sigma}{d\Omega dE}\right)_{coh} = \bar{b}^2 \frac{k_f}{k_i} e^{-2W} \sum_l \exp(i\vec{Q} \cdot \vec{r}_l) \times \int_{-\infty}^{\infty} \exp[\langle \vec{Q} \cdot \vec{u}_0(0) \vec{Q} \cdot \vec{u}_l(t) \rangle] \exp(-i\omega t) dt \quad (2.43)$$

If we expand the second exponential factor of Eq. 2.42 in a Taylor series, Eq. 2.43 has a quite clear physical meaning. It just gives the multi-phonon expansion

which describes zero, first, second...order processes. The zero-th term corresponds to elastic scattering, the first-order term corresponds to the one-phonon process, the second-order term corresponds to the two-phonon process and so on. The coherent one-phonon scattering process can be considered as elastic scattering on a moving target crystal, while higher-order processes give a broad distribution in the momentum and energy space and can be considered as the background [11].

The evaluation of the incoherent scattering, Eq. 2.40, is similar. The exponent can be expanded in a power series, and the n th term corresponds to the n -phonon process. As compared to the coherent cross section, there is only the energy conservation factor, therefore, the measurement of the incoherent scattering provides information only on the number of phonon modes as a function of energy but not on the dispersion relations.

2.2.3 Wide Angular-Range Chopper Spectrometer (ARCS)

Thermal neutrons can be produced in a nuclear reactor by a chain reaction of nuclear fission or by spallation reactions with heavy metals. An important experimental work on Ag_2O presented in this thesis made use of time-of-flight inelastic neutron scattering (INS) performed with the Wide Angular-Range Chopper Spectrometer (ARCS) at the Spallation Neutron Source (SNS) at the Oak Ridge National Laboratory [13]. The source of the neutrons is the spallation of neutrons from a mercury target bombarded with high energy protons. The SNS is currently the most powerful neutron source in the world.

The initial energies of the neutrons are too high for materials science research, and they are slowed down by passing through cells filled with water. The pulsed neutron beam is then directed to the instrument through neutron guides, inside of which the neutrons undergo total reflection, so the loss of intensity is negligible. Two choppers rotating with different frequencies allow selection of the incident energy E_0 of neutrons. The first chopper is more massive and stops high energy neutrons and other background radiation. The second chopper, usually called a

Fermi chopper, is smaller and used for further tuning the energy distribution of the neutron bunch. The schematic overview of the design is presented in Fig. 2.2.

Usually ^3He -filled tubes are used for neutron detection, since a charge is produced after a neutron is captured by a ^3He nucleus. ARCS has 115 packs of eight 1-meter-long tubes. Each is sensitive to linear position. The time the neutrons take to reach the sample is fixed, while the time they take to reach the detector depends on the distance to that particular pixel and the energy lost to or gained from phonons in the sample. The change in neutron momentum is also calculated from the position of the detector. The raw data from ARCS is a 'neutron event' record, i.e., for every neutron detected, the detector number and position as well as the time-of-flight of the neutron are saved into a data file.

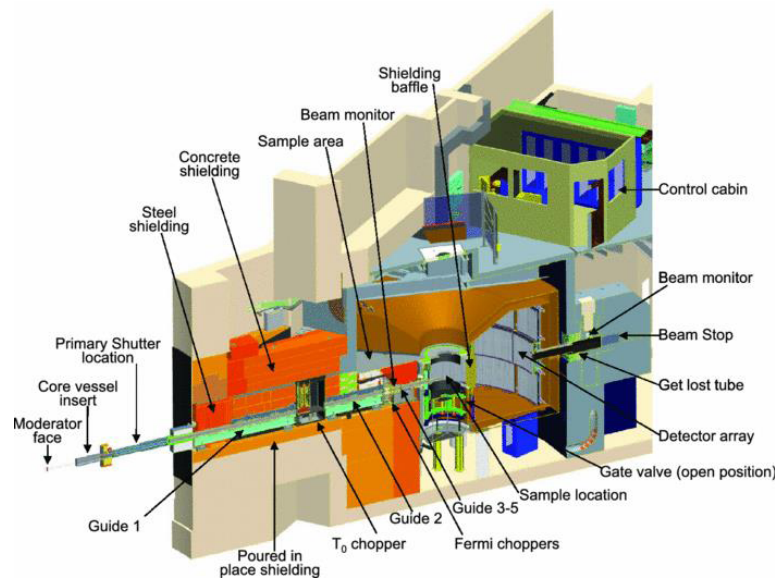


Figure 2.2: Schematic overview of the ARCS design with components labeled [13]

2.2.4 Data Reduction

For ARCS, the incident energy is more accurately determined than in older instruments and the performance of the detectors is also superior. ARCS samples a large part of (\vec{Q}, E) , which helps to improve the accuracy of experimental phonon DOS.

However, the data reduction of inelastic neutron scattering is still a complicated task, not only due to the difficulty of binning a large amount of data, but also due to the complexity of multiphonon and multiple scattering corrections. The detailed principles and procedures are documented elsewhere [12–14], and the development of the corresponding software package was an important part of the DANSE project [15]. Here, we give a brief overview about the data reduction procedures for ARCS.

The raw data are processed to obtain $I(\vec{Q}, E)$ histograms. The binning of the energy transfer and the momentum transfer are the main variable at this stage, and there is a trade-off between the two axis in terms of counting statistics. The binning used for the present work, 0.5 meV per energy bin and 0.1 Å per momentum bin, is fairly standard.

The background subtraction is performed next. A measurement under the same experimental conditions and sample environment is done, but without the sample. This accounts for most of the real contribution from the background. At ARCS the instrument background is quite low because it is almost completely shielded by neutron-absorbing materials, including in between detector packs. Most of the background comes from the sample environment.

Neutron-weighted phonon DOS curves are obtained from the $I(\vec{Q}, E)$ histograms, using getDOS, part of the DANSE software. For incoherent scatterers of neutrons, the phonon DOS is obtained by integrating over the Q axis. The subtraction of the elastic scattering is done by assuming an E^2 scaling of the intensity of the phonon DOS and fitting the elastic peak to a Gaussian. The main issue that the code deals with is the determination and subtraction of multiphonon scattering, which is solved by an iterative method: the n -phonon scattering can be written as the convolution of the 1- and $(n-1)$ -phonon scattering and this leads to a recursion relation for all the orders of scattering, with one adjustable parameter. A detailed description of the getDOS and underlying principles is given in [12, 14]

Chapter 3

Computational Methodologies

3.1 Density Functional Theory

3.1.1 Introduction

The fundamental principle of density function theory (DFT) is that any property of a system of many-body interactions can be viewed as a functional of the ground state density, which, in principle determines all the information for the ground state. The existence proof was given by Hohenberg and Kohn [16]. Kohn and Sham then provided an approach to make ground state functionals for real systems of many electrons [17]. The remarkable successes of the functionals of local density approximation (LDA) and generalized gradient approximation (GGA) within the Kohn-Sham approach lead to widespread interests and applications in DFT. Here, we briefly review the DFT theory. More theoretical details on this subject can be found in [18].

3.1.2 Hohenberg-Kohn Theorems

For a system of electrons and nuclei in an external potential $V_{ext}(\vec{r})$, the Hamiltonian can be written

$$H = -\frac{\hbar^2}{2m_e} \sum_i \nabla_i^2 + \sum_i V_{ext}(\vec{r}_i) + \frac{1}{2} \sum_{i \neq j} \frac{e^2}{|\vec{r}_i - \vec{r}_j|} + \hat{H}_{nn} \quad (3.1)$$

where $V_{ext}(\vec{r})$ includes interactions of electrons and nuclei and any other external fields, and \hat{H}_{nn} is nuclei-nuclei interaction potential.

The first theorem states that for this system, the potential $V_{ext}(\vec{r})$ is determined uniquely, except for a constant, by the ground state electron density $n_0(\vec{r})$. Since the Hamiltonian is fully determined, it follows that all properties of the system are completely determined given only the ground state density.

The second theorem states that given the external potential there exists a unique energy functional $E[n(\vec{r})]$, and the exact ground state energy of the system is the global minimum value of this functional, and the density $n(\vec{r})$ that minimizes the

functional is the exact ground state density $n_0(\vec{r})$.

According to the first theorem, the ground state energy functional can be written in the form

$$E[n(\vec{r})] = T[n(\vec{r})] + E_{int}[n(\vec{r})] + \int d^3r V_{ext}(\vec{r})n(\vec{r}) + E_{nn} \quad (3.2)$$

$$= F_{HK}[n(\vec{r})] + \int d^3r V_{ext}(\vec{r})n(\vec{r}) + E_{nn} \quad (3.3)$$

where the functional $F_{HK}[n(\vec{r})]$ includes kinetic and potential energies of the interacting electron system. It follows from the second theorem that if the functional $F_{HK}[n(\vec{r})]$ is known, then by minimizing the total energy of the system with respect to the density $n(\vec{r})$, the exact ground state energy and density are determined.

Notice that, although the density is in principle sufficient, Hohenberg-Kohn theorems do not provide a guidance for constructing the functional $F_{HK}[n(\vec{r})]$, and no exact functional is known for any system of more than one electron.

3.1.3 Kohn-Sham Theory

The task of finding good approximations to the energy functional is greatly simplified by Kohn-Sham theory [16,17]. The key of the success of Kohn-Sham approach is that it replaces the interacting many-body system with an auxiliary non-interacting system with the electron density equal to the original interacting system. Accordingly, the Hohenberg-Kohn expression for the ground state energy functional can be rewritten as

$$E_{KS} = T_0[n] + \int d^3r V_{ext}(\vec{r})n(\vec{r}) + \frac{1}{2} \int d^3r d^3r' \frac{n(\vec{r})n(\vec{r}')}{|\vec{r}_i - \vec{r}_j|} + E_{nn} + E_{xc}[n(\vec{r})] \quad (3.4)$$

where T_0 is the kinetic energy that a system with density n would have if there were no electron-electron interactions. The second integral is the classical Coulomb interaction energy of electrons, or the Hartree energy. All many-body effects of

exchange and correlation are grouped into the exchange-correlation energy E_{xc} . Evidently, in Eq. 3.4, all the terms but the exchange-correlation energy can be evaluated exactly, so the approximation for E_{xc} plays the central role. Comparing Eq. 3.2 and Eq. 3.4, we can obtain

$$E_{xc}[n(\vec{r})] = T[n(\vec{r})] - T_0[n(\vec{r})] + E_{int}[n(\vec{r})] - E_{Hartree}[n(\vec{r})] \quad (3.5)$$

One can see clearly that E_{xc} is the difference of the kinetic and the internal interaction energies of the interacting system from those of the auxiliary independent-electron system with Hartree energy $E_{Hartree}$.

If we apply the variational principle to Eq. 3.4, we can obtain the Kohn-Sham Schrödinger equation:

$$\left(-\frac{1}{2}\nabla^2 + V_{KS}(\vec{r}) - \epsilon\right)\Phi(\vec{r}) = 0 \quad (3.6)$$

with

$$V_{KS}(\vec{r}) = V_{ext}(\vec{r}) + \frac{\delta E_{Hartree}}{\delta n(\vec{r})} + \frac{\delta E_{xc}}{\delta n(\vec{r})} \quad (3.7)$$

as we will discuss later, efficient methods exist for solving the single particle Schrödinger equation with a local effective potential to yield

$$n(\vec{r}) = \sum_i |\Phi_i(\vec{r})|^2 \quad (3.8)$$

and all quantities derivable from it. There are many advantages of Kohn-Sham approach. For example, in contrast to the Hartree-Fock approach, the effective potential V_{KS} is local. Also, in contrast to Thomas-Fermi approach where a large kinetic energy term is approximated, only the small exchange energy and the even smaller correlation contribution require approximation.

3.1.4 Functionals for Exchange and Correlation

The crucial quantity in the Kohn-Sham approach is the exchange-correlation energy, which is also the main approximation of DFT. Although the exact E_{xc} functional

must be complicated, great progress has been made with simple approximation, and remarkable accuracy has been achieved. A widely used approximation, the local density approximation (LDA) is to postulate that the exchange-correlation functional has the following form [19,20]

$$E_{xc}^{LDA} = \int n(\vec{r})\epsilon_{xc}(n(\vec{r}))d\vec{r} \quad (3.9)$$

Here the function $\epsilon_{xc}(n(\vec{r}))$ for the homogeneous electron gas is numerically known by, for example quantum Monte Carlo method. The basic idea of LDA is that the exchange-correlation energy can be found by dividing the system in infinitesimally small volumes with a constant density, and each small volume contributes to E_{xc} by an amount equal to the exchange-correlation energy of a homogeneous electron gas with the same electron density as the original system. It is therefore expected that LDA will be good for solids close to a homogeneous gas with a slowly varying density, like a nearly free-electron metal. But surprisingly, LDA appears to be very accurate in many other cases too. No law guarantees the accuracy of this approximation, but LDA is a reasonable guess. The reason is that the range of the effect of exchange and correlation is local and rather short, and furthermore, the detailed shape of the exchange-correlation need not be correct since only the average enters the energy.

The success of LDA has led to the development of various improved functionals, such as the generalized-gradient approximations (GGA). GGAs make the exchange-correlation contribution of every infinitesimal volume dependent not only on the local density, but also on the density in the neighboring volumes. Therefore the gradient of the density plays a role, and there are numerous GGA forms that have been proposed to modify the behaviors of gradients, for example, the widely used forms of Perdew and Wang (PW91) [21], and Perdew, Burke and Enzerhof (PBE) [22]. In general, GGAs perform slightly better than LDA, however, in many GGAs, some free parameters are used to fit experimental data, which make them not strictly *ab initio*.

3.1.5 Pseudopotentials

Up to now, the Kohn-Sham single particle Schrödinger equation, Eq. 3.6, has been well defined. To solve it, it is necessary to express the single particle orbitals Φ with a basis set. The common approaches include a plane wave basis set or a Gaussian wave basis set. Having chosen a basis, we can tackle Eq. 3.6 as an eigenvalue problem, and a self-consistent iteration and a matrix diagonalization process can be performed numerically. However, it might be clear that Φ belongs to a function space with infinite dimensions, and the number of basis functions is therefore infinite in principle. In practice, we have to truncate the basis somehow to realize the compromise between speed and accuracy. For plane waves, this can be easily done by limiting the set to k with $k < K_{max}$. In the valence part far away from the nuclei, the wave function behaves like a plane wave and hence only a small K_{max} is needed. However, in the region near the nuclei (about 0.1 \AA), the wave function shows sharp changes, and a wavelength as small as an order of magnitude less than this dimension is required, which roughly corresponds to 10^8 plane waves, way beyond the capability of any computer.

The solution is to replace the potential in the oscillating core region by a pseudopotential (PP) which is designed to have smooth wave functions inside this region. This idea, which is usually called the ‘muffin-tin’ approach, came out much earlier for the calculation of electron band structures before the use of DFT [23,24], but the wide applications of DFT greatly pushed the development of pseudopotential models. There is a big family of pseudopotentials that are actively in use for DFT calculations. In the augmented plane wave (APW) PP, the wave functions take a hybrid form with the core part using a basis of atomic orbitals, e.g., spherical harmonics, and the valence part using standard plane waves. In the norm-conserving PP, the electron charge within the core region is equal to that of the actual atom [25]. The ultrasoft PP does not conserve the charge, but instead reduces the height of the peak of the potentials to reduce the number of plane waves needed to represent the wave functions [26]. The more recent projector augmented wave (PAW) PP begins

with a plane wave basis set, but then it adopts a set of projection operators to reintroduce the wave functions of the core electrons into the calculation. Essentially, this method retains the full all-electron wave function and charge density [27,28]. We used PAW and Ultrasoft PPs for the work presented in this thesis.

3.2 Molecular Dynamics Methods

3.2.1 Introduction

One possible way of simulating the behavior at a finite temperature is by allowing the system to evolve in real time according to a dynamical equation. This is called molecular dynamics (MD) simulation [29–31]. For nuclei, since they behave as classical particles in usual cases, the dynamics is usually governed by Newton's second law. However, when the temperature is low, for instance in solids when the temperature is much lower than Debye temperature, quantum effects should be taken into consideration [32,33].

MD simulations are commonly classified according to how the interatomic forces are calculated. Classical MD uses simple multiple particle potentials in analytical forms. For example, for solids, a Buckingham potential or a Morse potential is often adopted. Training a classical potential is usually performed by fitting the target functions to the structural and/or thermodynamical properties of the system, or by fitting to the simulated potential surface from first principles methods. Although a MD with classical potential in general has lower accuracy than first-principles methods because of the quality of potential surface in use, the speed is several orders of magnitude faster than its counterpart, and is hence valuable for studies requiring long simulation times and big system sizes. Developing classical potentials is therefore a very active research field.

First-principles MD, on the other hand, uses DFT methods to obtain the interatomic forces. First-principles MD includes two common categories: Born-Oppenheimer MD (BOMD) and Car-Parrinello MD (CPMD) [34]. For BOMD, the

electronic states are relaxed to the ground states by solving DFT equations at each time step, and the interatomic forces are calculated from there. CPMD couples the electronic degrees of freedom into the classical coordinate system by assigning electrons a fictitious mass. The main benefit of a CPMD approach is the reduction in computational expense but the convergence of CPMD is usually poorer than BOMD.

In the work presented in this thesis, MD simulations were used extensively. For example, to study anharmonic phonon effects, we used classical MD simulations for rutile TiO_2 , and we used BOMD for Ag_2O .

3.2.2 Solving Equations of Motion

The central role of MD simulation is to capture the trajectories of atoms in time, e.g., positions \vec{r}_i , velocities \vec{v}_i and accelerations \vec{a}_i . Given a position $\vec{r}(t)$ at time t , we can write down its evolution for a small time step Δt forward and backward,

$$\vec{r}(t + \Delta t) = \vec{r}(t) + \vec{v}(t)\Delta t + \frac{1}{2}\vec{a}(t)\Delta t^2 + \frac{1}{3!}\frac{d^3\vec{r}(t)}{dt^3}\Delta t^3 + \dots \quad (3.10)$$

$$\vec{r}(t - \Delta t) = \vec{r}(t) - \vec{v}(t)\Delta t + \frac{1}{2}\vec{a}(t)\Delta t^2 - \frac{1}{3!}\frac{d^3\vec{r}(t)}{dt^3}\Delta t^3 + \dots \quad (3.11)$$

and hence

$$\vec{r}(t + \Delta t) = (2\vec{r}(t) - \vec{r}(t - \Delta t)) + \vec{a}(t)\Delta t^2 + O(\Delta t^4) \quad (3.12)$$

$$\vec{a}(t) = -\frac{1}{m} \frac{dV}{d\vec{r}(t)} \quad (3.13)$$

This is the Verlet algorithm for solving Newton's equation numerically [35]. At each step, the acceleration is evaluated from the potential, and then the position of each atom can be updated. Note that the equation is correct to third order in Δt because the change in acceleration cancels. The preference of Verlet algorithm over, for example, the Runge-Kutta method which is commonly used in solving differential equations, is that it is time-reversible. This tends to improve energy conservation

over long simulation times. The Verlet algorithm has disadvantages, however. For example, the term proportional to Δt^2 may lead to numerical truncation error because it is small compared with $2\vec{r}(t) - \vec{r}(t - \Delta t)$. Moreover, this algorithm does not have velocities shown explicitly, which is a problem while the simulation is for a system that is in contact with constant temperature reservoir. The latter problem in the Verlet algorithm can be remedied by the velocity Verlet algorithm which includes an analogous expansion of velocity in the Verlet equations [36], in the form

$$\vec{v}(t + \Delta t) = \vec{v}(t) + \frac{1}{2}[\vec{a}(t) + \vec{a}(t + \Delta t)]\Delta t \quad (3.14)$$

The time step Δt is an important parameter for a MD simulation. Evidently, as the time step decreases, the numerically calculated trajectory is expected to become closer and closer to the true trajectory, but the computational cost increases accordingly. In practice, the limit of the maximum time step is determined by the rate of the fastest process in the system. In the case of lattice vibrations, the time step is typically a few femtoseconds, an order of magnitude smaller than the vibrational period of the phonon mode of highest energy.

3.2.3 Ensembles

A standard MD simulation generates an *NVE* ensemble, i.e., a microcanonical ensemble that preserves the total energy and volume, with the temperature and pressure fluctuating. The *NVE* ensemble is the natural ensemble of MD, but it is usually not a natural ensemble in nature. Fortunately, it is also possible to generate other ensembles, for example, the *NVT* and *NPT* ensembles. The *NVT* ensemble is a canonical ensemble that is coupled to a heat bath. In practice, this can be realized by the *Nosé-Hoover* method [37, 38]. The *Nosé-Hoover* method is similar to the extended Lagrange method and can produce a true canonical ensemble. In this method, a fictitious mass and its related degree of freedom is added to the system to simulate the coupling with the heat bath by scaling the timescale and adding a potential term. In the *NPT* ensemble, the pressure can also be controlled

by coupling to a pressure bath. Although these ensembles seem to be closer to realistic conditions, some fictitious parameters are added. The choices of these parameters are crucial to maintain the properties of the ensemble and stability of the system, and require tests and experiences to adjust. Therefore, it may be advantageous to use an ensemble that achieves the target condition, and then switch back to the simple *NVE* ensemble for the long time production run.

3.3 Phonon Calculations

3.3.1 Introduction

The methods and algorithms for calculating anharmonic phonons and analyzing anharmonic behavior are central topics of this thesis. In this section we give a brief overview of two popular approaches for calculating phonons, the small displacement method and the density functional perturbation approach. Both of these methods focus on the calculation of force constants based on harmonic lattice dynamics. We adopted these methods to calculate the harmonic or quasiharmonic phonons for further analysis. We focus more on the molecular dynamics approach and the velocity autocorrelation method that we developed to study the phonon anharmonicity. We also discuss how we developed an anharmonic fitting algorithm based on the phonon perturbation theory and the application of this method.

3.3.2 Lattice Dynamics Approach

3.3.2.1 Small Displacement Method

The small displacement method is a direct method that calculates the force constant matrix of the vibrating system by displacing the atoms of the system explicitly. As we discussed in Section 1.2, the force constant matrix or its Fourier transformed form, the dynamical matrix, is the key to phonon solutions. In this method, some atoms are displaced and the forces induced by this displacement can be calculated.

In fact, it is not necessary to displace all the atoms in the primitive cell since the use of symmetries can reduce the amount of work.

In first-principles DFT methods, the calculation of forces is based on the use of Hellmann-Feynman theorem. If we consider the ground state energy $E(\lambda)$ and wave function $\Phi(\lambda)$ to be parameterized by some parameter λ , then the change in $E(\lambda)$ incurred by a change in λ is given by

$$\frac{\partial E(\lambda)}{\partial \lambda} = \langle \Phi(\lambda) | \frac{\partial H}{\partial \lambda} | \Phi(\lambda) \rangle \quad (3.15)$$

Accordingly, the force on the nucleus I at \vec{X}_I is thus

$$\vec{F}_I = -\langle \Phi | \frac{\partial H}{\partial \vec{X}_I} | \Phi \rangle \quad (3.16)$$

Feynman showed this to be the electrostatic force on the displaced nucleus.

Similar treatment of displacements can be used to study the potential surface of one particular phonon mode. In the so called "frozen" phonon method, one picks a phonon mode for the system and applies a displacement field corresponding to this phonon described by the polarization vector e_s and a displacement amplitude u . By calculating the total energy for a set of displacement configurations varied by u , one obtains the deformation potential for this phonon. This potential curve is typically parabolic around the equilibrium configuration, but for larger displacements, anharmonic components in the potential become more important. The advantage of this method is that it provides the potential for the atomic displacements not limited to the harmonic approximation. However, it should be noticed that although some anharmonic effect is seen from this approach, this potential surface is only for this particular mode and therefore the contributions of phonon-phonon interactions still cannot be evaluated.

3.3.2.2 Density Functional Perturbation Method

The density functional perturbation theory (DFPT) is an advanced and fast developing branch of DFT calculations, and the calculation of phonons is one of its important applications [39,40]. In principle, DFPT can also be applied to calculate some physical quantities related to anharmonic phonon effects, for example, the third order phonon coupling tensors. These applications are more complicated to implement and are active research fields.

The idea of DFPT is based on the linear response theory and DFT. Since the electron density is the fundamental quantity in DFT, we are interested in the changes to first order of electron density in response to an external perturbation. The change of electron density can be used to derive many physical quantities.

$$\delta n(\vec{r}) = \int d\vec{r}' \chi(\vec{r}, \vec{r}') \delta V^{ext}(\vec{r}') \quad (3.17)$$

where χ is the coefficient of linear response in response to the potential perturbation δV^{ext} , and is usually called a susceptibility. It is non-local because the change of density somewhere will induce changes everywhere by electron-electron interaction. In the case of phonons, the perturbed potential is the displacement described by the phonon polarization vector. Once $\delta n(\vec{r})$ is calculated, the dynamical matrix can be easily derived because the second derivative of the energy can be simply expressed as the integral form of the first derivative of electron density $n(\vec{r})$ and potential according to the well-known "2n+1" theorem [40].

From basic quantum perturbation theory, it is easy to show that the susceptibility χ_0 , which is the linear response coefficient for the total potential change, i.e., $\chi_0^{-1}(\vec{r}, \vec{r}') = \frac{\delta V^{total}}{\delta n(\vec{r})}$, is

$$\chi_0(\vec{r}, \vec{r}') = \sum_{i,j} (f_i - f_j) \frac{\Phi_i(\vec{r})^* \Phi_j(\vec{r}') \Phi_j(\vec{r}')^* \Phi_i(\vec{r})}{\epsilon_i - \epsilon_j} \quad (3.18)$$

where f 's are the electron occupation factors at zero temperature. It should be

noted that although the DFPT involves Kohn-Sham eigenstates and eigenvalues of which the meaning is not very clear, they are just intermediate states. The real problem comes from the computational cost because Eq. 3.18 scales as $O(n^4)$. The computational complexity can be reduced to $O(n^2)$ by using a projection operator to avoid the evaluation of conduction bands.

3.3.3 Molecular Dynamics Approach

3.3.3.1 Time-Correlation Method

MD simulation is a perfect tool to investigate phonon anharmonicity because it naturally includes all effects of anharmonicity in the trajectories while the system is evolving dynamically. MD simulations should be reliable for calculating phonon spectra in strongly anharmonic systems, even when the QHA, or perturbation theory fails. However, the phonon densities of states and the phonon dispersion are not physical quantities that result directly from MD. How to extract the vibrational information from the MD trajectories is the key to connecting MD simulations with the study of phonon dynamics.

In the work presented in this thesis, we used time-correlation method to study the lattice dynamics properties from MD simulation. Specifically, we adopted the so called "Fourier transformed velocity autocorrelation method" to connect the velocity trajectories with the vibrational energy spectra. The time-correlation method is one of the most active and fruitful areas of nonequilibrium statistical mechanics. It was initiated by Green and Kubo in 1950s [41,42], who showed that many transport processes and time-dependent phenomena could be written as integrals over a certain type of function called a time-correlation function. Similar to the role of partition functions in equilibrium statistical mechanics, these time-correlation functions play a role in determining physical quantities in nonequilibrium statistical mechanics. One great advantage of this approach is that the resulting formulas do not depend upon the details of any particular model. For example, it can be shown that any frequency dependent conductivity $\sigma(\omega)$ resulting from some

time-dependent current \vec{j} caused by an external field is given by

$$\sigma(\omega) = \frac{1}{kT} \int_0^{\infty} dt e^{-i\omega t} \langle \vec{j}(0) \vec{j}(t) \rangle \quad (3.19)$$

where T is temperature. $\langle \rangle$ is the ensemble average of the system. Note that this equation is so general that it even describes the self-diffusion process if a zero frequency limit is applied. Likewise, we will show in the next subsection that a velocity correlation function can give phonon spectra.

One possible problem here is the evaluation of the ensemble average, which is in practice very difficult. In principle, we have to average a large number of similar systems or trajectories with different initial conditions over some equilibrium ensemble. This problem can be tackled by the ergodic hypothesis, which states that for a stationary random process, a large number of observations made on N arbitrarily chosen systems at the same time from an ensemble of similar systems have the identical statistical properties as observing a single system at N arbitrary instants of time. Under this assumption, the ensemble average is equivalent to a time average, the latter of which is simpler to evaluate from time-evolving simulations, e.g., a MD simulation.

3.3.3.2 Fourier-Transformed Velocity Autocorrelation Method

We developed an autocorrelation method to transform the velocity trajectory to the vibrational energy space to study the phonon anharmonicity at various temperatures or pressures. The essence of this method is a stochastic signal sampling algorithm. We correlate the velocities of different atoms at different times and use a complete set of the harmonic functions to sample the energy space of the system, taking advantage of the orthogonality nature of harmonic vibrational eigenstates. The proof is not difficult. Here we show how a Fourier-transformed velocity autocorrelation leads to the vibrational DOS. Note that we generalize the question to the aperiodic system which has no \vec{q} dependence. In this sense, the phonon DOS of a periodic lattice is just a special case, and this method has already automatically

summed the \vec{q} part. As a result, similar methods are used to study the molecule or liquid systems [43,44]. More interestingly, it does not require any pre-defined model embedded here, such as a harmonic model in lattice dynamics. This "first principles" character benefits the study of the anharmonicity intrinsically. The vibrational DOS can be obtained by the Fourier transformed velocity autocorrelation method as follows:

$$g(\omega) = \frac{2}{k_B T} \sum_{j=1}^N \sum_{k=1}^3 m_j \lim_{\tau \rightarrow \infty} \frac{1}{2\tau} \int_{-\infty}^{\infty} dt' \int_{-\tau}^{\tau} dt v_j^k(t' + t) v_j^k(t')^* e^{-i\omega t} \quad (3.20)$$

where velocities can be written as the superposition of normal coordinates

$$v_j^k(t) = \frac{1}{m_j} \sum_s \dot{X}_s e_s^{jk} \quad (3.21)$$

Here X_s and e_s are normal coordinate and eigenvector of the s mode respectively, defined in Section 1.2. Note that we do not assume any periodicity in the system, therefore there is no normalization factor $1/\sqrt{N}$ or \vec{q} dependence. Combining Eq. 3.20 and Eq. 3.21 and using the orthogonality property of eigenvectors, i.e., $\sum_{j,k} e_s^{jk} e_{s'}^{jk} = \delta_{ss'}$, we can show that

$$g(\omega) = \frac{2}{k_B T} \sum_{s=1}^{3N} \frac{1}{4} \omega_s^2 A_s^2 (\delta(\omega - \omega_s) + \delta(\omega + \omega_s)) \quad (3.22)$$

where A_s is the amplitude of X_s . In the classical limit, $\frac{1}{4} A_s^2 \omega_s^2 = \frac{1}{2} k_B T$, and hence

$$g(\omega) = \sum_{s=1}^{3N} \delta(\omega - \omega_s) + \delta(\omega + \omega_s) \quad (3.23)$$

We can also recover the \vec{q} dependence in this process for a periodic system, i.e., project the DOS to a particular q point and obtain the phonon dispersion relation $\omega(\vec{q})$. The proof is more tedious, but the idea is clear: we account for the \vec{q} in the superposition of normal modes. Therefore, in addition to the time domain transformation for DOS, the spatial domain transformation is also performed si-

multaneously with the equilibrium lattice structures as the initial input. We can get a power spectrum $P(\vec{q}, \omega)$ which not only provides the dispersion relation, but also the power intensity distribution at any \vec{q} point. This method is versatile and powerful, and can be applied to many related fields. For example, similar method was used to study the thermal transport phenomena in solids [45].

Fig. 3.1 schematically illustrates how our velocity autocorrelation package works. The package takes in the time-dependent velocity data from a long time MD simulation, implemented with first-principles or classical MD packages, such as VASP or GULP. After the boundary correction and cell grouping, the velocity data are fed into the core of this package which calculates the autocorrelation function in parallel. It can then transform the autocorrelation function to the corresponding energy or momentum space and generate the DOS or phonon dispersion. The implementation of this code has little dependence on symmetry, atomic type, e.g., and hence is very robust. This is a signal processing code, and the accuracy is only determined by the quality of MD simulation. As expected, the frequency resolution Δf is inversely proportional to the simulation time T , and the resolution in \vec{q} space is inversely proportional to the size of the simulation box. As a result, the longer the MD simulation and the larger the simulated system, the better the quality of the output. For example, a 10 ps MD production roughly corresponds to a frequency resolution of 10 wavenumbers. Interesting applications and results from this method will be presented and discussed in the next few chapters.

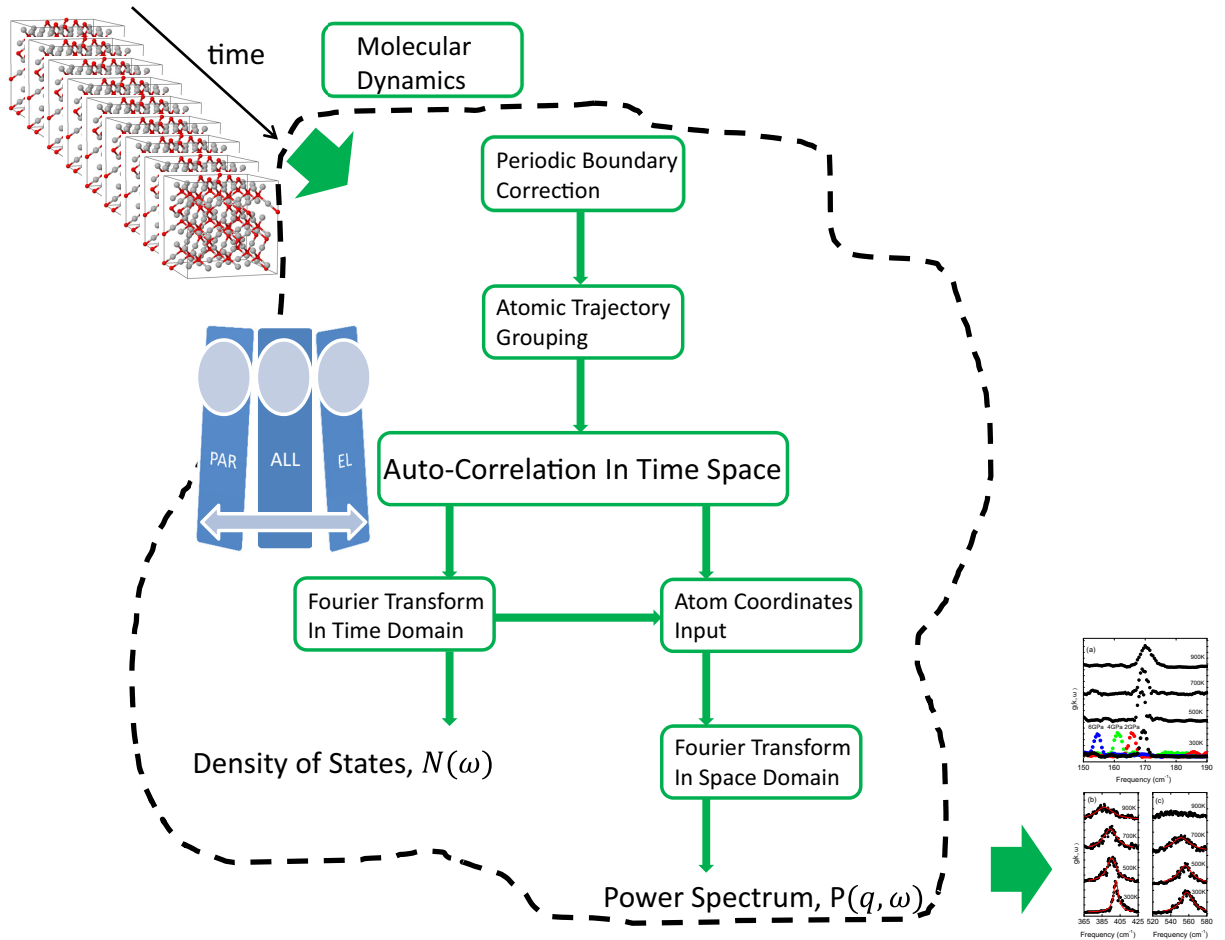


Figure 3.1: The flow chart implementing the Fourier-transformed velocity autocorrelation method

3.4 Anharmonic Fitting Algorithm

Based on the phonon-phonon interactions derived in Chapter 1, we developed a new method to fit the thermal broadenings and shifts of Raman and infrared peaks simultaneously with a full calculation for the kinematics of three-phonon and four-phonon processes. This fitting method correlates the thermal broadenings and shifts together, and provides rigorous procedures to identify the cubic and quartic components of the anharmonicity for each mode.

The main idea behind this method is the fact that the anharmonic coupling strength and the two-phonon kinematical processes are approximately separable if

the anharmonicity tensor does not vary significantly for different phonon processes. An analytical form of anharmonicity tensor was proposed by Ipatova [46], and more recently was found to be a good approximation by first principles calculations [47,48].

$$V(j; \vec{q}_1 j_1; \dots; \vec{q}_{s-1} j_{s-1}) = \frac{1}{2s!} \left(\frac{\hbar}{2N} \right)^{\frac{s}{2}} N \Delta(\vec{q}_1 + \dots + \vec{q}_{s-1}) \times [\omega_{j_0} \omega_1 \dots \omega_{s-1}]^{\frac{1}{2}} C(j; \vec{q}_1 j_1; \dots; \vec{q}_{s-1} j_{s-1}) \quad (3.24)$$

where $\Delta(\vec{q}_1 + \dots + \vec{q}_{s-1})$ enforces momentum conservation. We consider the term $C(j; \vec{q}_1 j_1; \dots; \vec{q}_{s-1} j_{s-1})$ to be a constant of the Raman mode j , and we use it as a fitting parameter. This approximation is not rigorous because $C(j; \vec{q}_1 j_1; \vec{q}_2 j_2)$ and $C(j; \vec{q}_1 j_1; -\vec{q}_1 j_1)$ change with j_1 and j_2 , but an average over modes, $\langle C(\cdot) \rangle = \sum_{1,2} C(j; \vec{q}_1 j_1; \vec{q}_2 j_2) / \sum_{1,2} 1$, is found by the fitting, where 1, 2 under the summation symbol represent $\vec{q}_i j_i$.

Central to this method is the calculation of the two-phonon DOS, $D(\Omega)$, defined as

$$D(\Omega) = \sum_{\vec{q}_1, j_1} \sum_{\vec{q}_2, j_2} D(\Omega, \omega_1, \omega_2) = \frac{1}{N} \sum_{\vec{q}_1, j_1} \sum_{\vec{q}_2, j_2} \Delta(\vec{q}_1 + \vec{q}_2) \left[(n_1 + n_2 + 1) \delta(\Omega - \omega_1 - \omega_2) + 2(n_1 - n_2) \delta(\Omega + \omega_1 - \omega_2) \right] \quad (3.25)$$

which counts the number of phonon-phonon interaction channels available to a phonon of frequency Ω . It depends on temperature through the phonon occupancy factors, n , and satisfies the kinematical conditions of conservation of energy and momentum. The first and second terms in square brackets in Eq. 6.5 are from down-conversion and up-conversion processes, respectively [47]. This spectral quantity can be calculated by scanning all phonon modes in Brillouin zone.

We will discuss this algorithm in detail, and present examples of analyzing the anharmonicity strengths of rutile and cuprite structures in the next few chapters.

Chapter 4

Phonon Anharmonicity of Rutile TiO₂

The main content of this chapter appeared in the journal article: Tian Lan, Xiaoli Tang and Brent Fultz, *Physical Review B* **85**, 094305 (2012).

Raman spectra of rutile titanium dioxide (TiO_2) were measured at temperatures from 100 K to 1150 K. Each Raman mode showed unique changes with temperature. Beyond the volume-dependent quasiharmonicity, the explicit anharmonicity was large. A new method was developed to fit the thermal broadenings and shifts of Raman peaks with a full calculation of the kinematics of 3-phonon and 4-phonon processes, allowing the cubic and quartic components of the anharmonicity to be identified for each Raman mode. A dominant role of phonon-phonon kinematics on phonon shifts and broadenings is reported. Force field molecular dynamics (MD) calculations with the Fourier-transformed velocity autocorrelation method were also used to perform a quantitative study of anharmonic effects, successfully accounting for the anomalous phonon anharmonicity of the B_{1g} mode.

4.1 Introduction

Rutile is the most common and stable crystal structure of titanium dioxide (TiO_2), and is important for both science and technology. Owing to its high refractive index and strong ultraviolet resistance, it is used extensively for pigments, optical coatings and sunscreens. In the past two decades, TiO_2 surfaces have been subjects of research as photocatalysts and high efficiency solar cells [49–53]. Many questions remain about point defects, vibrational dynamics, size effects and the recently-reported close relationship between surface and bulk properties [53–55]. A better understanding of the lattice dynamics of rutile will help answer many of them.

Rutile TiO_2 is tetragonal with the space group $P4/mnm$. It is stable to 1800 K [56]. The other two naturally-occurring phases of TiO_2 , anatase and brookite, are metastable and both convert to rutile upon heating. The 15 optical vibrational modes of rutile TiO_2 have the irreducible representation $1A_{1g} + 1A_{2g} + 1A_{2u} + 1B_{1g} + 1B_{2g} + 2B_{1u} + 1E_g + 3E_u$. The modes of symmetry B_{1g} , E_g , A_{1g} and B_{2g} are Raman active. The Raman active modes comprise motions of anions with respect to stationary central cations, either perpendicular to the c axis (modes B_{1g} , A_{1g} and B_{2g}), or along the c axis (mode E_g). The Raman spectrum of rutile was first recorded

by Narayanan [57], and peak assignments were made by Porto, *et al.* [58]. Raman spectrometry has been used in many studies of the lattice dynamics, phase transition and nanostructures of TiO_2 [59–64].

The present work on rutile TiO_2 focuses on anharmonicity, one of the most important but poorly understood characteristics of lattice dynamics at elevated temperatures. Anharmonic behavior affects crystal stability, heat capacity, optical properties and thermal transport. It causes shifts of phonon energies with temperature because larger thermal displacements emphasize components of the potential with higher powers of the displacement. Phonon broadening from decreased lifetimes is another anharmonic phenomenon, and an anharmonic model should be able to predict both the broadenings and shifts of the phonons with temperature. To date there have been few studies of anharmonicity of rutile TiO_2 . Perhaps the most complete experimental results are from Samara and Peercy's work in 1973 [59]. They reported frequency shifts of Raman modes with temperature and pressure, although the temperature range was below 500 K and no broadening information was reported. Their results show that the B_{1g} mode, which comprises rotatory motions of the four nearest neighbor oxygen anions around a central titanium atom (Fig. 4.1) is especially interesting. Its frequency changes little with temperature, but softens with pressure. Studies on other materials with the rutile structure, e.g., SnO_2 , MgF_2 and FeF_2 report similar behavior of the B_{1g} mode [65–68]. There are two conflicting views on the physical origin of these anomalies. One attributes it to an incipient structural phase transition [65,69,70], and the other attributes it to a thermal- or pressure-induced lattice contraction [66–68].

Lattice dynamics calculations based on density functional theory (DFT) were used to study the effect of pressure on phonons in rutile TiO_2 [70,71]. These calculations were for low temperature and in the quasiharmonic approximation, where phonons are assumed to be harmonic but their frequencies change with volume. Only a few studies have used molecular dynamics (MD) to calculate anharmonic frequency shifts and broadenings of phonon mode of materials [72,73], and to our knowledge, no such investigation has yet been performed on rutile TiO_2 .

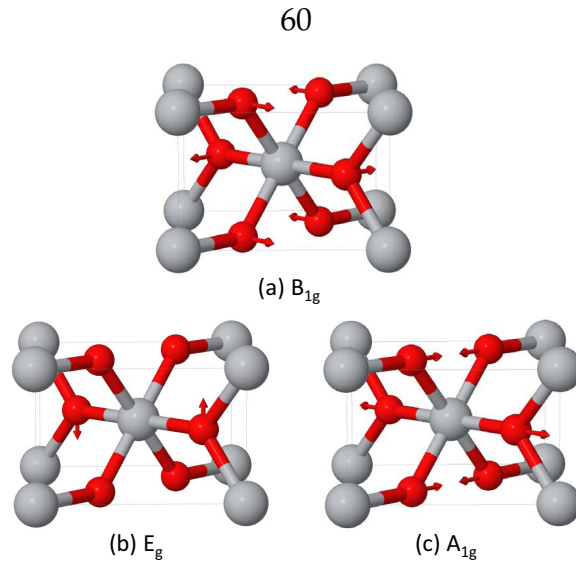


Figure 4.1: Rutile structure and oxygen atom displacements for Raman-active modes.

Here we report measurements of Raman spectra with high resolution at temperatures from 100 to 1150 K. Both phonon frequency shifts and broadenings were measured and analyzed. The quasiharmonic effects from thermal expansion were separated from anharmonic effects of phonon-phonon interactions by comparing temperature and pressure dependent trends of the Raman peaks. To identify the effects of cubic and quartic anharmonicity, we developed a new anharmonic analysis that allows data fitting with calculated two-phonon kinematic functionals. We also used force-field molecular dynamics (MD) calculations and Fourier-transformed velocity autocorrelation function methods to study the anharmonicity. The methods proved quite successful, and are able to account for the anomalous phonon softening of the B_{1g} mode.

4.2 Experiments

Samples were commercial TiO_2 powder (Alfa Aesar, Ward Hill, MA) with a rutile phase fraction of at least 99.9%. The sample powder was packed loosely inside a quartz sample cell in a furnace with several electrical resistance heating elements insulated by ceramic rods [74]. The heating assembly was supported by stainless

steel flanges and surrounded by heat shields made of niobium foil. The assembly was mounted in a quartz optical tube of 1 mm thickness, and evacuated with a turbomolecular pump. Both the interior and exterior of the tube were covered by aluminum foil for thermal radiation shielding. A temperature controller drove a 1 kW direct current power supply for heating power. For low temperature measurements, the sample cell was mounted on the copper cold finger of a liquid nitrogen filled cryostat and evacuated. Uniformity of sample temperature was confirmed by multiple ultrafine thermocouples mounted at different locations inside the sample cell, and the temperature resolution was ± 1 K. Samples were measured at temperatures from 100 to 1150 K, with intervals of 100 K below 700 K and 50 K above 700 K.

The Raman spectrometer used the 532 nm line from a solid state laser at power levels of 100 mW or less. A high efficiency longpass edge filter was used to block the laser line. The single pass spectrometer (Princeton Instruments Acton Series 500 mm) used a two-dimensional charge-coupled device camera with thermoelectric cooling (Princeton Instruments PIXIS 400B). The instrument resolution was 1.4 cm^{-1} . Each Raman spectrum was accumulated in 10 measurements with 1 s exposure times.

4.3 Molecular Dynamics Calculations

Our classical molecular dynamics (MD) calculations used simulation tools in the GULP software package [75]. Rutile TiO_2 , with its relatively small ionicity and large dipole moments on anions, is a challenging system for developing an interatomic potential. Few of those we tried [76–79] could simultaneously provide the crystal structure, elastic properties, thermal expansion and phonon vibrational frequencies. The best results for phonon properties were obtained with the Buckingham potential (Model 3) developed by Mostoller and Wang (MW shell model) [79]. The MW shell model was parameterized by fitting the phonon spectra over the whole Brillouin zone, and the model also gives reasonable bulk properties. We altered

slightly this model to improve its transferability and stability at different temperatures and pressures (the shell charge of titanium atoms was increased to 0.37 $|e|$). The parameters of the force field model were fixed for all the calculations presented below.

To extract anharmonic information on individual phonon modes from the atomic trajectories of the MD simulations, the phonon spectral energy density function $g(\vec{q}, \omega)$ was obtained by the velocity autocorrelation technique [43, 80]

$$g(\vec{q}, \omega) = \int dt e^{-i\omega t} \sum_{n,b} e^{i\vec{q}\cdot\vec{R}_n} \langle \vec{v}_{n,b}(t) \vec{v}_{0,0}(0) \rangle \quad (4.1)$$

where $\langle \rangle$ is an ensemble average, $\vec{v}_{n,b}(t)$ is the velocity of the atom b in the unit cell n at time t , \vec{R}_n is the equilibrium position of the cell n , and \vec{q} is the phonon wavevector. Equation 4.1 is both a time and space Fourier transform, and gives the frequency and lifetime of each phonon mode with a resolution determined by the size of the supercell used in the simulation.

Our MD simulations were performed with a $2 \times 2 \times 20$ supercell containing 960 atom cores and shells. We used the Verlet algorithm, an *NPT* ensemble, and a modified Nosé-Hoover thermostat for control of temperature and pressure. Both the isobaric temperature-dependent phonon peaks and the isothermal pressure-dependent phonon peaks were obtained in ranges of 300 K to 900 K and 0 GPa to 6 GPa. The run time for each set was 100 ps with time steps of 0.5 fs and sampling periods of 10 fs. The time-dependent atomic trajectories of velocity were post-processed by the velocity autocorrelation method to obtain mode frequencies and linewidths. The resolution of the wavevector \vec{q} along the Γ -Z direction was therefore $G_z/20$, where G_z is the magnitude of the reciprocal lattice vector. The frequency resolution was approximately 0.5 cm^{-1} .

4.4 Results

4.4.1 Experiment

After background subtraction, each peak in each spectrum was fitted to a Lorentzian function to obtain a centroid and full-width-at-half-maximum (FWHM). The FWHM data from the experiment were corrected for the finite resolution of the spectrometer [81]. Figure 4.3 presents these results of peak shifts and widths versus temperature. At room temperature, the Raman peak frequencies were 143 cm^{-1} , 447 cm^{-1} and 612 cm^{-1} , consistent with the well-accepted data from Porto, *et al.* [58]. We also find good agreement with the frequency shift data reported by Samara and Peercy [59] at temperatures below 480 K.

The E_g mode undergoes a large phonon softening with temperature. The A_{1g} mode has a small thermal softening at high temperature, but below 400 K the A_{1g} mode tends to stiffen slightly with temperature, as also reported by Samara and Peercy [59]. The B_{1g} mode appears to have no thermal shift. The thermal broadenings of E_g and A_{1g} peaks are large, but the B_{1g} mode shows far less broadening.

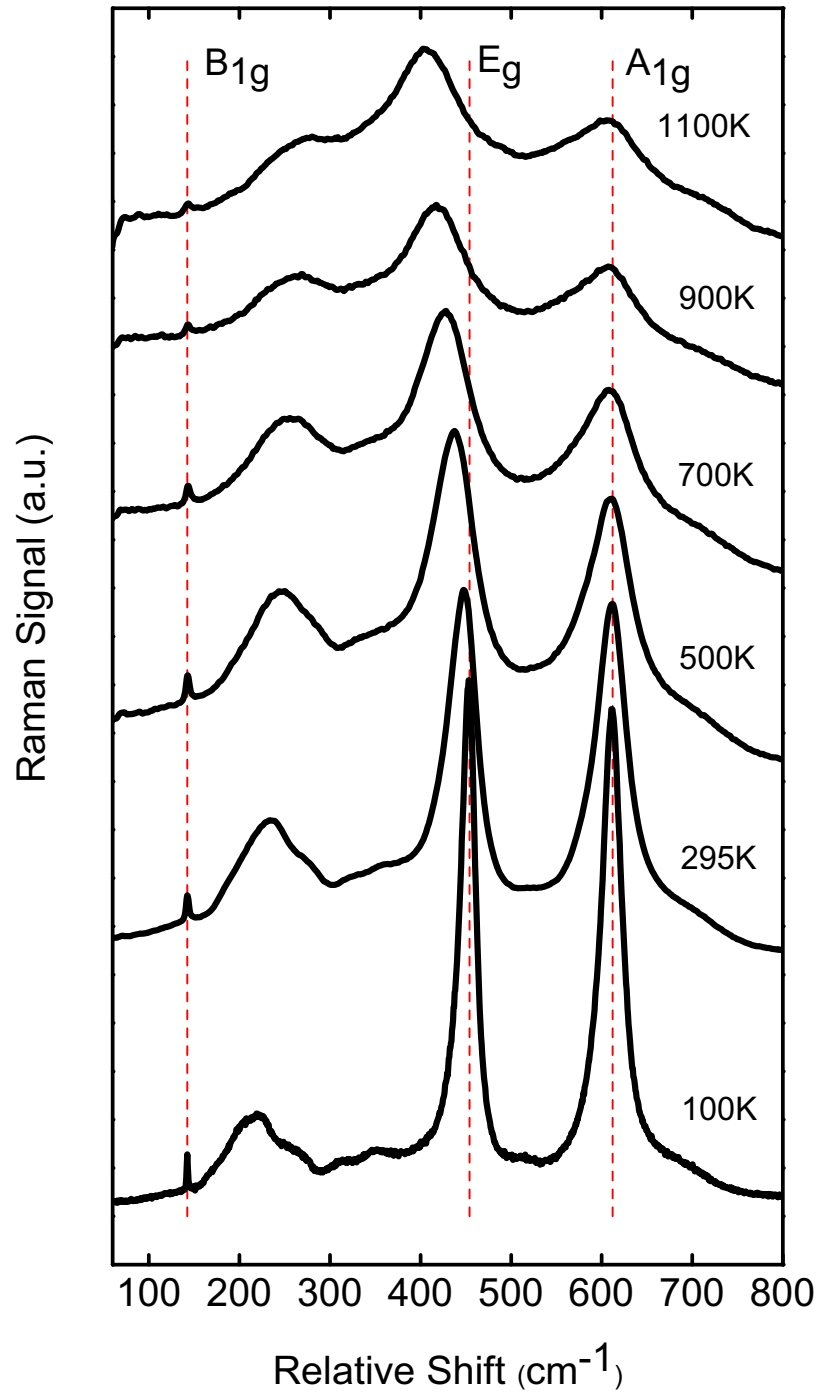


Figure 4.2: Raman spectra of rutile TiO₂ at selected temperatures from 100 K to 1150 K.

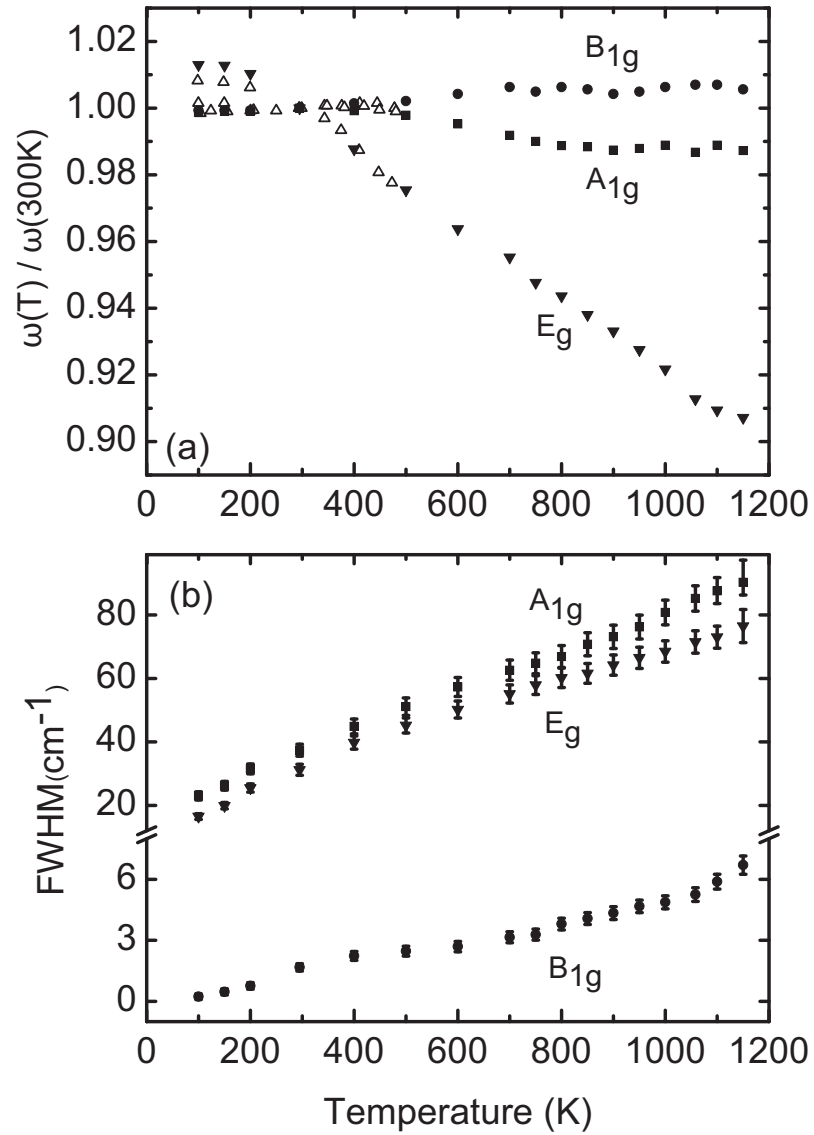


Figure 4.3: Temperature dependence of (a) frequency shifts, (b) FWHM, of the Raman modes B_{1g} , E_g and A_{1g} . Data of Ref. [[59]] are shown as open triangles in panel a.

4.4.2 MD Simulations

Table 4.1: Properties of rutile TiO₂ from present calculations, compared to experimental data. Units: lattice parameters in Å, Raman frequencies in cm⁻¹, thermal expansion coefficients in 10⁻⁶K⁻¹, volume compressibility in 10⁻³GPa⁻¹.

	Experiment	Calculation
Crystal Structure		
a	4.593	4.499
c	2.959	3.077
u	0.3048	0.3059
Raman Frequency		
B_{1g}	143	169
E_g	447	400
A_{1g}	612	558
B_{2g}	826	803
Thermal Expansion		
β_a	8.25	8.13
β_b	10.86	9.85
β_V	27.35	26.1
Compressibility		
κ	4.73	4.09

Table 6.1 presents results from our MD simulations and experimental data on lattice parameters, Raman frequencies, thermal expansion and volume compressibility. The calculated lattice parameters and Raman frequencies were from MD simulations at 300 K. The thermal expansion and compressibility were from isobaric (0 GPa) MD calculations to 900 K and isothermal (300 K) MD calculations to 6 GPa. The agreement with experimental data is good. The good agreement for the thermal expansion is encouraging for the use of the MD calculations for predicting

anharmonic behavior.

Figure 4.4a presents simulated Raman peaks of the B_{1g} mode at elevated temperatures at 0 GPa, and at elevated pressures at 300 K. The small thermal shift and broadening seen in the experimental results of Fig. 5.2 are apparent in the simulated results.

Figure 4.4b, c presents simulated Raman peaks of the E_g and A_{1g} modes at elevated temperature. The large thermal broadening of both modes, and the large thermal shift of the E_g mode are in apparent agreement with the experimental results of Fig. 5.2.

4.5 Experimental Data Analysis

4.5.1 Analysis of Quasiharmonicity and Anharmonicity

Both quasiharmonicity and explicit anharmonicity contribute to the non-harmonic lattice dynamics of rutile TiO_2 . In the quasiharmonic model, phonon modes behave harmonically with infinite lifetimes, but their frequencies are changed by the effects of volume on the interatomic potential. Explicit anharmonicity originates with phonon-phonon interactions, which increase with temperature. Explicit anharmonicity contributes to shifts in phonon frequencies, but also causes phonon damping and lifetime broadening of phonon peaks with temperature. The large peak broadenings and peculiar differences in shifts of the Raman peaks in rutile TiO_2 suggest there are important effects from explicit anharmonicity.

To separate the effects of quasiharmonicity and explicit anharmonicity, we treat the mode frequency $\omega_j = \omega_j(V, T)$ as a function of volume and temperature [59]

$$\left(\frac{\partial \ln \omega_j}{\partial T}\right)_P = -\frac{\beta}{\kappa} \left(\frac{\partial \ln \omega_j}{\partial P}\right)_T + \left(\frac{\partial \ln \omega_j}{\partial T}\right)_V \quad (4.2)$$

where j is the phonon mode index, β is the volume thermal expansivity and κ is the isothermal compressibility. The left-hand side gives the temperature-dependent

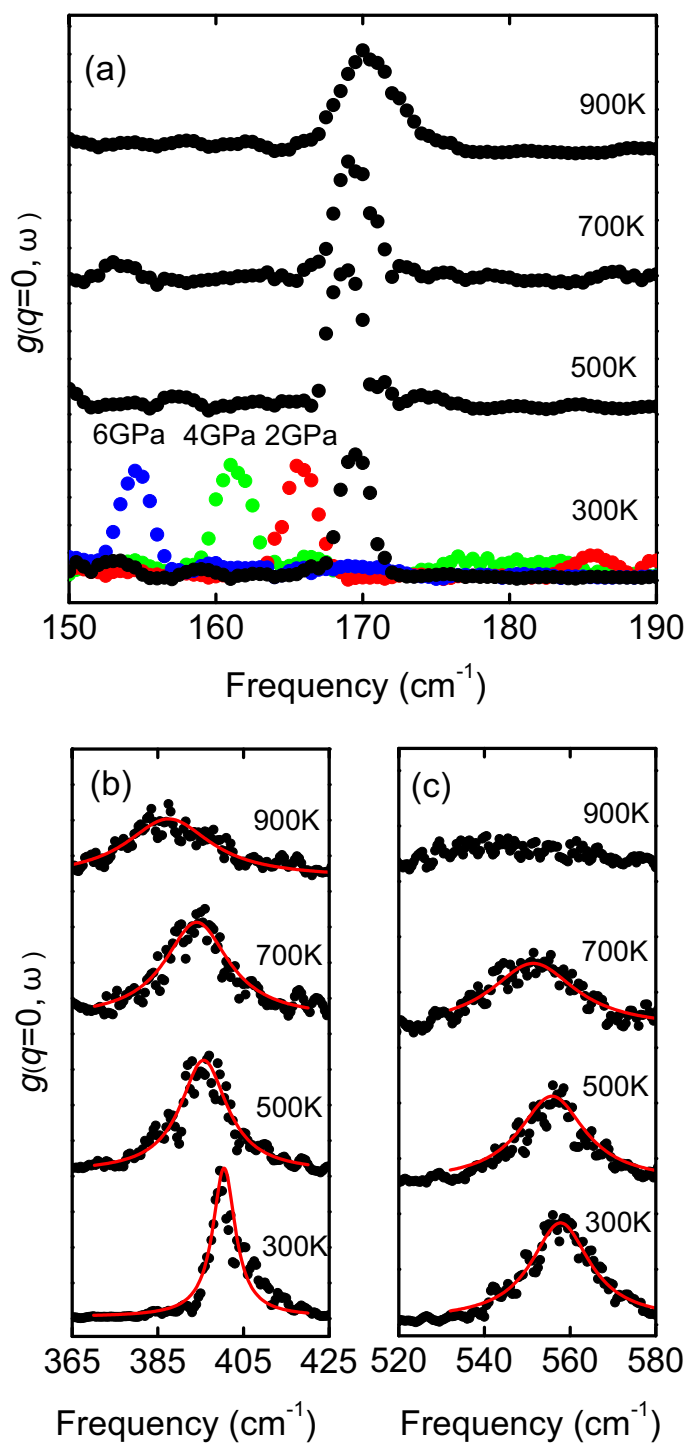


Figure 4.4: (a) The B_{1g} Raman peak calculated from the velocity trajectories of MD simulations, at temperatures as labeled and constant pressure of 0 GPa, and at pressures from 0 to 6 GPa at 300 K. (b) Calculated E_g Raman peak, and (c) Calculated A_{1g} Raman peak at temperatures as labeled and constant pressure of 0 GPa. Solid red curves are the Lorentzian fits.

isobaric frequency shift, including both quasiharmonic and explicit anharmonic behavior. The first term on the right-hand side, the isothermal frequency shift as a function of pressure, is the quasiharmonic contribution to the frequency shift. By defining a mode Grüneisen parameter as the proportionality of the relative change of the mode frequency to the relative change of volume, i.e., $\gamma_j = -\partial(\ln \omega_j)/(\partial(\ln V))$, this term can be written as $\gamma_j\beta$. The second term on the right of Eq. 6.7 is the pure temperature contribution to the frequency shift from the explicit anharmonicity. From the difference of the isobaric and isothermal frequency shifts, the explicit anharmonicity can be determined experimentally.

We used the mode Grüneisen parameters γ_j reported by Samara and Peercy [59] from Raman measurements under pressure. Since the γ_j are very weakly dependent on temperature [59,65], as is the thermal expansion above 300 K [82], the γ_j can be assumed to be constants for identifying the volume dependent quasiharmonic contribution. The results, summarized in Table 5.2, separate the frequency shifts from quasiharmonicity and explicit anharmonicity. Samara and Peercy's results at 296 K are also shown for comparison. For the B_{1g} mode, Table 5.2 shows that the quasiharmonic and explicit anharmonic contributions are both large but opposite in sign, and their near-perfect cancellation causes the B_{1g} mode to have a small thermal frequency shift to 1150 K. The quasiharmonic softening of the B_{1g} mode with increasing pressure (or equivalently, with decreasing temperature), and its negative Grüneisen parameter, are anomalous. The A_{1g} mode has a similar cancellation of quasiharmonic and explicit anharmonic contributions, but the signs of two contributions are reversed. The positive explicit anharmonic shift of the A_{1g} mode is unusual. We find this explicit anharmonicity at higher temperature to be smaller than Samara and Peercy's result below 400 K. There is a similar difference for the E_g mode but with an opposite trend, where the explicit anharmonic contribution increases by an order of magnitude when averaged over a larger range of temperature. It becomes comparable to the quasiharmonic contribution, hastening the softening of the E_g mode at temperatures above 400 K.

Table 4.2: Frequencies of the three Raman modes, their logarithmic pressure and temperature derivatives, and mode Grüneisen parameters. The measured isobaric temperature derivatives are separated into the pure volume and pure temperature contributions. Samara and Percy's results are listed in the lower row for each mode. And mode Grüneisen parameters are from Ref. [59]

Mode	ω (cm^{-1})	γ_j	$\left(\frac{\partial \ln \omega}{\partial T}\right)_P$ (10^{-5}K^{-1})	$= -\gamma_j \beta$ (10^{-5}K^{-1})	$+ \left(\frac{\partial \ln \omega}{\partial T}\right)_V$ (10^{-5}K^{-1})
B_{1g}	143	-5.03	0.788	11.82	-11.03
	143		0.6		-11.22
E_g	447	2.43	-11.17	-5.71	-5.46
	450		-6.3		-0.59
A_{1g}	612	1.59	-1.42	-3.72	2.3
	612		0.6		4.32

4.5.2 Analysis of Cubic and Quartic Anharmonicity

The previous section showed how the comparison of temperature-dependent and pressure-dependent shifts of phonon frequencies can be used to separate quasiharmonic and anharmonic behavior. The anharmonic behavior can be resolved further. When phonon anharmonicities are treated as perturbations that cause interactions of quasiharmonic phonons, it is known how the cubic anharmonicity associated with three-phonon processes and the quartic anharmonicity of four-phonon processes affect differently the shift and broadening of quasiharmonic phonons. The Feynman diagrams for the leading-order contributions to the phonon self-energy are [2]

$$\Sigma_j = \Sigma^{(3)} + \Sigma^{(3')} + \Sigma^{(4)}, \quad (3a)$$

$$\Sigma_j = \begin{array}{c} \begin{array}{c} \vec{q}_1 \\ \curvearrowright \\ \vec{q}_j \quad \vec{q}_j \\ \curvearrowleft \\ \vec{q}_2 \end{array} \\ + \begin{array}{c} \vec{q}_2 \\ \curvearrowright \\ \vec{q}_j \quad \vec{q}_j \\ \curvearrowleft \\ -\vec{q}_2 \end{array} \\ + \begin{array}{c} \vec{q}_1 \\ \curvearrowright \\ \vec{q}_j \quad \vec{q}_j \\ \curvearrowleft \\ -\vec{q}_1 \end{array} \end{array} . \quad (3b)$$

The lowest order contributions to the shifts, Δ , and broadenings, Γ , of the Raman mode j , are derived from the real and imaginary parts of the cubic and quartic self-energies $\Sigma^{(3)}$, $\Sigma^{(3')}$ and $\Sigma^{(4)}$

$$\begin{aligned} \Delta^{(3)}(j; \Omega) &= -\frac{18}{\hbar^2} \sum_{\vec{q}_1 j_1} \sum_{\vec{q}_2 j_2} |V(j; \vec{q}_1 j_1; \vec{q}_2 j_2)|^2 \\ &\times \wp \left[\frac{n_1 + n_2 + 1}{\Omega + \omega_1 + \omega_2} - \frac{n_1 + n_2 + 1}{\Omega - \omega_1 - \omega_2} \right. \\ &\quad \left. + \frac{n_1 - n_2}{\Omega - \omega_1 + \omega_2} - \frac{n_1 - n_2}{\Omega + \omega_1 - \omega_2} \right] \end{aligned} \quad (4.4a)$$

$$\begin{aligned} \Delta^{(3')}(j) &= -\frac{72}{\hbar^2} \sum_{j_1} \sum_{\vec{q}_2 j_2} V(j; j; \vec{0} j_1) V(\vec{0} j_1; -\vec{q}_2 j_2; \vec{q}_2 j_2) \\ &\times \wp \left(\frac{1}{\omega_1} \right) \left(n_2 + \frac{1}{2} \right) \end{aligned} \quad (4.4b)$$

$$\Delta^{(4)}(j) = \frac{24}{\hbar} \sum_{\vec{q}_1 j_1} V(j; j; \vec{q}_1 j_1; -\vec{q}_1 j_1) \left(n_1 + \frac{1}{2} \right) \quad (4.4c)$$

$$\begin{aligned} \Gamma^{(3)}(j; \Omega) &= \frac{18\pi}{\hbar^2} \sum_{\vec{q}_1 j_1} \sum_{\vec{q}_2 j_2} |V(j; \vec{q}_1 j_1; \vec{q}_2 j_2)|^2 \\ &\times \left[(n_1 + n_2 + 1) \delta(\Omega - \omega_1 - \omega_2) \right. \\ &\quad \left. + 2(n_1 - n_2) \delta(\Omega + \omega_1 - \omega_2) \right], \end{aligned} \quad (4.4d)$$

where Ω is the phonon frequency and \wp denotes the Cauchy principal part. The $V(\cdot)$'s are elements of the Fourier transformed anharmonic tensor, denoting the coupling strength between the Raman mode j to other modes $\{\vec{q}_i j_i\}$ having quasi-harmonic frequencies $\{\omega_i\}$ and occupancies $\{n_i\}$. The broadening of the Raman peaks is $2\Gamma^{(3)}(j; \Omega)$. The simplicity of the first-order shift $\Delta^{(4)}(j; \Omega)$ is partly a consequence of zero momentum transfer in Raman spectroscopy.

For crystals having atoms without inversion symmetry, as is the case for the rutile structure, an additional low-order cubic term $\Delta^{(3')}(j)$, expressed in Eq. 4.4b, is possible. It corresponds to the second diagram in Eq. 3 with instantaneous phonons at a three-phonon vertex [2]. Group theory further showed that the only nonzero contribution to Eq. 4.4b arises from the j_1 mode that belongs to the

identity representation [83]. Owing to the rigorous restrictions on the existence of instantaneous three-phonon processes, $\Delta^{(3)}$ is generally much smaller than $\Delta^{(3)}$. For rutile TiO_2 , this term needs to be evaluated only for the A_{1g} mode because it does not have inversion symmetry for oxygen atom motions (see Fig. 4.1c).

Including all shifts, the frequencies of the Raman peaks are

$$\omega_j(T, \Omega) = \omega_{j0} \exp\left[-\gamma_j \int_0^T \beta(T) dT\right] + \Delta^{(3)}(j; \Omega) + \Delta^{(3)}(j) + \Delta^{(4)}(j). \quad (4.5)$$

The first term on the right of Eq. 4.5 is the integral form of the quasiharmonic phonon shift (discussed after Eq. 6.7) and from the last term of Eq. 4.5, $(\partial\omega_j/\partial T)_V \delta T = \Delta^{(3)}(j; \Omega) + \Delta^{(3)}(j) + \Delta^{(4)}(j)$ is the explicit anharmonic shift. To obtain $\beta(T)$, experimental data from 4 K to 1200 K [59, 82] were fitted with a well-accepted analytical form [84]

$$\beta(T) = \left(\frac{A}{T} + \frac{B}{T^2}\right) \sinh^{-2}\left(\frac{T_1}{T}\right) \quad (4.6)$$

giving $A = 7.16 \times 10^{-5}$, $B = 0.524K$ and $T_1 = 146.2K$.

In what follows, we use Eqns. 4.4a - 4.4d, to identify the magnitudes and signs of the cubic and quartic anharmonicities from the thermal shifts and broadenings of the Raman modes in rutile TiO_2 . We do not calculate the $V(\cdot)$'s, which are complicated tensor quantities, but instead we treat them as parameters in fitting the experimental trends of the Raman modes. We do a full calculation of the two-phonon density of states, however, as described below.

From Ipatova, *et al.* [46], an anharmonic tensor element for a process with s phonons is

$$V(j; \vec{q}_1 j_1; \dots; \vec{q}_{s-1} j_{s-1}) = \frac{1}{2s!} \left(\frac{\hbar}{2N}\right)^{\frac{s}{2}} N \Delta(\vec{q}_1 + \dots + \vec{q}_{s-1}) \times [\omega_{j0} \omega_1 \dots \omega_{s-1}]^{\frac{1}{2}} C(j; \vec{q}_1 j_1; \dots; \vec{q}_{s-1} j_{s-1}) \quad (4.7)$$

where $\Delta(\vec{q}_1 + \dots + \vec{q}_{s-1})$ enforces momentum conservation. Ipatova, *et al.* [46],

suggest that the $C(\cdot)$'s are slowly-varying functions of their arguments. Several studies used this assumption to calculate or fit approximately the anharmonic broadening [46, 85, 86]. Klemens assumed the frequency independent part of the coupling tensor for a Raman mode j was a constant that depended on the strain field of the mode [87]. Likewise, we consider the term $C(j; \vec{q}_1 j_1; \dots; \vec{q}_{s-1} j_{s-1})$ to be a constant of the Raman mode j , and we use it as a fitting parameter. This approximation is not rigorous because $C(j; \vec{q}_1 j_1; \vec{q}_2 j_2)$ and $C(j; j; \vec{q}_1 j_1; -\vec{q}_1 j_1)$ change with j_1 and j_2 , but an average over modes, $\langle C(\cdot) \rangle = \sum_{1,2} C(j; \vec{q}_1 j_1; \vec{q}_2 j_2) / \sum_{1,2} 1$, is found by the fitting, where 1, 2 under the summation symbol represent $\vec{q}_i j_i$. We define the cubic and quartic fitting parameters as

$$C_j^{(3)} = \langle C(j; \vec{q}_1 j_1; \vec{q}_2 j_2) \rangle \quad (4.8a)$$

$$C_j^{(4)} = \langle C(j; j; \vec{q}_1 j_1; -\vec{q}_1 j_1) \rangle \quad (4.8b)$$

While the anharmonic tensor describes the coupling strength of phonon-phonon interactions, a prerequisite is that the phonons in these processes satisfy the kinematical conditions of conservation of energy and momentum (as explicitly written in Eqs. 4.4 and 6.2). Central to phonon linewidth broadening from the cubic anharmonicity, $2\Gamma^{(3)}$, is the two-phonon DOS, $D(\Omega)$, defined as

$$\begin{aligned} D(\Omega) &= \sum_{\vec{q}_1, j_1} \sum_{\vec{q}_2, j_2} D(\Omega, \omega_1, \omega_2) \\ &= \frac{1}{N} \sum_{\vec{q}_1, j_1} \sum_{\vec{q}_2, j_2} \Delta(\vec{q}_1 + \vec{q}_2) \left[(n_1 + n_2 + 1) \delta(\Omega - \omega_1 - \omega_2) \right. \\ &\quad \left. + 2(n_1 - n_2) \delta(\Omega + \omega_1 - \omega_2) \right] \end{aligned} \quad (4.9)$$

which depends on temperature through the phonon occupancy factors, n . The first and second terms in square brackets in Eq. 6.5 are from down-conversion and up-conversion processes, respectively [47]. The two-phonon kinematical functional

for the anharmonic frequency shifts from the cubic anharmonicity, $\Delta^{(3)}$, is $P(\Omega)$

$$\begin{aligned}
P(\Omega) &= \sum_{\vec{q}_1, j_1} \sum_{\vec{q}_2, j_2} P(\Omega, \omega_1, \omega_2) \\
&= \frac{1}{N} \sum_{\vec{q}_1, j_1} \sum_{\vec{q}_2, j_2} \Delta(\vec{q}_1 + \vec{q}_2) \wp \left[\frac{n_1 + n_2 + 1}{\Omega + \omega_1 + \omega_2} - \frac{n_1 + n_2 + 1}{\Omega - \omega_1 - \omega_2} \right. \\
&\quad \left. + \frac{n_1 - n_2}{\Omega - \omega_1 + \omega_2} - \frac{n_1 - n_2}{\Omega + \omega_1 - \omega_2} \right] \quad (4.10)
\end{aligned}$$

Both $D(\Omega)$ and $P(\Omega)$ were calculated at various temperatures for the phonon dispersions calculated with the MW shell model, sampling $\omega_{\vec{q}j}$ with a $16 \times 16 \times 16$ q -point grid, giving good convergence. Figure 4.5 shows representative results for $D(\Omega)$ and $P(\Omega)$. The down-conversion and up-conversion subspectra of $D(\Omega)$ are shown for 1000 K. The up-conversion processes are skewed to lower frequencies, and disappear above 800 cm^{-1} , consistent with the highest phonon frequency of rutile TiO_2 being about 800 cm^{-1} .

With Eqs. 6.2, 6.4, 4.9 and 5.2, the anharmonic frequency shifts and linewidth broadenings are rewritten as functions of $P(\Omega)$ and $D(\Omega)$, weighted by average anharmonic coupling strengths

$$\Delta^{(3)}(j; \Omega) = -\frac{\hbar}{64} \omega_{j0} |C_j^{(3)}|^2 \sum_{\vec{q}_1, j_1} \sum_{\vec{q}_2, j_2} \omega_1 \omega_2 P(\Omega, \omega_1, \omega_2) \quad (4.11a)$$

$$\Delta^{(3')} (j) = -\frac{\hbar}{16N} \omega_{j0} |C_j^{(3)}|^2 \sum_{\vec{q}_2, j_2} \omega_{j_2}(\vec{q}_2) \left(n_{\vec{q}_2, j_2} + \frac{1}{2} \right) \quad (4.11b)$$

$$\Delta^{(4)}(j) = \frac{\hbar}{8N} \omega_{j0} C_j^{(4)} \sum_{\vec{q}_1, j_1} \omega_{j_1}(\vec{q}_1) \left(n_{\vec{q}_1, j_1} + \frac{1}{2} \right) \quad (4.11c)$$

$$\Gamma^{(3)}(j; \Omega) = \frac{\pi \hbar}{64} \omega_{j0} |C_j^{(3)}|^2 \sum_{\vec{q}_1, j_1} \sum_{\vec{q}_2, j_2} \omega_1 \omega_2 D(\Omega, \omega_1, \omega_2) \quad (4.11d)$$

It is an approximation to use the same $|C_j^{(3)}|^2$ for $\Delta^{(3)}$ and $\Delta^{(3')}$, but $\Delta^{(3')}$ is expected to be small, and is nonzero for only the A_{1g} mode. Using Eq. 6.6 and Eq. 4.5, for each Raman mode both its frequency shift and its broadening were fitted simultaneously

with the two parameters, $|C_j^{(3)}|^2$ and $C_j^{(4)}$. The best fits for the shifts and broadenings are shown in Figs. 4.6, 4.7 and 4.8, and the fitting parameters are given in Table 5.3. Figure 4.6a, 4.7a and 4.8a also present contributions to the shift from the quasiharmonic and explicit anharmonicity as dashed curves.

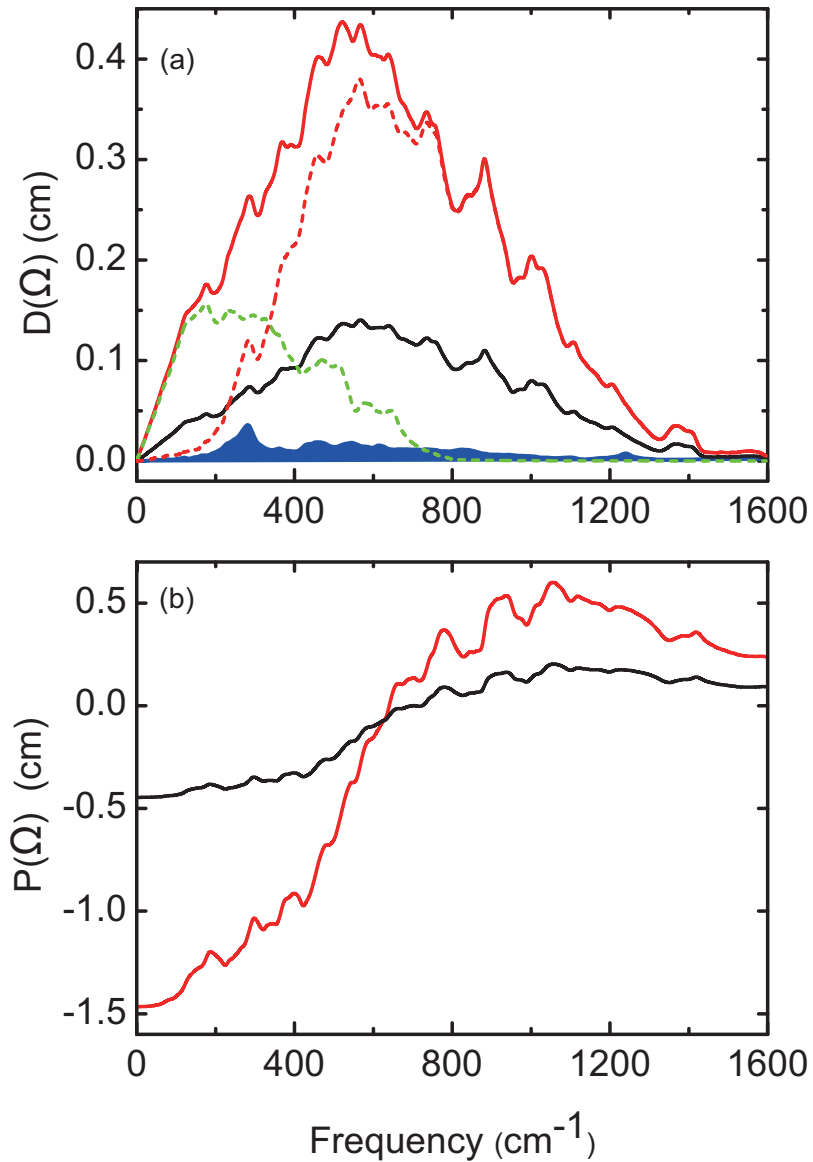


Figure 4.5: (a) Two-phonon density of states $D(\Omega)$ of Eq. 4.9 for 300 K (black) and 1000 K (red). The up-conversion and down-conversion contributions to $D(\Omega)$ at 1000 K are shown in green dash and red dash curves, respectively. The overtone process at 1000 K is highlighted as the filled area under the blue curve. (b) $P(\Omega)$ of Eq. 5.2 at 300 K (black) and 1000 K (red).

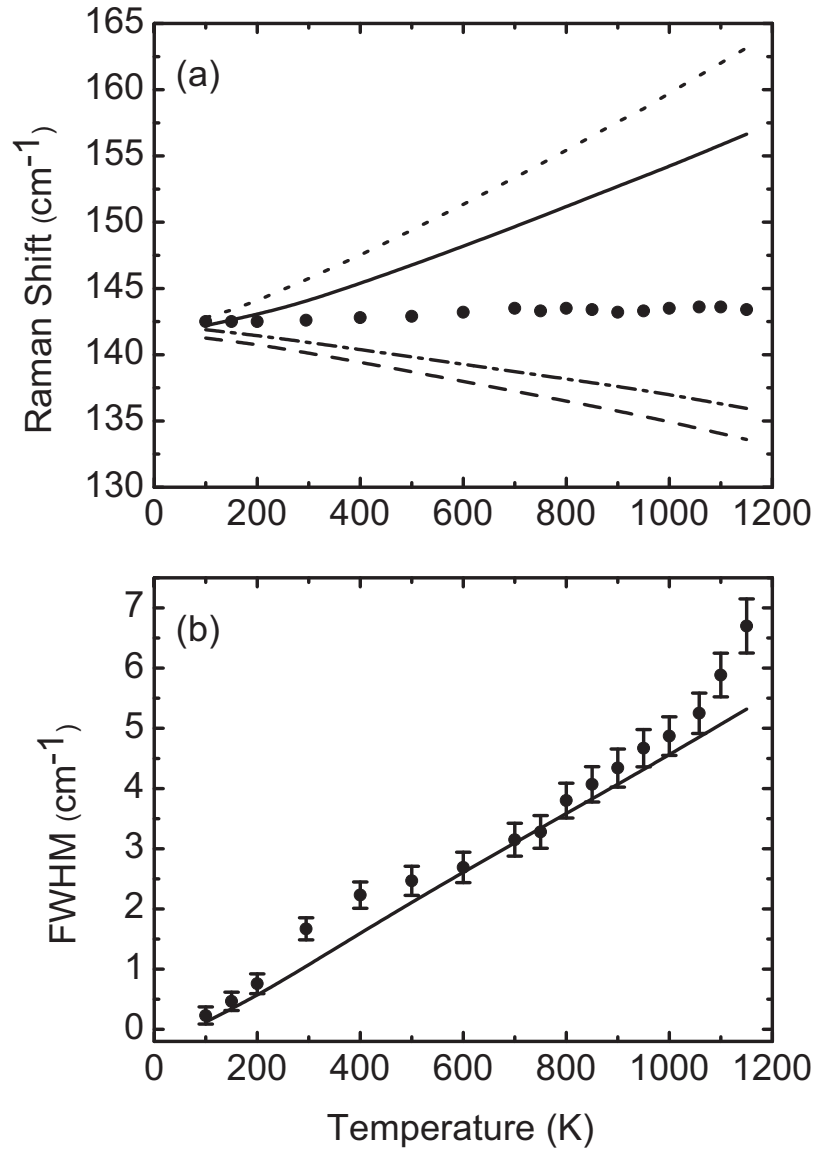


Figure 4.6: Temperature dependence of parameters for fittings to Raman peaks of mode B_{1g} (a) frequency shift, and (b) FWHM. Solid circles are experimental data. Solid curves are the fittings of the experimental points to Eq. 4.5 and Eq. 4.11d. Dotted line is the quasi-harmonic contribution to the frequency shift. Dash-dot line is the explicit anharmonicity $\omega_0 + \Delta^{(4)} + \Delta^{(3)}$, and dashed line is $\omega_0 + \Delta^{(3)}$.

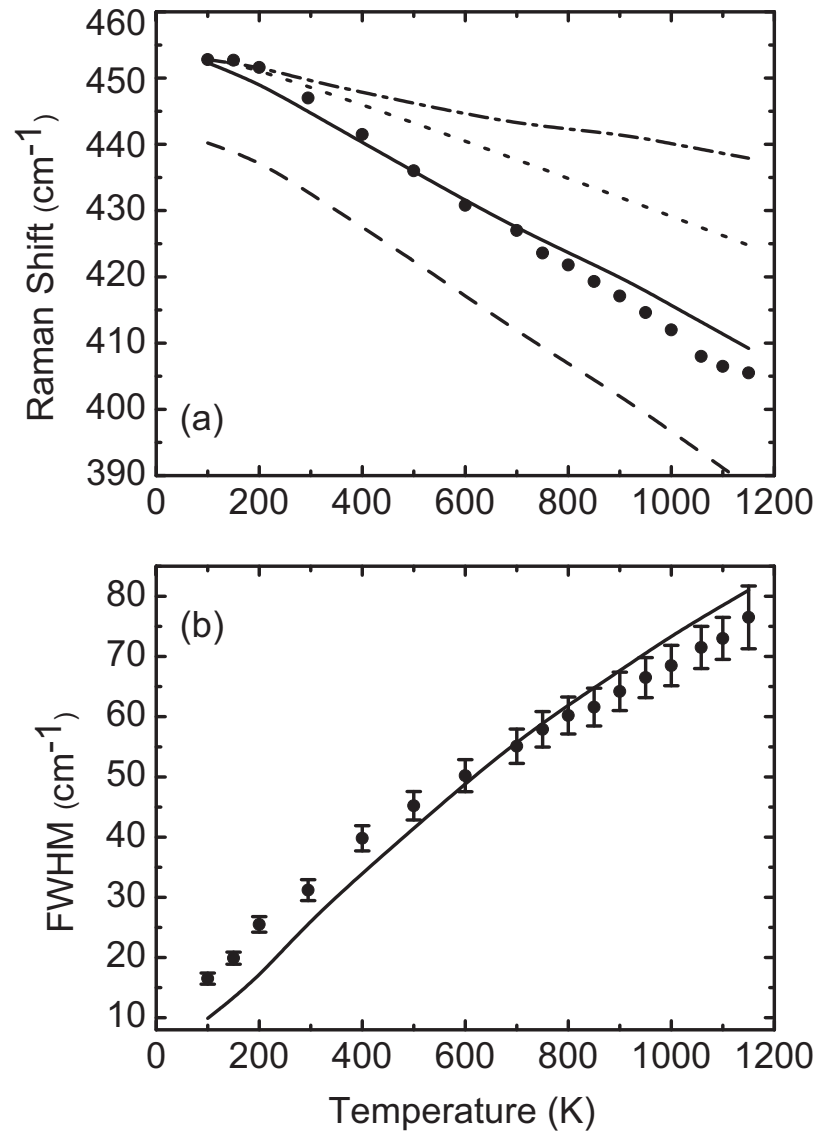


Figure 4.7: Temperature dependence of parameters for fittings to Raman peaks of mode E_g (a) frequency shift, and (b) FWHM. Dotted line is the quasi-harmonic contribution to the frequency shifts. Dash-dot line is the explicit anharmonicity $\omega_0 + \Delta^{(4)} + \Delta^{(3)}$ and dashed line is $\omega_0 + \Delta^{(3)}$.

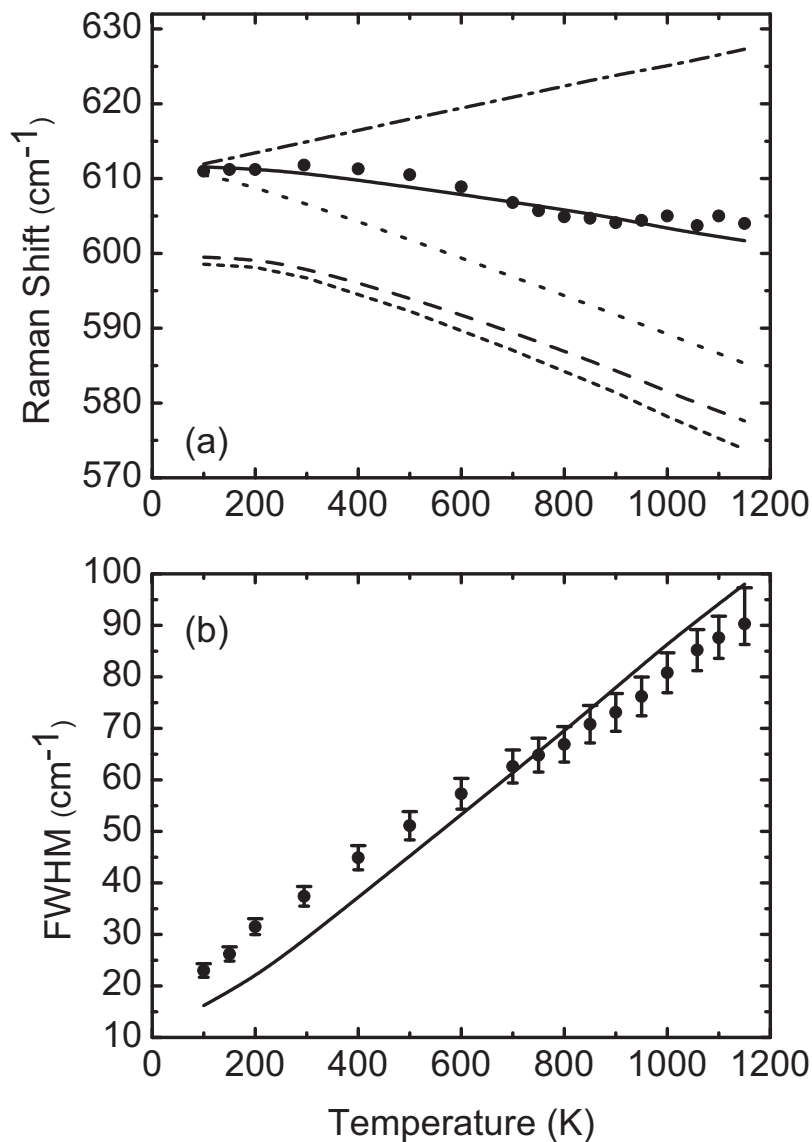


Figure 4.8: Temperature dependence of parameters for fittings to Raman peaks of mode A_{1g} (a) frequency shift, and (b)FWHM. Dotted line represents the quasi-harmonic contribution to the frequency shifts. Dash-dot line is the explicit anharmonicity $\omega_0 + \Delta^{(4)} + \Delta^{(3)} + \Delta^{(3')}$, short dash line corresponds to $\omega_0 + \Delta^{(3)} + \Delta^{(3')}$ and dashed line is $\omega_0 + \Delta^{(3)}$.

4.6 Discussion

4.6.1 Anharmonicities from Experimental Trends

Two factors determine the explicit anharmonicity – the anharmonic coupling strength described by the coupling tensor, and the two-phonon kinematical processes described by $D(\Omega)$ and $P(\Omega)$. The two are approximately separable if the anharmonicity tensor does not vary significantly for different phonon processes, and some features of the fits of Figs. 4.6, 4.7 and 4.8 suggest this is approximately true. Figure 4.5 shows that $D(\Omega)$ has a peak at the frequency $\Omega_0 = 600 \text{ cm}^{-1}$. The cubic anharmonicity and hence the broadening of the mode E_g and especially A_{1g} are large because they are near this peak in $D(\Omega)$. On the other hand, the B_{1g} mode can have only a small cubic anharmonicity because its frequency is far from Ω_0 . For the E_g and A_{1g} modes good fittings to the broadenings are obtained, indicating the dominance of cubic anharmonicity. The unusual concave downwards curvature of broadening of E_g in Fig. 4.3b is caused by the large frequency shift of this mode with temperature, which rapidly moves the E_g mode away from Ω_0 , and down the steep slope of $D(\Omega)$ in Fig. 4.5. This causes the broadening of the E_g mode to have a trend with temperature that is less than linear.

Starting with the same cubic fitting parameters used for the broadenings, the frequency shifts of the E_g and A_{1g} modes are fit well by adding the quasi-harmonic and quartic anharmonic effects. As illustrated in Fig. 4.7 and Fig. 4.8, the quartic contribution $\Delta^{(4)}$ is of the same order as the cubic one $\Delta^{(3)}$, consistent with the fact that $\Delta^{(4)}$ and $\Delta^{(3)}$ are both the leading order terms for the anharmonic frequency shifts. They are opposite in sign, however, because $\Delta^{(3)}$ enters with a negative sign

Table 4.3: Fitting parameters for the temperature dependent Raman modes (unit: 10^{11} erg^{-1})

	B_{1g}	E_g	A_{1g}
$ C^{(3)} ^2$	0.21	0.63	0.34
$C^{(4)}$	0.45	3.0	2.4

times the square of the cubic coupling tensor. The net anharmonic shift is usually negative, as for the E_g mode. For the A_{1g} mode, the additional contribution from the instantaneous three-phonon processes, $\Delta^{(3)}$ is also considered, but owing to a symmetry restriction, this term is small. The A_{1g} mode is unusual, having a net anharmonic shift that is positive, indicating the quartic contribution to the shift is larger than the cubic. Figure 4.5 shows that, at the frequency of mode A_{1g} , $P(\Omega)$ is close to zero. The cubic anharmonic shift $\Delta^{(3)}$ is therefore attenuated for the A_{1g} mode.

For the B_{1g} mode, Fig. 4.6a shows that the fitting deviates substantially from the experimental data. The discrepancies may originate with anharmonic contributions beyond the leading terms we considered. The rapid increase of the linewidth of the B_{1g} mode above the Debye temperature (≈ 780 K for rutile TiO_2) further supports this argument (a T^2 dependence is typical of broadening from higher-order quartic anharmonicity [46]).

The ratio of cubic to quartic anharmonicity is sometimes evaluated by fitting Raman spectra to a simplified Klemens model, in which the shifts and broadenings from phonon-phonon interactions (Eq. 4.4) include only overtone processes (one optical phonon at the Γ point decays into two or three phonons of equal energy on the same branch) [88]. In this simplified model, the temperature dependence of the Raman peak linewidth is

$$\begin{aligned} \Gamma_j(T) = & \Gamma_j(0) + A \left(1 + \frac{2}{e^{\hbar\omega_{j0}/2k_B T} - 1} \right) \\ & + B \left(1 + \frac{3}{e^{\hbar\omega_{j0}/3k_B T} - 1} + \frac{3}{(e^{\hbar\omega_{j0}/3k_B T} - 1)^2} \right) \end{aligned} \quad (4.12)$$

where $\Gamma_j(0)$ is the FWHM extrapolated to 0 K, and A and B are fitting parameters for three-phonon and four-phonon processes, respectively. A similar expression is used to fit the frequency shift, with fitting parameters C , D replacing A , B , and the quasi-harmonic frequency shift replacing $\Gamma_j(0)$ in Eq. 4.12. This approach often gives good fits to experimental Raman data, but the results can be misleading owing to the oversimplified approximations. In performing such fits for our data

on rutile TiO_2 , we found a cubic anharmonicity for the B_{1g} mode that was large compared to the quartic, which we know to be incorrect. This approach also gave a negative fitting parameter B for the quartic anharmonicity to explain the concave curvature of the thermal broadening of the E_g mode, which is unreasonable. The independent fits to thermal trends of linewidth and frequency shift (using Eq. 4.12 and its equivalent) offer no correlation between these quantities, even though they share a dependence on the same cubic anharmonic coupling tensor. Furthermore, it has been shown that the contributions from overtone processes are usually very small [81], as is shown by the lowest curve in Fig. 4.5(a) for rutile TiO_2 .

4.6.2 Anharmonicities from MD Simulations

Figure 4.9 shows the effects of temperature on the frequency shifts and broadenings of the B_{1g} mode, obtained from MD results such as those of Fig. 4.4a. Also shown is the effect of pressure on the frequency shift of the B_{1g} mode. These results are in excellent agreement with the experimental data.

From Fig. 4.9c, the Grüneisen parameter of the B_{1g} mode is found to be -4.23 , which compares well to the experimental value of -5.03 reported by Samara and Peercy [59].

To further study the anomalous anharmonicity of the B_{1g} mode, the frozen phonon method was used with the force field of MW shell model, allowing us to obtain the effective potential energy curve of the B_{1g} mode at different temperatures and pressures, as shown in Fig. 4.10. Three sets of lattice parameters were used, obtained from MD calculations at 300 K and 0 GPa, 300K and 6 GPa, 800 K and 0 GPa. These correspond to the volume at ambient conditions, a volume contraction of about 2.4%, and a volume expansion by about 1.3%, respectively. The quadratic potential dominates, and there is no cubic anharmonic contribution, as expected from symmetry. The quartic anharmonic potential is significant, however.

Figure 4.10 shows that the harmonic part of the B_{1g} potential has a curvature that increases with volume, contrary to the usual trend. This anomalous quasi-harmonic

response to volume reduces the force constant with increasing pressure, giving an anomalous mode softening. This phenomenon can be explained by the transverse motion of oxygen anion in the B_{1g} mode, perpendicular to the Ti-O bond. This transverse motion makes the mean interatomic distance $\langle R \rangle = |\langle \vec{r}_O - \vec{r}_{Ti} \rangle|$ greater than the distance between the mean atomic positions $R_0 = |\langle \vec{r}_O \rangle - \langle \vec{r}_{Ti} \rangle|$. An increase in volume increases the tension in the bond, tending to bring $\langle R \rangle$ closer to R_0 . The restoring force for transverse motion is thus increased, and the mode is stiffened [89]. For most materials this tension effect is hardly seen because the stretching along the bond direction is usually dominant, and bond stretching weakens the force constant. Rutile TiO_2 is special owing to its open structure, which reduces the coordination of atoms around the oxygen, allowing it large transverse amplitudes. Moreover, the Ti-O bonds are strong (vibrational modes along this bond direction, such as mode B_{2g} , are at the highest frequencies). The rigidity of the Ti-O bond suppresses bond stretching for the B_{1g} mode. A similar mechanism was used to explain the negative thermal expansion in polyethylene and Cu_2O [90, 91]. The temperature dependence of the B_{1g} mode is also anomalous – for both experiment and MD calculations, thermal expansion does not stiffen or soften the mode. As discussed following Eq. (6.7), this results from a quartic anharmonicity that increases with temperature, cancelling the stiffening trend from quasiharmonicity.

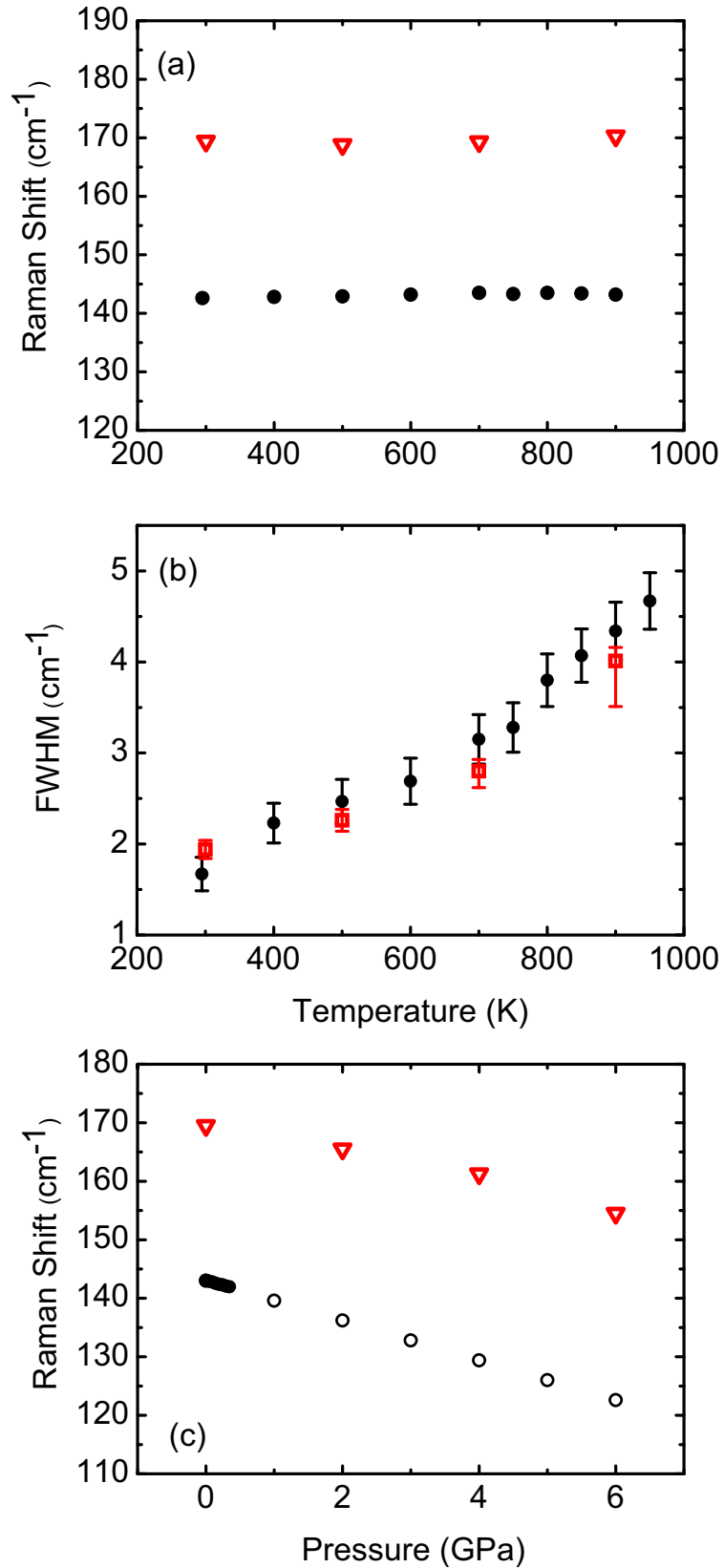


Figure 4.9: (a) Temperature dependent frequency shift, (b) FWHM broadening, and (c) pressure dependent frequency shift, of the B_{1g} mode from MD calculations (red), compared with experiment data (black).

The success of the MD calculations at elevated temperature and pressure shows that a shell model with a Buckingham potential can reproduce both the anomalous quasiharmonicity and the explicit anharmonicity of the B_{1g} mode of rutile TiO_2 , giving a detailed picture than can be compared to results from uniaxial-stress experiments [92], zero-pressure extrapolations of phonon frequencies [67, 68], and DFT calculations within the quasiharmonic approximation [70]. No orthorhombic or other distortion was found for our supercell at any temperature or pressure. The anomalous anharmonic behavior of the B_{1g} mode can be explained by volume effects on quasiharmonic force constants, and by the quartic anharmonicity. We need not invoke an incipient phase transition to the orthorhombic structure to explain this anharmonic behavior.

For the E_g and A_{1g} modes, the force field of the MW shell model qualitatively accounts for the large anharmonicity. As shown in Fig. 4.11 and Fig. 4.12, we obtain the trends of the large linewidth broadenings and the thermal softening of the E_g mode, but the MD calculations significantly underestimate the amount. The E_g and A_{1g} modes are more anharmonic than predicted by the MW shell model.

For each Raman mode, Fig. 4.13 compares the anharmonic potential to the harmonic potential, both obtained from the frozen phonon method with the MW shell model. The B_{1g} mode shows a large quartic potential. The A_{1g} mode is dominated by cubic anharmonicity. (A cubic contribution is not allowed by symmetry for the B_{1g} and E_g modes.) Since the MW shell model significantly underestimates the anharmonicity of the A_{1g} mode, the actual cubic potential energy could be larger. Evidently the frozen phonon potential cannot itself explain the large anharmonic effects, especially for the E_g mode, due to the fact that the frozen phonon potential does not account for phonon-phonon interactions. The large anharmonic effects of the E_g mode may originate from the many couplings between anharmonic phonons.

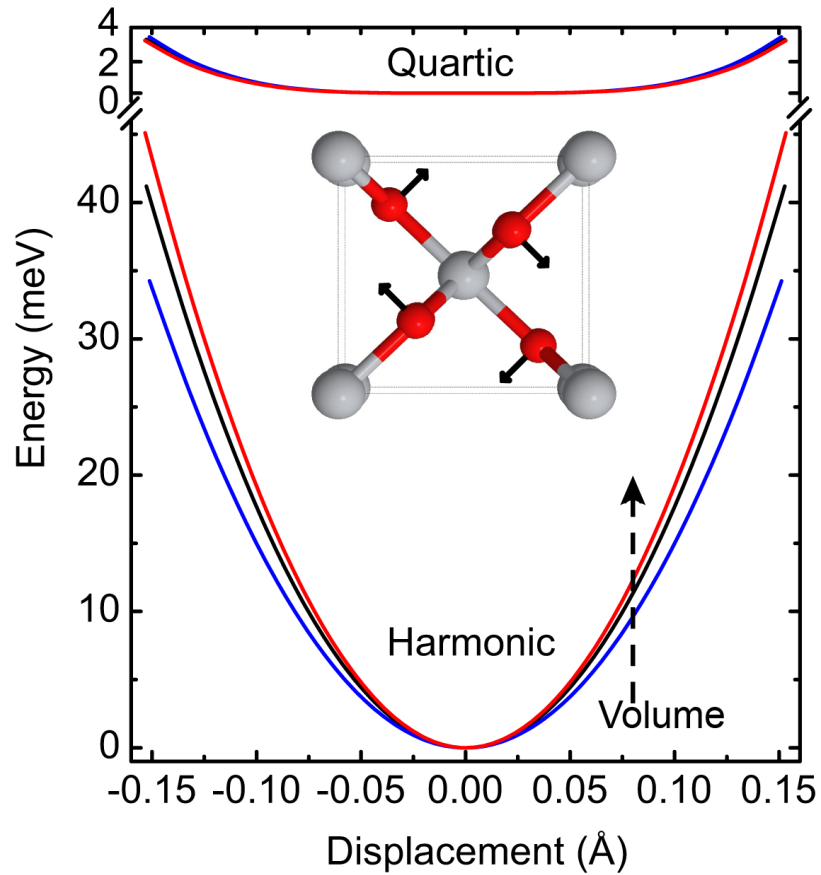


Figure 4.10: Frozen phonon potential of the B_{1g} mode calculated with the MW shell model, and its response to the volume increase (indicated as the dash arrow). The potential is decomposed into the harmonic component and quartic component. The three potentials are for lattice parameters corresponding to 300 K at 0 GPa (black), 300 K at 6 GPa (blue), and 800 K at 0 GPa (red). The inset shows the B_{1g} mode of rutile TiO_2 structure projected along the c-axis. Small arrows indicate the polarization vectors of this mode.

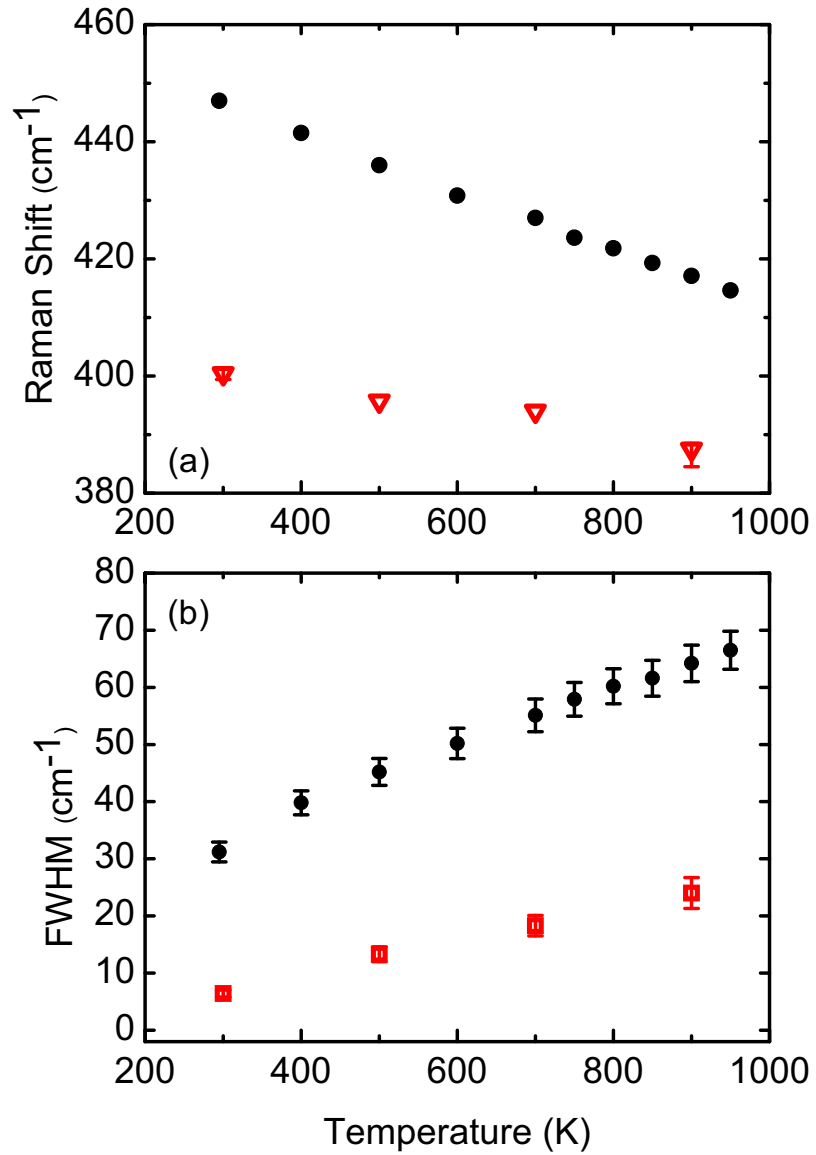


Figure 4.11: Temperature dependence of the (a) frequency shift, and (b) FWHM broadening, of the E_g mode from MD simulations (red) and experimental data (black).

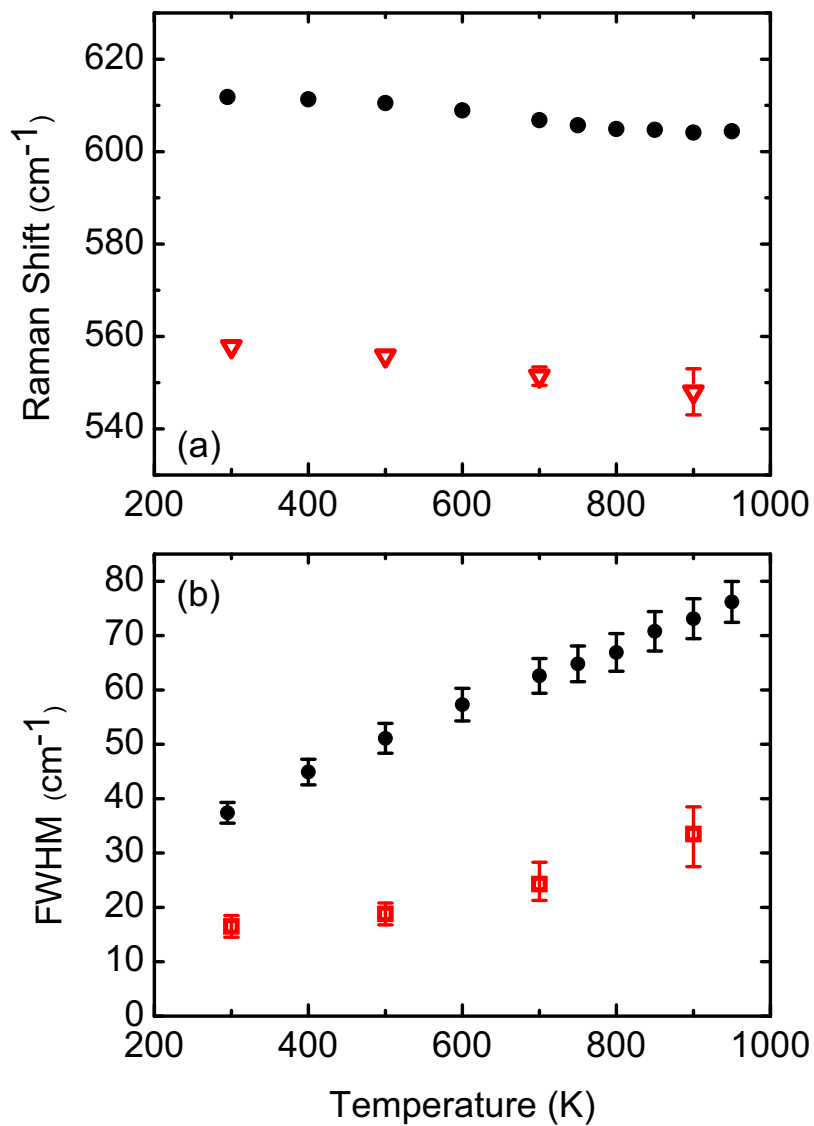


Figure 4.12: Temperature dependence of the (a) frequency shift, and (b) FWHM broadening, of the A_{1g} mode from MD simulations (red) and experimental data (black).

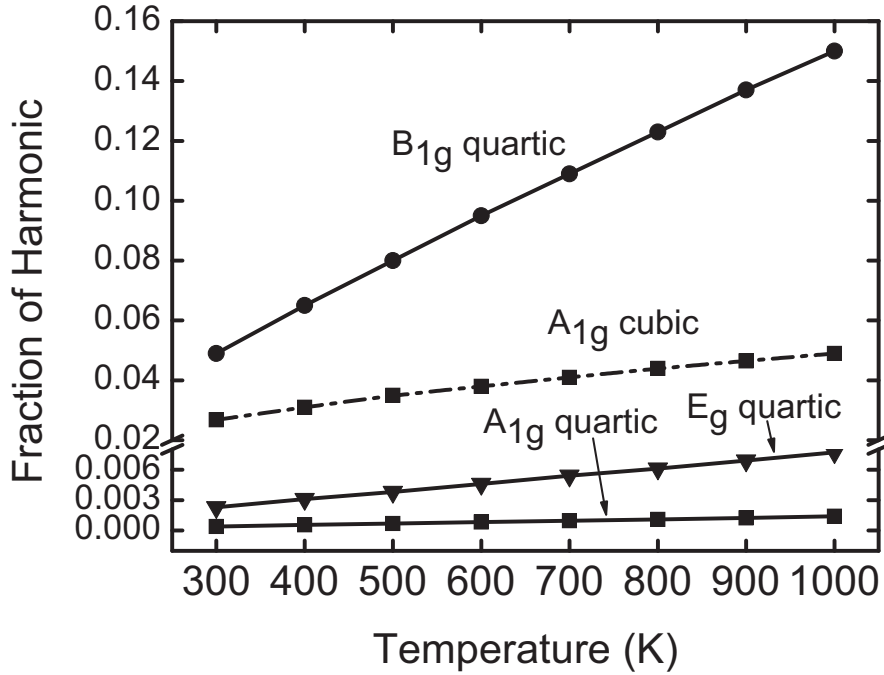


Figure 4.13: Ratio of the mode anharmonic potential and harmonic potential, with increasing temperature.

4.6.3 Vibrational Entropy of Rutile TiO₂

Vibrational entropy is important for thermophysical properties of materials, and for the thermodynamic stabilities of different solid phases as reviewed recently [93].

The vibrational entropy S_{vib} is

$$S_{\text{vib}} = 3k_{\text{B}} \int_0^{\infty} g(\epsilon) \left[(n(\epsilon) + 1) \ln(n(\epsilon) + 1) - n(\epsilon) \ln(n(\epsilon)) \right] d\epsilon \quad (4.13)$$

where $g(\epsilon)$ is the single phonon DOS at the temperature of interest, and $n(\epsilon)$ is the phonon occupancy. Although Eq. 4.13 is derived from the harmonic model, it is known to be valid for anharmonic systems to first order in perturbation theory [94]. From the phonon DOS obtained by MD simulations at elevated temperatures, S_{vib} was calculated with Eq. 4.13 and the results are presented in Table 4.4. The calculated results are in general agreement with the experimental data, but the dis-

crepancies suggest that the average phonon frequencies from the MD calculations are about 3.7% too small.

Table 4.4: Entropy in J/(mol K) of rutile TiO₂ from MD calculations and experimental data of Ref. [95].

T [K]	MD	Experimental
300	48.01	50.69
500	80.28	82.21
700	101.79	105.51
900	119.22	123.65

4.7 Conclusions

Raman spectra were measured on rutile TiO₂ at temperatures to 1150 K, and giant anharmonic behaviors were found for the shifts and broadenings of the three measurable Raman peaks. The pressure-dependence and temperature-dependence of the Raman peak shifts were used to separate the anharmonic behavior from the quasiharmonic behavior. Individual assessments of the cubic and quartic contributions to the anharmonicity were performed with a new data fitting method based on the kinematics of 3-phonon and 4-phonon processes, with the phonons calculated from a shell model in this case. In fitting the anharmonic behavior, mode broadening is from effects of cubic anharmonicity, while the anharmonic shifts are from the same cubic factor plus a quartic anharmonicity. The quartic anharmonicity of the B_{1g} mode was found to be large, and its cubic anharmonicity small, unlike the large cubic anharmonicity found for the E_g and A_{1g} modes. From successes of the fitting method, we suggest that the observed anharmonic effects are dominated by considerations of the kinematics of energy and momentum conservation in the phonon-phonon scattering processes, and less by the details of the anharmonicity tensor.

Force field molecular dynamics (MD) calculations were performed with the

same shell model. Both the anomalous quasiharmonic behavior and the explicit anharmonic behavior of the B_{1g} mode from our calculations were in excellent agreement with the experimental observation. No orthorhombic distortion was found, suggesting that the anomalous anharmonicity originates with the phonon responses to temperature and pressure, and not an incipient phase transition. Discrepancies for the E_g and A_{1g} modes suggest that the shell model potential may not be sufficient for obtaining accurate anharmonicities from molecular dynamics calculations, however.

Chapter 5

Phonon Anharmonicity of Rutile SnO₂

The main content of this chapter appeared in the journal article: Tian Lan, Chen W. Li and Brent Fultz, *Physical Review B* **86**, 134302 (2012).

Raman spectra of rutile tin dioxide (SnO_2) were measured at temperatures from 83 to 873 K. The pure anharmonicity from phonon-phonon interactions was found to be large and comparable to the quasiharmonicity. First principles calculations of phonon dispersions were used to assess the kinematics of 3-phonon and 4-phonon processes. These kinematics were used to generate Raman peak widths and shifts, which were fit to measured data to obtain the cubic and quartic components of the anharmonicity for each Raman mode. The B_{2g} mode had a large quartic component, consistent with the symmetry of its atom displacements. The broadening of the B_{2g} mode with temperature showed an unusual concave downwards curvature. This curvature is caused by a change with temperature in the number of down-conversion decay channels, originating with the wide band gap in the phonon dispersions.

5.1 Introduction

Rutile tin dioxide (SnO_2) is the most common and stable oxide of tin found in nature. Owing to the wide variety of its applications for optoelectronics, heterogeneous catalysis and gas sensors, rutile SnO_2 has been the subject of much recent research. [96] Lattice dynamics, phase transitions, and nanostructures of SnO_2 have been studied by measurements of optical phonons with Raman, Brillouin or infrared spectroscopy, [65, 97–100] and by computation with force field models or density functional theory. [97, 101–105] Rutile SnO_2 is tetragonal with the space group $P4/mnm$. The modes of symmetry B_{1g} , E_g , A_{1g} and B_{2g} are Raman active, and comprise motions of oxygen anions with respect to stationary tin cations, either perpendicular to the c axis (modes B_{1g} , A_{1g} and B_{2g}), or along the c axis (mode E_g).

Nonharmonic effects are known to be important for understanding the thermodynamic stability and the thermal transport properties of materials at elevated temperatures, but the anharmonic lattice dynamics of rutile SnO_2 is largely unknown. Perhaps the most complete experimental results are from Percy and Morosin's work in 1973. [65] They reported frequency shifts of Raman modes with

temperature and pressure, although the temperature range was below 480 K and no phonon broadening information was reported. The linewidth broadening of the A_{1g} mode was measured to 973 K by Sato and Asari, and compared well with results from shell model calculations. [102] Their results suggest that the anharmonicity of SnO_2 is large.

In our recent study on rutile TiO_2 , the pure anharmonicity gave shifts of Raman peaks that were as large as from quasiharmonicity. [106] In that study we developed a rigorous method of simultaneously fitting Raman peak widths and shifts with calculations from the kinematics of phonon-phonon interactions. The effects of cubic and quartic anharmonicity were separated, and these anharmonic effects were found to be dominated by phonon kinematics. This previous work on TiO_2 used kinematics calculated with a shell model, but in the present study on rutile SnO_2 , inconsistencies in the different shell model parameters from the literature motivated the use of *ab initio* methods to calculate phonon dispersions. The analysis and comparison of our present results on rutile SnO_2 with previous results on TiO_2 provides a better understanding of the anharmonic phonon dynamics in both.

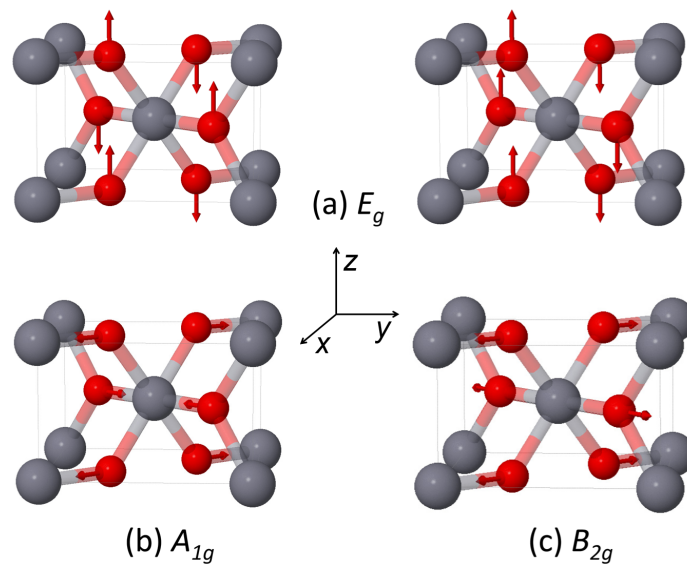


Figure 5.1: Rutile structure and oxygen atom displacements for Raman-active modes.

Here we report high resolution measurements of Raman spectra at temperatures from 83 to 873 K. Both phonon frequency shifts and broadenings are reported. The quasiharmonic effects from thermal expansion were separated from the anharmonic effects of phonon-phonon interactions by comparing the temperature dependence to the pressure dependence of the Raman peaks. The data fitting method used *ab initio* calculations of two-phonon kinematic functionals to identify the effects of cubic and quartic anharmonicity. The peak broadening originates with cubic anharmonicity, but the peak shifts depend on both cubic and quartic effects. The phonon-phonon kinematics explains an unusual feature in the temperature dependence of the broadening of the B_{2g} mode of rutile SnO_2 . The large difference in masses of Sn and O atoms causes a gap in the phonon density of states (DOS) that produces a peak in the two-phonon DOS (TDOS). The thermal shift moves the frequency of the B_{2g} mode away from this peak in the TDOS, and reduces the number of channels available for three-phonon processes, giving a concave-downwards curvature to the thermal broadening of the B_{2g} peak. The symmetrical B_{2g} mode was found to have a relatively large quartic anharmonicity.

5.2 Experimental Procedures

Measurements were performed on both powder and single crystal samples of rutile SnO_2 . The powder sample was prepared from commercial SnO_2 powder (Alfa Aesar, Ward Hill, MA) with a grain size of $10\ \mu\text{m}$. The powder was compressed into pellets of 1 mm thickness using a pressure of 50 MPa at ambient temperature. Raman spectra were acquired before and after compression into a pellet, and were found to be identical. A sample of single crystal casiterite of high optical quality was provided by the Mineral Museum of the Division of Geological and Planetary Sciences at the California Institute of Technology. The sample was cut and polished to a thickness of approximately 0.3 mm. Samples were mounted on the silver block of a Linkam thermal stage that provided excellent heat transfer and temperature stability for both heating and cooling. The sample chamber was sealed and purged

with nitrogen gas flow. A temperature controller drove a 200 W power supply for heating. For low temperature measurements, the stage was equipped with a coolant pump that injected liquid nitrogen directly into the silver block. Samples of powder pellets were measured at temperatures from 83 to 833 K, and the single crystal sample was measured from 83 to 873 K. Each temperature was held stable for 10 min before the spectrum was taken. The temperature precision was within 1 K.

The Raman spectra were measured with a Renishaw micro-Raman system with an Olympus LMPlanFI microscope lens. The spectrometer was configured in backscattering geometry, minimizing issues with the thickness of the sample. A depolarized solid state laser operated at wavelength of 514.5 nm excited the sample with the low incident power of 10 mW to avoid additional thermal heating. The laser spot size was 12 μm in diameter. To test for heating effects this spot size was varied, but no changes were found. Each Raman spectrum was accumulated in 10 measurements with 10 s exposure times.

5.3 Results

Representative Raman spectra of powder samples are shown in Fig. 5.2. Three of the four Raman-active modes, E_g , A_{1g} and B_{2g} , have enough intensity for extracting quantitative information on phonon frequencies and linewidths. The B_{1g} mode was too weak for obtaining quantitative information (its intensity is about three orders of magnitude smaller than that of the A_{1g} mode [97]). The single crystal sample showed very similar spectra, but the E_g mode was weaker primarily because of orientation effects. Three weak abnormal Raman bands that were previously reported [107] were also observed at 503, 545 and 692 cm^{-1} for both powder and single crystal samples.

After background subtraction, each peak in each spectrum was fitted to a Lorentzian function to obtain a centroid and full-width-at-half-maximum (FWHM). The FWHM data from the experiment were corrected for the finite resolution of the

spectrometer. [81] At room temperature, the Raman peak frequencies were 475 cm^{-1} for E_g , 633 cm^{-1} for A_{1g} , 774 cm^{-1} for B_{2g} . The mode frequencies at 83 K, $\omega(83\text{ K})$, were 476 cm^{-1} , 636 cm^{-1} and 778 cm^{-1} . Figure 5.3 presents results of peak shifts and widths versus temperature. Here the peak shift $\Delta\omega$ is defined as $\omega(T) - \omega(83\text{ K})$. We find good agreement with the frequency shift data reported by Peercy and Morosin at temperatures below 480 K. [65] We also find good agreement with the linewidth broadening data of the A_{1g} mode reported by Sato and Asari to 900 K. [102]

With increasing temperature, the A_{1g} and B_{2g} modes undergo large shifts to lower frequencies and significant linewidth broadenings, but the E_g mode undergoes less shift and broadening. At high temperatures above 500 K, the broadening of the B_{2g} mode shows an unusual concave downward curvature, while the other two modes broaden linearly. At low temperatures, the B_{2g} mode has a much larger linewidth than the other two modes. The linewidth of the B_{2g} mode extrapolated to 0 K is approximately 8 cm^{-1} , whereas the linewidths of the E_g and A_{1g} modes extrapolate to less than 2 cm^{-1} .

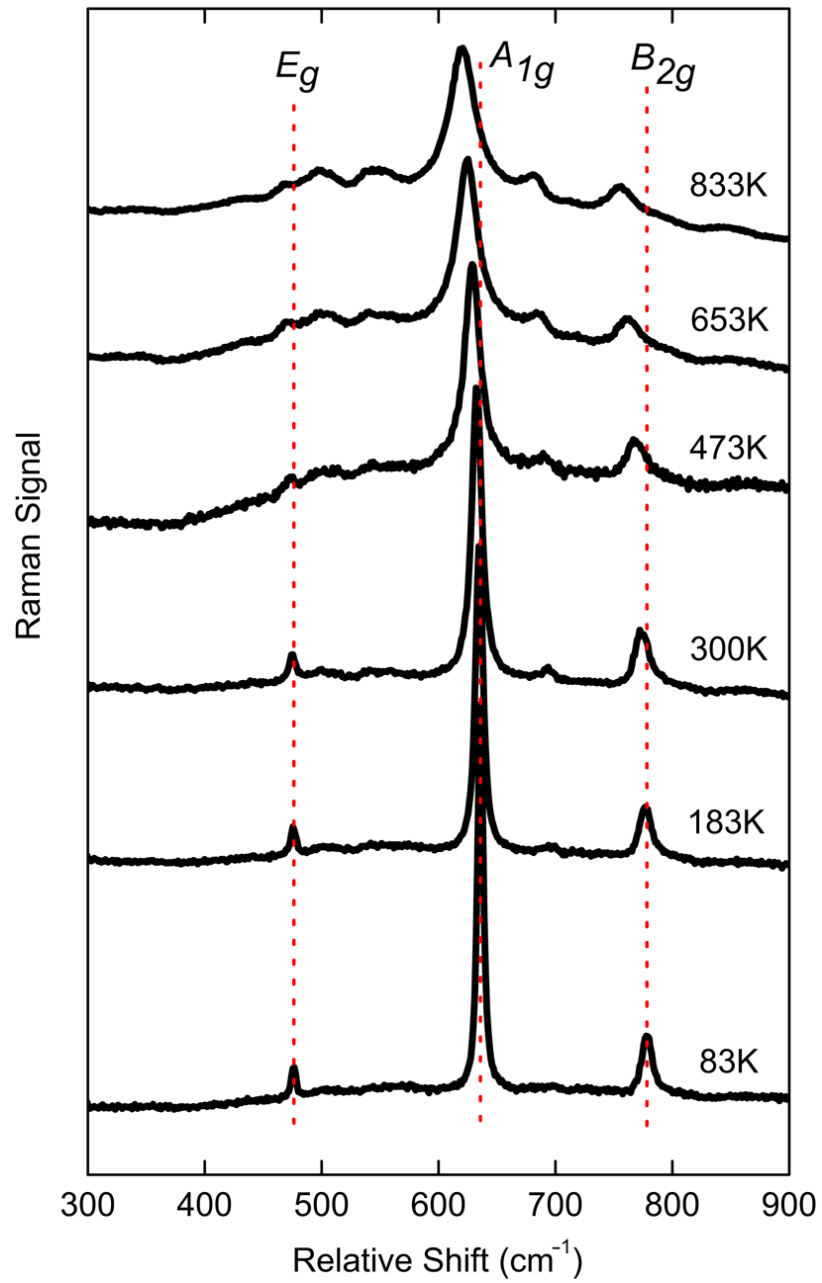


Figure 5.2: Raman spectra of powder samples of rutile SnO₂ at selected temperatures.

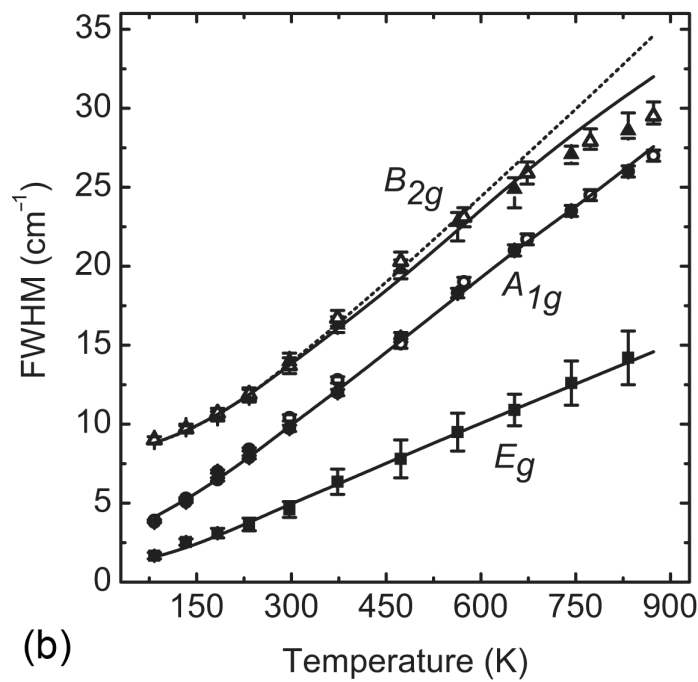
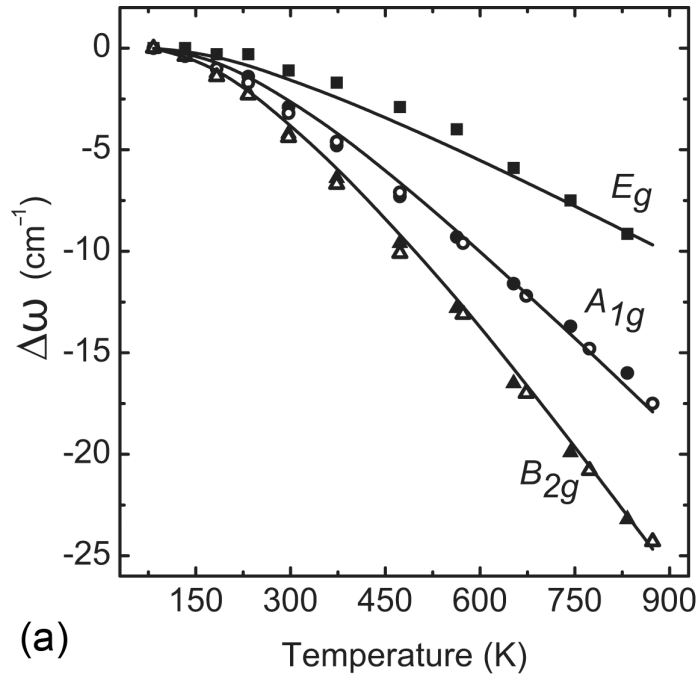


Figure 5.3: Temperature dependence of (a) frequency shifts, (b) breadths as FWHMs, of the Raman modes E_g , A_{1g} and B_{2g} . The solid and open symbols represent the experimental data from powder and single crystal samples, respectively. Solid curves are the theoretical fittings with a full calculation of the kinematics of three-phonon and four-phonon processes. The dashed curve was calculated without considering the frequency dependence of $D_{0l}(\Omega)$, the number of decay channels, at elevated temperatures.

5.4 Calculations

5.4.1 First Principles Lattice Dynamics

Phonon dispersion calculations over the whole Brillouin zone were performed with the QuantumEspresso package, within the framework of *ab initio* density functional perturbation theory (DFPT). [39] Vanderbilt ultrasoft pseudopotentials with the local density approximation (LDA) and nonlinear core corrections were used. The LO/TO splitting was corrected by adding a non-analytical part into the dynamical matrix. [40] The calculated dispersion curves are shown in Fig. 6.2a, and mode frequencies at the Γ -point are presented in Table 6.1. Calculations of the phonon density of states (DOS) with a uniform $16 \times 16 \times 16$ sampling grid were also performed, as shown in Fig. 6.2b. Our calculations are in good agreement with prior experimental and theoretical results. [97, 101–105] A band gap of width 100 cm^{-1} , centered around 400 cm^{-1} , is evident in Fig. 6.2. Above the gap, phonon modes are dominated by the motions of oxygen atoms.

Table 5.1: Comparison of the mode frequencies (cm^{-1}) at the Γ point for rutile SnO_2 . Calc1. is from the first principles LDA calculation from Borges, *et al.*, Ref. [105]; Calc2. is from Force field calculation by Katiyar, *et al.*, Ref. [97]. For expt., the data of infrared active modes at 100 K are from Katiyar, *et al.*, Ref. [97], and The data for Raman-active modes at 83 K are from the present measurement.

Mode	Present Calc.	Calc.	Calc.	Expt.
B_{1g}	104	83	100	121 ⁴
B_{1u}	147	138	140	-
$E_u^{(1)}(TO)$	223	200	236	244
$E_u^{(1)}(LO)$	269	252	268	276
$E_u^{(2)}(TO)$	285	270	297	293
$E_u^{(2)}(LO)$	335	307	377	366
A_{2g}	360	320	398	-
$A_{2u}(TO)$	456	457	512	477
E_g	468	462	476	476 ⁴
B_{1u}	564	553	505	-
$E_u^{(3)}(TO)$	613	584	651	618
A_{1g}	633	617	646	636 ⁴
$A_{2u}(LO)$	670	648	687	705
$E_u^{(3)}(LO)$	745	712	750	770
B_{2g}	765	734	752	778 ⁴

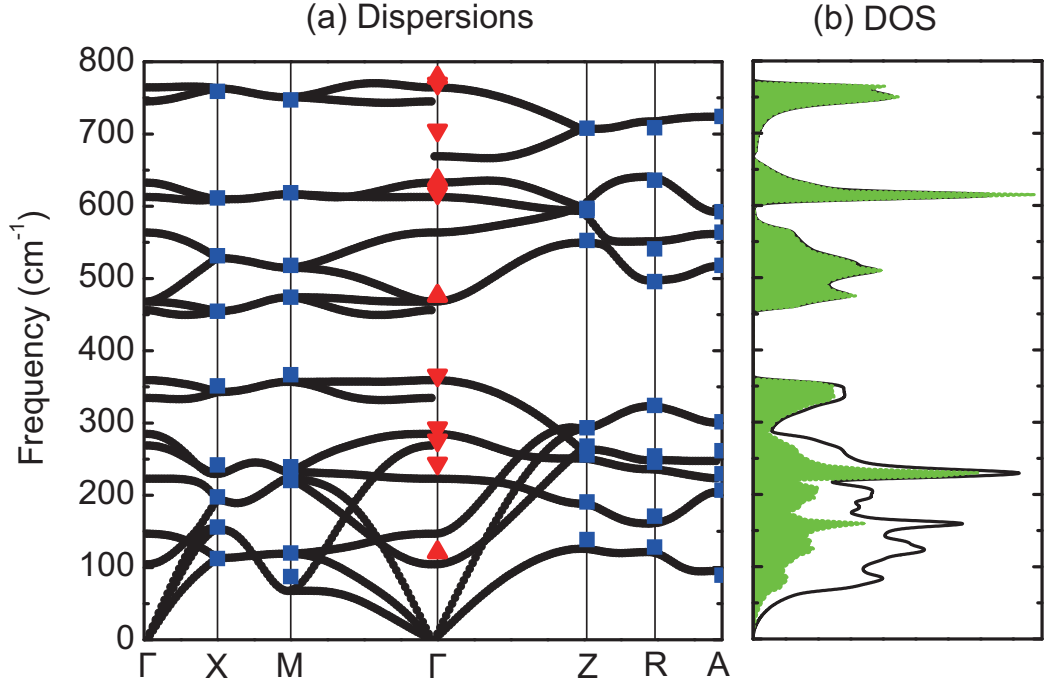


Figure 5.4: (a) Calculated phonon dispersion along high symmetry directions of rutile SnO_2 . Γ (0,0,0), X (0.5,0,0), M (0.5,0.5,0), Z (0,0,0.5), R (0.5,0,0.5) and A (0.5,0.5,0.5). At the Γ point, the frequencies from Table 6.1 are presented as up triangles (Raman) and down triangles (infrared). At the X, M, Z, R and A points, the mode frequencies from Ref. [[103]] (all doubly degenerate) are presented as squares. (b) Total phonon DOS (black curve) and oxygen-projected DOS (filled green).

5.4.2 The Kinematic Functionals $D^\omega(\Omega)$ and $P^\omega(\Omega)$

In anharmonic phonon perturbation theory, [2] the phonon linewidth is related to the two-phonon density of states (TDOS), $D(\Omega)$, which is defined as

$$\begin{aligned}
 D(\Omega) &= \sum_{\vec{q}_1, j_1} \sum_{\vec{q}_2, j_2} D(\Omega, \omega_1, \omega_2) \\
 &= \frac{1}{N} \sum_{\vec{q}_1, j_1} \sum_{\vec{q}_2, j_2} \Delta(\vec{q}_1 + \vec{q}_2) \left[(n_1 + n_2 + 1) \delta(\Omega - \omega_1 - \omega_2) \right. \\
 &\quad \left. + 2(n_1 - n_2) \delta(\Omega + \omega_1 - \omega_2) \right]
 \end{aligned} \tag{5.1}$$

where Ω is the frequency of the initial phonon, and phonon modes $\{\vec{q}_i j_i\}$ have quasiharmonic frequencies $\{\omega_i\}$ and occupancies $\{n_i\}$. The first and second terms in square brackets are from down-conversion and up-conversion phonon processes, respectively. [47]

The two-phonon kinematical functional $P(\Omega)$ for the anharmonic frequency shift is

$$\begin{aligned}
 P(\Omega) &= \sum_{\vec{q}_1, j_1} \sum_{\vec{q}_2, j_2} P(\Omega, \omega_1, \omega_2) \\
 &= \frac{1}{N} \sum_{\vec{q}_1, j_1} \sum_{\vec{q}_2, j_2} \Delta(\vec{q}_1 + \vec{q}_2) \wp \left[\frac{n_1 + n_2 + 1}{\Omega + \omega_1 + \omega_2} - \frac{n_1 + n_2 + 1}{\Omega - \omega_1 - \omega_2} \right. \\
 &\quad \left. + \frac{n_1 - n_2}{\Omega - \omega_1 + \omega_2} - \frac{n_1 - n_2}{\Omega + \omega_1 - \omega_2} \right] \quad (5.2)
 \end{aligned}$$

where \wp denotes the Cauchy principal part. The two-phonon spectra, $D(\Omega)$ and $P(\Omega)$, depend on temperature through the phonon occupancy factor, n . Both $D(\Omega)$ and $P(\Omega)$ were calculated at various temperatures from the first principles lattice dynamics calculations described in the previous subsection, sampling modes $\{\vec{q}j\}$ with a $16 \times 16 \times 16$ q -point grid over the first Brillouin zone for good convergence.

5.5 Analysis

5.5.1 Separating Anharmonicity from Quasiharmonicity

Both quasiharmonicity and pure anharmonicity contribute to the non-harmonic lattice dynamics of rutile SnO_2 . In the quasiharmonic model, phonon modes behave harmonically with infinite lifetimes, but their frequencies are altered by the effects of volume on the interatomic potential. Pure anharmonicity originates with phonon-phonon interactions, which increase with temperature. Pure anharmonicity contributes to shifts in phonon frequencies, but also causes phonon damping and lifetime broadening of phonon peaks. The large peak broadenings in SnO_2 show that there are large effects from pure anharmonicity.

To separate the peak shifts caused by pure anharmonicity from shifts caused by quasiharmonicity, we treat the mode frequency $\omega_j = \omega_j(V, T)$ as a function of volume and temperature [59]

$$\left(\frac{\partial \ln \omega_j}{\partial T}\right)_P = -\frac{\beta}{\kappa} \left(\frac{\partial \ln \omega_j}{\partial P}\right)_T + \left(\frac{\partial \ln \omega_j}{\partial T}\right)_V \quad (5.3)$$

where j is the phonon mode index, β is the volume thermal expansivity and κ is the isothermal compressibility. This is a general method to separate phonon quasiharmonicity from phonon anharmonicity, and is not unique for rutile structures, for example. The left-hand side gives the directly measurable temperature-dependent isobaric frequency shift, including both quasiharmonic and pure anharmonic behavior. The first term on the right-hand side, the isothermal frequency shift as a function of pressure, is the quasiharmonic contribution, which is also measurable. By defining a mode Grüneisen parameter as the proportionality of the relative change of the mode frequency to the relative change of volume, i.e., $\gamma_j = -\partial(\ln \omega_j)/\partial(\ln V)$, the quasiharmonic term can be written as $\gamma_j\beta$. The second term on the right of Eq. 6.7 is the frequency shift from the pure anharmonicity, which depends on temperature and not volume. From the difference of the isobaric and isothermal frequency shifts, the pure anharmonicity can be determined experimentally.

To obtain the quasiharmonic contributions to the peak shifts, we used the mode Grüneisen parameters γ_j reported recently by Hellwig, *et al.*, from Raman measurements at pressures to 14 GPa, [98] which agreed well with earlier high pressure measurements to 4 GPa. [108] These results suggest that Percy and Morosin overestimated the quasiharmonic contributions to their data, for which the pressure was only 0.4 GPa.

We also performed first principles calculations of the mode Grüneisen parameters by optimizing the enthalpy function to 10 GPa. Our calculated γ_j were in good agreement with the experimental results of Hellwig, *et al.*, and both are listed in Table 5.2. Since the γ_j are very weakly dependent on temperature, as is the thermal

Table 5.2: Frequencies of the three Raman modes, mode Grüneisen parameters, and the logarithmic pressure and temperature derivatives of frequency. Grüneisen parameters data from Hellwig, *et al.*, Ref. [98]. Thermal expansion data from Peercy and Morosin, Ref. [65]

Mode	$\omega(300\text{ K})$ (cm^{-1})	γ_j [expt.]	γ_j [calc.]	$\left(\frac{\partial \ln \omega}{\partial T}\right)_P$ (10^{-5}K^{-1})	=	$-\gamma_j \beta$ (10^{-5}K^{-1})	+	$\left(\frac{\partial \ln \omega}{\partial T}\right)_V$ (10^{-5}K^{-1})
E_g	475	1.45	1.48	-2.6		-1.7		-0.9
A_{1g}	633	1.65	1.81	-4.2		-1.9		-2.3
B_{2g}	774	1.49	1.71	-4.6		-1.7		-2.9

expansion above 400 K, [59, 65] the γ_j were assumed to be constants when assessing the volume dependent quasiharmonic contribution. The last two columns of Table 5.2 separate the measured isobaric temperature derivatives into the pure volume and pure temperature contributions as in Eq. 6.7. These last columns in Table 5.2 are the frequency shifts from quasiharmonicity and pure anharmonicity at temperatures above 400 K.

By comparing the last two columns in Table 5.2, we see that like rutile TiO_2 , the pure anharmonic contribution is comparable to the quasiharmonic contribution above 400 K. Nevertheless, the total anharmonicity of SnO_2 is considerably smaller than for TiO_2 . For the modes A_{1g} and B_{2g} in SnO_2 , the pure anharmonic contribution is larger than the quasiharmonic, while the E_g mode is more quasiharmonic. The relative magnitudes of pure anharmonicities of the three modes derived from the frequency shift data are consistent with the relative magnitudes of linewidth broadenings of the modes as shown in Fig. 5.3b.

5.5.2 Cubic and Quartic Anharmonicity

Anharmonicity tensors describe the coupling strengths for phonon-phonon interactions, but a prerequisite is that the phonons in these processes satisfy the kinematical conditions of conservation of energy and momentum. An anharmonicity

tensor element for an s -phonon process is [46]

$$V(j; \vec{q}_1 j_1; \dots; \vec{q}_{s-1} j_{s-1}) = \frac{1}{2s!} \left(\frac{\hbar}{2N} \right)^{\frac{s}{2}} N \Delta(\vec{q}_1 + \dots + \vec{q}_{s-1}) \times [\omega_{j_0} \omega_1 \dots \omega_{s-1}]^{\frac{1}{2}} C(j; \vec{q}_1 j_1; \dots; \vec{q}_{s-1} j_{s-1}) \quad (5.4)$$

where $\Delta(\vec{q}_1 + \dots + \vec{q}_{s-1})$ enforces momentum conservation and the $C(\cdot)$'s, elements of the s -phonon anharmonic tensor, are expected to be slowly-varying functions of their arguments. The cubic anharmonicity tensor has been calculated by first principles methods, [47, 109, 110] but to our knowledge the quartic anharmonicity tensor has never been fully calculated from first principles.

Nevertheless, if the anharmonicity tensor or its average does not vary significantly for different phonon processes, the coupling factor and the kinematic factor are approximately separable in Eq. 6.2. The separation of the anharmonic coupling and the kinematics has been used with success in many studies including our recent report on rutile TiO₂. [106] We consider the term $C(j; \vec{q}_1 j_1; \dots; \vec{q}_{s-1} j_{s-1})$ to be a constant of the Raman mode j , and use it as a fitting parameter. Although $C(j; \vec{q}_1 j_1; \vec{q}_2 j_2)$ and $C(j; j; \vec{q}_1 j_1; -\vec{q}_1 j_1)$ change with j_1 and j_2 , an average over modes, $\langle C(\cdot) \rangle = \sum_{1,2} C(j; \vec{q}_1 j_1; \vec{q}_2 j_2) / \sum_{1,2} 1$, is needed by the fitting, where 1, 2 under the summation symbol represent $\vec{q}_i j_i$. We define the cubic and quartic fitting parameters as

$$C_j^{(3)} = \langle C(j; \vec{q}_1 j_1; \vec{q}_2 j_2) \rangle \quad (5.5a)$$

$$C_j^{(4)} = \langle C(j; j; \vec{q}_1 j_1; -\vec{q}_1 j_1) \rangle \quad (5.5b)$$

To the leading order of cubic and quartic anharmonicity, the broadening of the Raman peaks is $2\Gamma^{(3)}(j; \Omega)$. The frequency shift of the Raman peaks is $\Delta^Q + \Delta^{(3)} + \Delta^{(3')} + \Delta^{(4)}$, where the quasiharmonic part Δ^Q is the integral form of the first term in Eq. 6.7. These quantities can be written as functions of $D(\Omega, \omega_1, \omega_2)$ and $P(\Omega, \omega_1, \omega_2)$,

weighted by average anharmonic coupling strengths [106]

$$\begin{aligned}\Gamma^{(3)}(j; \Omega) &= \frac{\pi\hbar}{64} \omega_{j0} |C_j^{(3)}|^2 \sum_{\vec{q}_{1,j_1}} \sum_{\vec{q}_{2,j_2}} \omega_1 \omega_2 D(\Omega, \omega_1, \omega_2) \\ &= \omega_{j0} |C_j^{(3)}|^2 D^\omega(\Omega)\end{aligned}\quad (5.6a)$$

$$\begin{aligned}\Delta^{(3)}(j; \Omega) &= -\frac{\hbar}{64} \omega_{j0} |C_j^{(3)}|^2 \sum_{\vec{q}_{1,j_1}} \sum_{\vec{q}_{2,j_2}} \omega_1 \omega_2 P(\Omega, \omega_1, \omega_2) \\ &= \omega_{j0} |C_j^{(3)}|^2 P^\omega(\Omega)\end{aligned}\quad (5.6b)$$

$$\Delta^{(3')} (j) = -\frac{\hbar}{16N} \omega_{j0} |C_j^{(3)}|^2 \sum_{\vec{q}_{2,j_2}} \omega_{j_2}(\vec{q}_2) \left(n_{\vec{q}_{2,j_2}} + \frac{1}{2} \right) \quad (5.6c)$$

$$\Delta^{(4)}(j) = \frac{\hbar}{8N} \omega_{j0} C_j^{(4)} \sum_{\vec{q}_{1,j_1}} \omega_{j_1}(\vec{q}_1) \left(n_{\vec{q}_{1,j_1}} + \frac{1}{2} \right) \quad (5.6d)$$

where $D^\omega(\Omega)$ and $P^\omega(\Omega)$ are functionals of $D(\Omega, \omega_1, \omega_2)$ and $P(\Omega, \omega_1, \omega_2)$ weighted by the kinematics of anharmonic phonon coupling. Figure 6.10 shows representative results for $D^\omega(\Omega)$ and $P^\omega(\Omega)$ at 0 K and 800 K. The down-conversion and up-conversion subspectra are also shown.

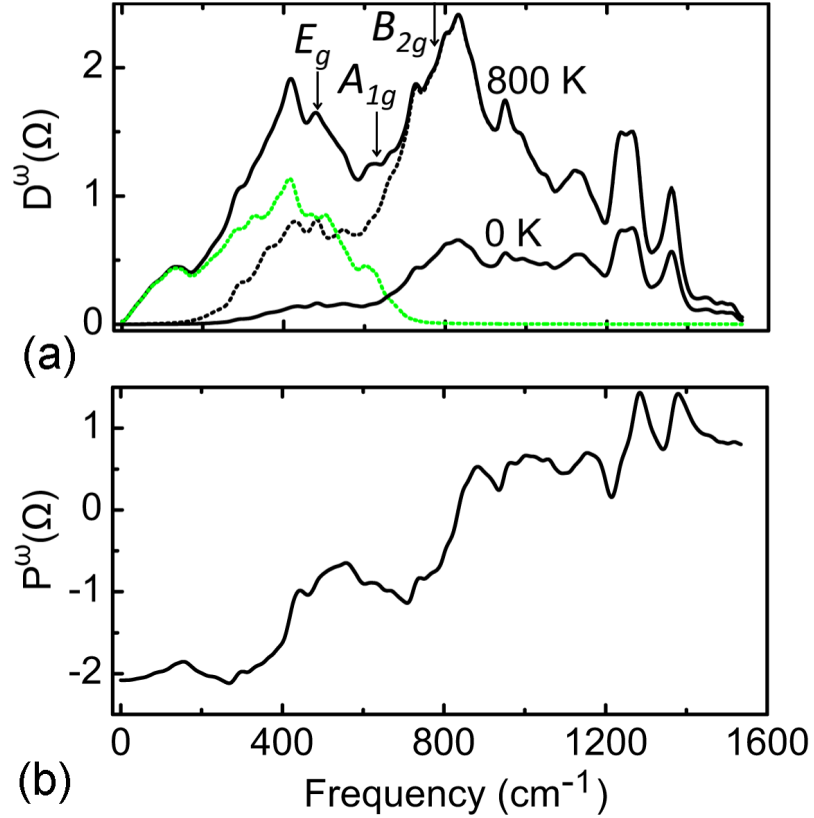


Figure 5.5: (a) Two-phonon density of states $D^\omega(\Omega)$ for 0 K and 800 K. The arrowheads mark the positions of the three Raman modes, E_g , A_{1g} and B_{2g} , respectively. The up-conversion and down-conversion contributions at 800 K are shown in green and black dash curves, respectively. There is no up-conversion process at 0 K. (b) $P^\omega(\Omega)$ at 800 K.

The $\Delta^{(3')}$ is an additional low-order cubic term that corresponds to instantaneous three-phonon processes. [2] It is nonzero for crystals having atoms without inversion symmetry, as in the case for the oxygen atom motions in the A_{1g} mode. It is much smaller than other contributions, however, owing to symmetry restrictions.

With Eq. 6.6 and rigorous calculations of $D^\omega(\Omega)$ and $P^\omega(\Omega)$ at various temperatures, for each Raman mode both its frequency shift and broadening were fitted simultaneously with the two parameters, $|C_j^{(3)}|^2$ and $C_j^{(4)}$. The best fits for the shifts and broadenings are shown in Fig. 5.3, and the fitting parameters are given in Table 5.3. Figure 5.6 also shows contributions to the shift from the quasi-harmonic and

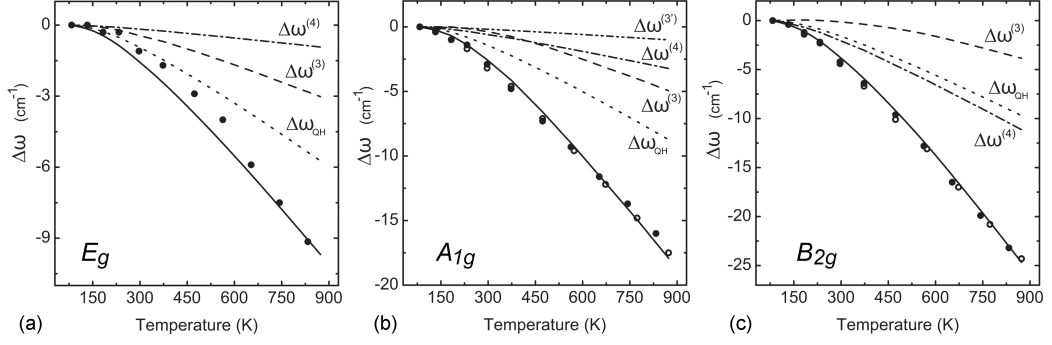


Figure 5.6: Fittings of the temperature dependence of frequency shift of (a) the E_g mode, (b) the A_{1g} mode and (c) the B_{2g} mode. Solid curves are the final fittings to $\Delta^Q + \Delta^{(3)} + \Delta^{(3')} + \Delta^{(4)}$. Different contributions are indicated individually in these figures.

pure anharmonicity (dashed curves).

Table 5.3: Fitting parameters for the temperature dependent Raman modes (unit: 10^{10} erg^{-1})

	E_g	A_{1g}	B_{2g}
$ C^{(3)} ^2$	0.87	1.6	1.0
$-C^{(4)}$	1.0	2.6	7.3

With a single parameter $|C^{(3)}|^2$ for each mode, good fittings to the broadenings are obtained as shown in Fig. 5.3b, indicating significant cubic anharmonicity for these Raman-active modes. Moreover, our fittings also successfully reproduced the unusual concave curvature of the B_{2g} mode at high temperatures. The $|C_j^{(3)}|^2$ do not vary much among different modes, suggesting the assumption of slowly-varying properties of $C(\cdot)$'s is reasonable.

Starting with the same cubic fitting parameters used for the broadenings, the frequency shifts of these modes are fit well by adding the quasi-harmonic and quartic anharmonic effects. As shown in Fig. 5.6, the quartic contribution $\Delta^{(4)}$ is generally of the same order as the cubic contribution $\Delta^{(3)}$, consistent with the fact that $\Delta^{(4)}$ and $\Delta^{(3)}$ are both leading-order terms for the anharmonic frequency shifts. For the E_g and A_{1g} modes, the pure anharmonicity is mainly from the cubic terms,

but for the B_{2g} mode, the quartic anharmonicity is dominant and is as large as the quasiharmonic part.

5.6 Discussion

We can understand why the B_{2g} mode has a relatively larger quartic anharmonicity than the A_{1g} from differences in how the O atoms move towards the Sn atoms. Using a unit cell with 4 O atoms and 2 Sn atoms, as shown in Fig. 5.1, the A_{1g} mode has all 4 O atoms moving directly into one Sn atom on one half of the cycle, but moving between two Sn atoms during the other half cycle. The B_{2g} mode has 2 O atoms moving into a Sn atom and 2 O atoms moving between two Sn atoms on both halves of the vibrational cycle, making for a potential that is an even function of the phonon coordinate. Table 5.3 shows a larger quartic contribution for the B_{2g} mode than the A_{1g} . (The E_g mode does not have similar atom motions for comparison.)

The TDOS function $D^\omega(\Omega)$ in Fig. 6.10 shows large variations with Ω that explains a trend in the thermal broadening of Fig. 5.3b. Owing to the high frequency of the B_{2g} mode, at the temperatures of this study its phonon-phonon anharmonicity comes mostly from down-conversion processes, as shown in Fig. 6.10. Ignoring the small up-conversion contribution, at high temperatures [48]

$$D^\omega(\Omega, T) \propto T \sum_{\vec{q}_1, j_1} \sum_{\vec{q}_2, j_2} \delta(\Omega - \omega_1 - \omega_2) \equiv T D_{0\downarrow}(\Omega) \quad (5.7)$$

where $D_{0\downarrow}(\Omega)$ is the number of two-phonon down-conversion channels. Usually the line broadening is linear in T because $D_{0\downarrow}(\Omega)$ does not vary much with temperature. However, the B_{2g} mode at 774 cm^{-1} lies on a steep gradient of $D^\omega(\Omega, T)$ in Fig. 6.10. Because the B_{2g} mode undergoes a significant shift of frequency with temperature, it moves down the gradient of $D^\omega(\Omega, T)$, and its broadening is less than linear in T . The temperature dependence of the broadening of the B_{2g} mode has an unusual concave downwards shape. For comparison, the dashed line in Fig. 5.3 was calculated without considering the frequency dependence of $D_{0\downarrow}(\Omega)$ at elevated

temperatures, and it deviates substantially from the experimental trend.

The unusual temperature dependence of the linewidth of the B_{2g} mode comes from the sharp peak in $D^\omega(\Omega, T)$ centered at 800 cm^{-1} . This feature in the TDOS originates with the phonon DOS of SnO_2 shown in Fig. 6.2, which has a band gap between 360 cm^{-1} to 450 cm^{-1} associated with the mass difference of Sn and O atoms. The shape of the TDOS can be understood as the convolution of the phonon DOS with itself. With two approximately equal regions above and below the gap, the result is a peak at 800 cm^{-1} , with steep slopes on both sides. For comparison, although the TDOS of rutile TiO_2 is shaped as a broad peak, [106] it does not have the sharp features of Fig. 6.10a because the mass difference between Ti and O atoms does not cause a band gap in the phonon DOS of TiO_2 .

Especially with more up-conversion processes at higher temperatures, there is another peak in the SnO_2 TDOS at 400 cm^{-1} . The up-conversion channels are primarily from the pairs of sharp peaks in the phonon DOS at 100 cm^{-1} and 500 cm^{-1} , 200 cm^{-1} and 600 cm^{-1} , and 350 cm^{-1} and 750 cm^{-1} . Although the E_g mode at 475 cm^{-1} is on the slope of this peak in the TDOS, the E_g mode does not show anomalous broadening with temperature because it undergoes only a small thermal shift in frequency.

In the low-temperature limit, up-conversion processes are prohibited because $n \rightarrow 0$. The peak linewidth extrapolated to 0 K is determined entirely by down-conversion processes, quantified by the down-conversion TDOS. [48] The B_{2g} mode has a significant broadening because its frequency is near a peak in the down-conversion TDOS, as seen in Fig. 6.10. On the other hand, the E_g and A_{1g} modes are not broadened at low temperatures because their frequencies are at low values of the TDOS. The phonon-phonon kinematics accounts for the significant difference of linewidths between the B_{2g} and the other two Raman modes at low temperatures.

5.7 Conclusions

Raman spectra were measured on rutile SnO₂ at temperatures from 83 to 873 K, and large anharmonic shifts and broadenings were found for the three measurable Raman peaks. Individual assessments of the cubic and quartic contributions to the anharmonicity were performed by calculating the kinematics of 3-phonon and 4-phonon processes with *ab initio* methods, and varying the anharmonic coupling parameters to fit the peak shifts and broadenings simultaneously. The quartic anharmonicity of the B_{2g} mode was found to be large, unlike the E_g and A_{1g} modes for which cubic anharmonicity is dominant. The quartic behavior of the B_{2g} mode can be understood from the symmetry of the oxygen atom displacements.

The phonon DOS of SnO₂ has a band gap around 400 cm⁻¹ owing to the mass difference of Sn and O atoms, with similar structure above and below the gap. This causes a sharp peak in the TDOS at 800 cm⁻¹. The frequency of the B_{2g} mode is on the slope of this peak in the TDOS, and its frequency shift with temperature reduces the number of down-conversion channels for its broadening. The thermal broadening of the B_{2g} mode consequently shows an anomalous concave downwards curvature. At 0 K, the large TDOS around 800 cm⁻¹ explains the large linewidth of the B_{2g} mode. The anharmonic peak shifts and broadenings were well accounted for by the kinematics of phonon-phonon interactions, suggesting that on the average, the anharmonicity tensors for rutile SnO₂ are not rich in structure.

Chapter 6

Phonon Anharmonicity of Ag_2O with Cuprite Structure

The main content of this chapter appeared in the journal article: Tian Lan, Chen W. Li, Jennifer L. Niedziela, Hillary Smith, Douglas L. Abernathy, George R. Rossman, and Brent Fultz *Physical Review B* **89**, 054306 (2014)

Inelastic neutron scattering measurements on silver oxide (Ag_2O) with the cuprite structure were performed at temperatures from 40 to 400 K, and Fourier transform far-infrared spectra were measured from 100 to 300 K. The measured phonon densities of states and the infrared spectra showed unusually large energy shifts with temperature, and large linewidth broadenings. First principles molecular dynamics (MD) calculations were performed at various temperatures, successfully accounting for the negative thermal expansion (NTE) and local dynamics. Using the Fourier-transformed velocity autocorrelation method, the MD calculations reproduced the large anharmonic effects of Ag_2O , and were in excellent agreement with the neutron scattering data. The quasiharmonic approximation (QHA) was less successful in accounting for much of the phonon behavior. The QHA could account for some of the NTE below 250 K, although not at higher temperatures. Strong anharmonic effects were found for both phonons and for the NTE. The lifetime broadenings of Ag_2O were explained by anharmonic perturbation theory, which showed rich interactions between the Ag-dominated modes and the O-dominated modes in both up- and down-conversion processes.

6.1 Introduction

Silver oxide (Ag_2O) with the cuprite structure has attracted much interest after the discovery of its extraordinarily large negative thermal expansion (NTE), [111,112] which exceeds $-1 \times 10^{-5} \text{ K}^{-1}$ and occurs over a wide range of temperature from 40 K to its decomposition temperature near 500 K. Besides its large NTE, Ag_2O is commonly used as a modifier in fast-ion conducting glasses and batteries, [113,114] and its catalytic properties are also of interest. [115,116]

In the cuprite structure of Ag_2O shown in Fig. 6.1, the fcc Ag lattice is expanded by the presence of the O atoms, which form an interpenetrating bcc lattice. The O atoms occupy two tetrahedral sites of the standard fcc unit cell of Ag atoms. Each O atom is linked to four O atoms through a bridging Ag atom, placing the Ag atoms in linear O-Ag-O links with little transverse constraint. A geometrical model of

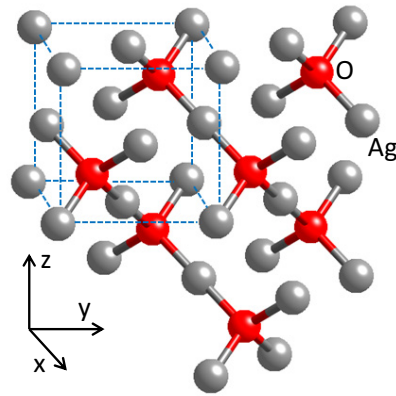


Figure 6.1: Cuprite structure of Ag_2O , showing standard cubic fcc unit cell and O-Ag-O links that pass between cubes.

NTE considers tetrahedra of Ag_4O around each O atom that bend at the Ag atoms linking the O atoms in adjacent tetrahedra. Rigid-unit modes (RUMs) account for counteracting rotations of all such tetrahedra. [117, 118] These RUMs tend to have low frequencies owing to the large mass of the unit, and hence are excited at low temperatures. Locally, the O-Ag bond length does not contract, but bending of the O-Ag-O links pulls the O atoms together, leading to NTE. This model correlates the NTE and lattice dynamics. Similar models seem to explain the large NTE of ZrW_2O_8 and other systems.

The RUM model has value even if the Ag_4O tetrahedra do not move as rigid units, but the interpretation of NTE becomes less direct. A related concern is that modes involving bending of the O-Ag-O links may be strongly anharmonic. In a recent study on ScF_3 , for example, the NTE largely originated with the bending of linear Sc-F-Sc links. [119] Frozen phonon calculations showed that the displacement of F atoms in these modes followed a nearly quartic potential, and the low mass of F made it possible to approximate the problem as independent local quartic oscillators. The heavy mass of the Ag atoms in the O-Ag-O links implies that different Ag atoms will move cooperatively, and delocalized anharmonic oscillators are challenging to understand.

Recent measurements by high-resolution x-ray diffractometry and extended x-

ray absorption fine structure spectrometry (EXAFS) showed large deformations of the Ag_4O tetrahedra. [120–123] Although these tetrahedra are not distorted by a pure RUM, the simultaneous excitation of other modes makes it unrealistic to view the dynamics as motions of rigid framework units. Measurements by EXAFS also showed that the average Ag-O nearest-neighbor distance expands slightly upon heating, but the Ag-Ag next-nearest neighbor distance contracts approximately as expected from the bulk NTE.

Anharmonic phonon behavior is known to be important for the thermodynamics and the thermal conductivity of materials at elevated temperatures. It is also important for the thermodynamic stability of phases. [124, 125] Anharmonic phonon behavior is sometimes associated with NTE, but such relationships are not well understood, and helped motivate the present study.

Inelastic neutron scattering is a powerful method to measure phonon dynamics, allowing accurate measurements of vibrational entropy. [93] Additionally, phonon energy broadening can be measured, allowing further assessment of how anharmonic effects originate from the non-quadratic parts of the interatomic potential. A recent inelastic neutron scattering experiment on Ag_2O with the cuprite structure showed phonon softening (reduction in energy) with temperature. [126] The authors interpreted this result with a quasiharmonic model, where they calculated harmonic phonons for reduced volumes of the structure and obtained a negative Grüneisen parameter. These measurements were performed on the neutron energy gain side of the elastic line, restricting measurements to temperatures above 150 K, and the available energy range of 20 meV allowed about a quarter of the Ag_2O phonon spectrum to be measured.

Lattice dynamics calculations, based on either classical force fields or density functional theory (DFT), have been used to study materials with the cuprite structure. [126–128] All these calculations were performed with the quasiharmonic approximation (QHA), where the interatomic forces and phonon frequencies changed with volume, but all phonons were assumed to be harmonic normal modes with infinite lifetimes. This QHA ignores interactions of phonons at finite temperatures

through the cubic or quartic parts of the interatomic potential, but these interactions are essential to explicit phonon anharmonicity. Although the QHA calculation accounted for the NTE behavior in ZrW_2O_8 , [129] for Ag_2O with the cuprite structure, the QHA was only partly successful. Molecular dynamics (MD) simulations should be reliable for calculating phonon spectra in strongly anharmonic systems, [72, 130, 131] even when the QHA fails. To our knowledge, no MD investigation has yet been performed on Ag_2O with the cuprite structure.

To study phonon anharmonicity in Ag_2O , and its possible relationship to NTE, we performed temperature-dependent inelastic neutron scattering experiments at temperatures from 40 to 400 K to obtain the phonon density of states (DOS). (At temperatures below 40 K a first-order phase transition occurs, giving a temperature-dependent fraction of a second phase with different phonon properties [112, 132].) Fourier transform infrared spectrometry at cryogenic temperatures was also used to measure the frequencies and lineshapes of phonons at the Γ -point of the Brillouin zone. First-principles ab-initio MD simulations were performed, and by Fourier transforming the velocity autocorrelation function, the large temperature-dependent phonon anharmonicity was reproduced accurately. An independent calculation of anharmonic phonon interaction channels was performed with interacting phonon perturbation theory, and semiquantitatively explained anharmonicities of the different phonons. Most of the phonons have many channels for decay and are highly anharmonic. Although the QHA is capable of predicting about half of the NTE at low temperatures, part of this NTE is associated with anharmonicity, and most of the NTE above 250 K originates with anharmonic interactions between Ag-dominated and O-dominated phonon modes.

6.2 Experiments

6.2.1 Inelastic Neutron Scattering

Inelastic neutron scattering measurements were performed with the wide angular-range chopper spectrometer, ARCS, [13] at the Spallation Neutron Source at Oak Ridge National Laboratory. Powder samples of Ag_2O with the cuprite structure of 99.99% purity were loaded into an annular volume between concentric aluminum cylinders with an outer diameter of 29 mm and an inner diameter of 27 mm, giving about 5% scattering of the incident neutron beam. The sample assembly was mounted in a bottom-loading closed cycle refrigerator outfitted with a sapphire hot stage that can be controlled independently of the second stage of the cryostat. Spectra were acquired with two incident neutron energies of approximately 30 and 100 meV. Measurements were performed at temperatures of 40, 100, 200, 300 and 400 K, each with approximately 1.6×10^6 neutron counts. Backgrounds with empty sample cans were measured at each temperature. Ag has an absorption cross section of 63 barns, but this was not be a problem with low background and high neutron flux.

The raw data were rebinned into intensity I as a function of momentum transfer Q and energy transfer E . After deleting the elastic peak around zero energy, neutron-weighted phonon densities of states curves were calculated from $I(Q, E)$ by subtracting the measured background, and using an iterative procedure to remove contributions from multiple scattering and higher-order multiphonon processes. [133]

6.2.2 Fourier Transform Far-Infrared Spectrometer

The far-infrared spectrometry measurements were performed with a Thermo-Nicolet Magna 860 FTIR spectrometer using a room-temperature deuterated triglycine sulfate detector and a solid substrate beam splitter. The same Ag_2O powder was mixed with polyethylene fine powder with a mass ratio of 1:19 and finely ground.

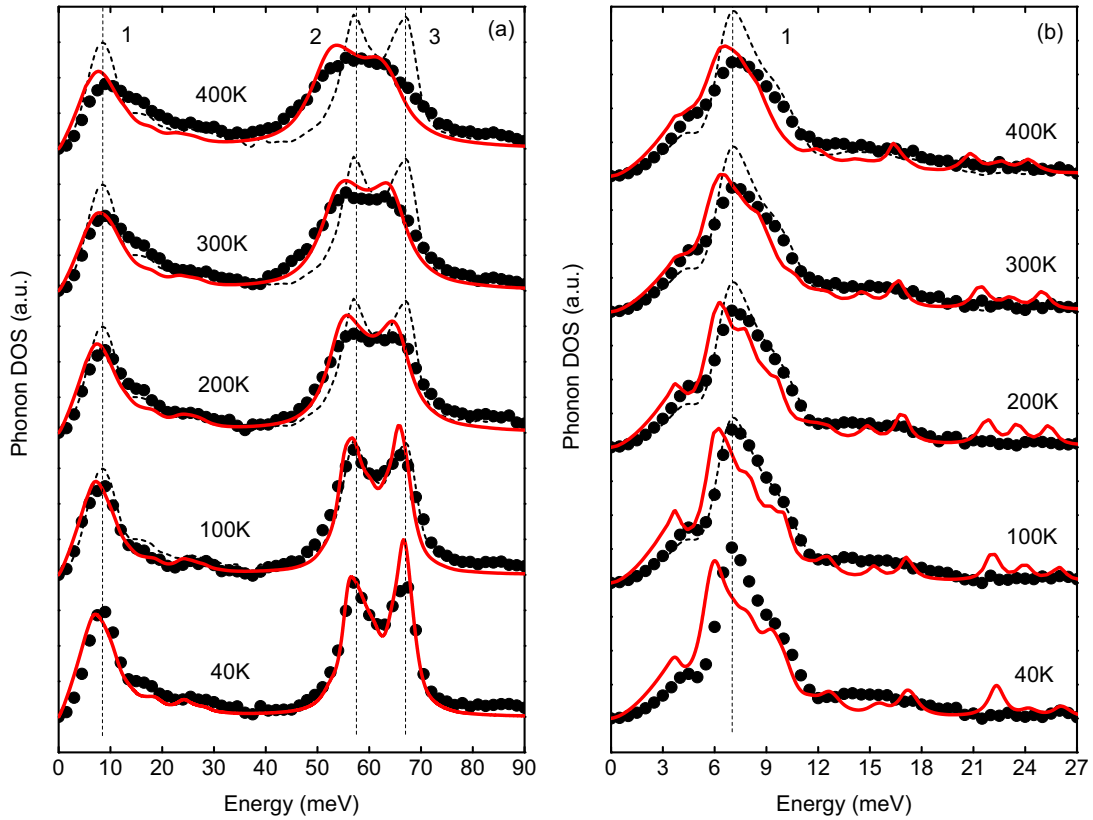


Figure 6.2: Neutron weighted phonon DOS of Ag_2O with the cuprite structure from ARCS experimental data (black dots) and MD simulations (red curves) at temperatures from 40 to 400 K. The dashed spectrum corresponds to the 40 K experimental result, shifted vertically for comparison at each temperature. Vertical dashed lines are aligned to the major peak centers at 40 K from experiments, and are numbered at top. The incident energy was 100 meV for panel (a), and 30 meV for panel (b).

The sample was compressed into a pellet of 1 mm thickness, and mounted on a copper cold finger of an evacuated cryostat filled with liquid nitrogen. The cryostat had polyethylene windows that were transparent in the far-infrared. Spectra were acquired at temperatures from 100 to 300 K, and temperature was measured with a thermocouple in direct contact with the sample pellet. Backgrounds from a pure polyethylene pellet of the same size were measured at each temperature.

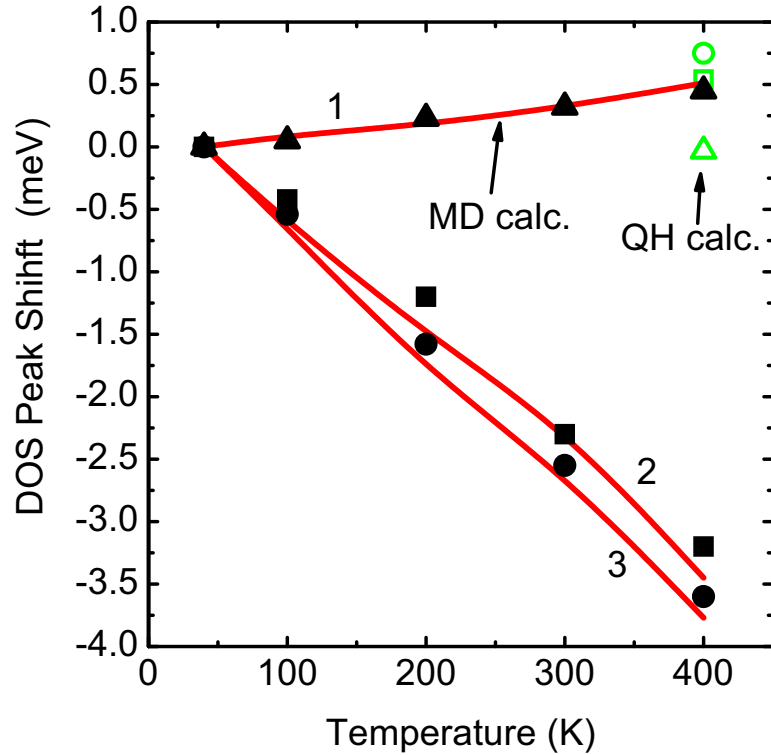


Figure 6.3: Shifts of centers of peaks in the phonon DOS, relative to data at 40 K. The filled symbols are experimental data, open symbols (green) are from MD-based QHA calculations and solid curves (red) are from MD calculations. Indices 1, 2, 3 correspond to the peak labels in Fig. 6.2, and are also represented by the triangle, square and circle respectively for experimental data and QHA calculations.

6.2.3 Results

Figure 6.2 presents the “neutron-weighted” phonon DOS of Ag_2O with the cuprite structure from ARCS data at two incident energies at temperatures from 40 to 400 K. Neutron-weighting is an artifact of inelastic neutron scattering by phonons. Phonon scattering scales with the scattering cross section divided by atom mass, σ/m , so the Ag-dominated modes around 8 meV are relatively weaker than the O-dominated modes around 63 meV. Since the instrument energy resolution is inversely related to both the incident energy and the energy transfer, the spectra in Fig. 6.2(b) have generally higher resolution than in Fig. 6.2(a). As shown in Fig. 6.2, the main features (peaks 1, 2 and 3) of the DOS curve from inelastic neutron scattering experiments undergo substantial broadening with temperature,

even below 200 K, indicating an unusually large anharmonicity. Along with the broadening, peak 1 stiffens slightly, but peaks 2 and 3 shift to lower energy by more than 3.2 meV. This is an enormous shift over such a small temperature range. Over the same temperature range, phonons of ScF_3 shifted by about 1 meV, for example. [119] To quantify thermal shifts, Gaussian functions were fitted to the three major peaks in the phonon DOS, and Fig. 6.3 presents the peak shifts relative to their centers at 40 K.

Figure 6.4 presents the infrared spectra of Ag_2O between 50 and 650 cm^{-1} . Two absorption bands at 86 cm^{-1} and 540 cm^{-1} are seen, consistent with previous measurements at room temperature [134]. Analysis by group theory showed they have F_{1u} symmetry. The low frequency mode at 86 cm^{-1} is an Ag-O-Ag bending mode, while the high frequency band corresponds to Ag-O stretching. Consistent with the trend of phonon DOS measured by neutron scattering, the high frequency band broadened significantly with temperature. From 100 to 300 K, the two modes shifted to lower energy by about 4 cm^{-1} and 13 cm^{-1} , respectively.

6.3 First-Principles Molecular Dynamics Simulations

6.3.1 Methods

First-principles calculations were performed with the generalized gradient approximation (GGA) of density functional theory (DFT), implemented in the VASP package. [135–137] Projector augmented wave pseudopotentials and a plane wave basis set with an energy cutoff of 500 eV were used in all calculations.

First-principles Born-Oppenheimer molecular dynamics simulations were performed for a $3 \times 3 \times 3$ supercell with temperature control by a Nosé thermostat. The relatively small simulation cell could be a cause for concern. [138] As shown in Fig. 6.5, we did the convergence test for different sizes of cells, and the test showed that the supercell in our study is large enough to accurately capture the phonon anharmonicity of Ag_2O . We also did the convergence test for different simulation

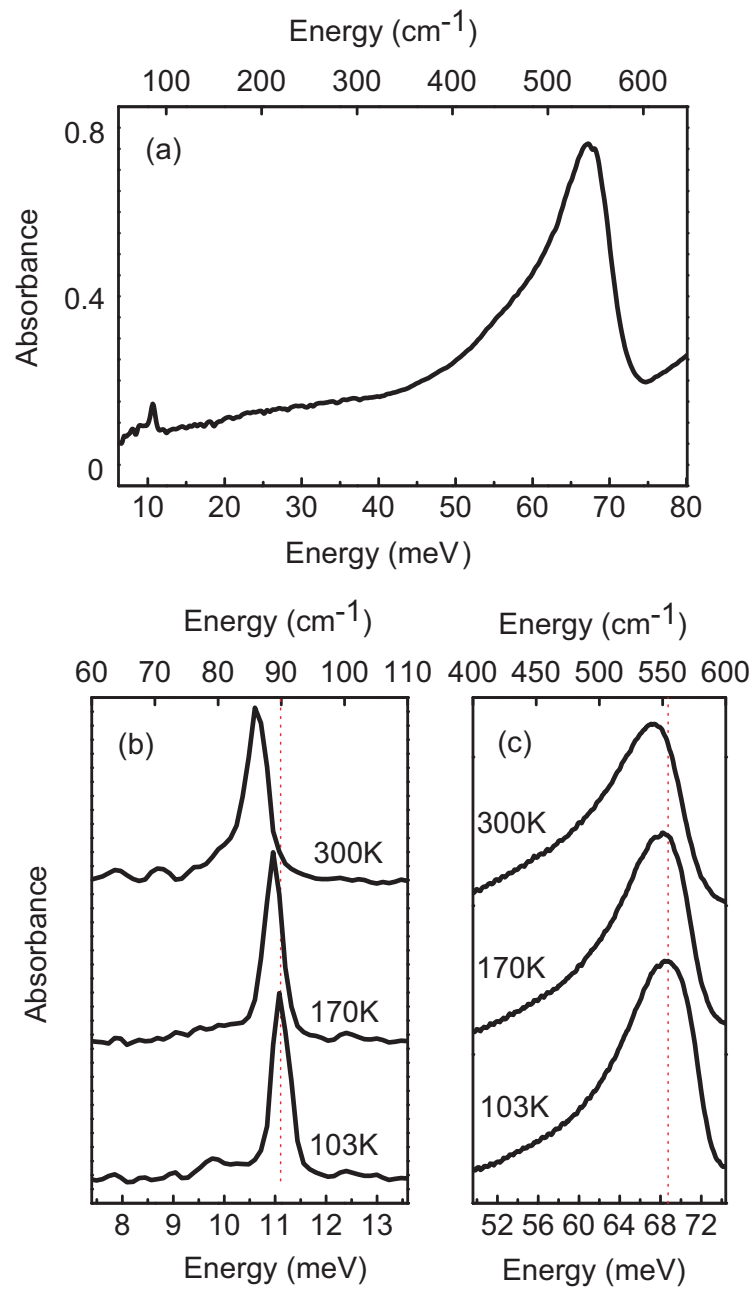


Figure 6.4: (a) FT-IR absorption spectra of Ag_2O with the cuprite structure at 300 K. (b), (c) Enlargement of two bands at selected temperatures.

time. As shown in Fig. 6.6, the simulated phonon spectra were well converged after 12 ps simulation time. The simulated temperatures included 40, 100, 200, 300 and 400 K. For each temperature, the system was first equilibrated for 3 ps, then simulated for 18 ps with a time step of 3 fs. The system was fully relaxed at each temperature, with convergence of the pressure within 1 kbar.

Phonon frequency spectra and their k -space structure were obtained from the MD trajectories by the Fourier transform velocity autocorrelation method. [45,72, 130,131] The phonon DOS is

$$g(\omega) = \sum_{n,b} \int dt e^{-i\omega t} \langle \vec{v}_{n,b}(t) \vec{v}_{0,0}(0) \rangle \quad (6.1)$$

where $\langle \rangle$ is an ensemble average, and $\vec{v}_{n,b}(t)$ is the velocity of the atom b in the unit cell n at time t . Individual phonon modes could also be projected onto each k -point in the Brillouin zone by computing the phonon power spectrum. [72,131] To better compare with data from inelastic neutron scattering, the calculated DOS at each temperature was convoluted with the ARCS instrumental broadening function, and was neutron-weighted appropriately. [119,133]

Calculations in the quasiharmonic approximation were performed two ways. In the lattice dynamics method, the thermal expansion was evaluated by optimizing the vibrational free energy as a function of volume. [119] Calculations were performed self-consistently with a 6-atom unit cell with a $10 \times 10 \times 10$ k -point grid. Phonon frequencies were calculated using the small displacement method implemented by the Phonopy package. [139] These phonon dispersions in the QHA were also used for the anharmonic perturbation theory described below. The second method used MD calculations to implement the QHA. We removed the temperature-dependent explicit anharmonicity by performing simulations at 40 K for volumes characteristic of 400 K, which produced a pressure of 0.45 GPa at 40 K. Further computational details are given in Section 6.5.1.

At the lowest simulation temperature of 40 K, classical MD trajectories may require justification. In principle, nuclear motions could be better treated by mapping

each nucleus onto a classical system of several fictitious particles governed by an effective Hamiltonian, derived from a Feynman path integral, for example. [32,33] Such low temperature quantum effects are beyond the scope of this work. Nevertheless, our results should not be altered significantly by quantum effects for the following reasons. Our particular interest is in anharmonic phonon-phonon interactions at higher temperatures, and our new results concern the phonons and NTE above 250 K. A classical MD simulation is usually appropriate at higher temperatures. The modes most subject to quantum corrections are those involving the dynamics of the lower mass O atoms, but these are at high energies. They are not activated at 40 K, and show weak anharmonic effects. Relatively larger anharmonic effects at low temperatures are found in the modes below 10 meV. These are dominated by the Ag atoms, but with their high mass only tiny quantum effects are expected. There are several semi-quantitative methods to estimate the magnitudes of quantum corrections. For example, Berens, *et al.* [140] and Lin, *et al.* [44] suggest that quantum effects could be evaluated from the difference between the quantum and classical vibrational energy or free energy derived from the corresponding partition functions. These methods do not account for all quantum effects on nuclear trajectories, but for Ag₂O at 40 K, by using both classical and quantum partition function for the same phonon DOS, we found the vibrational energy difference between classical and quantum statistics is only 1.2% of the cohesive energy.

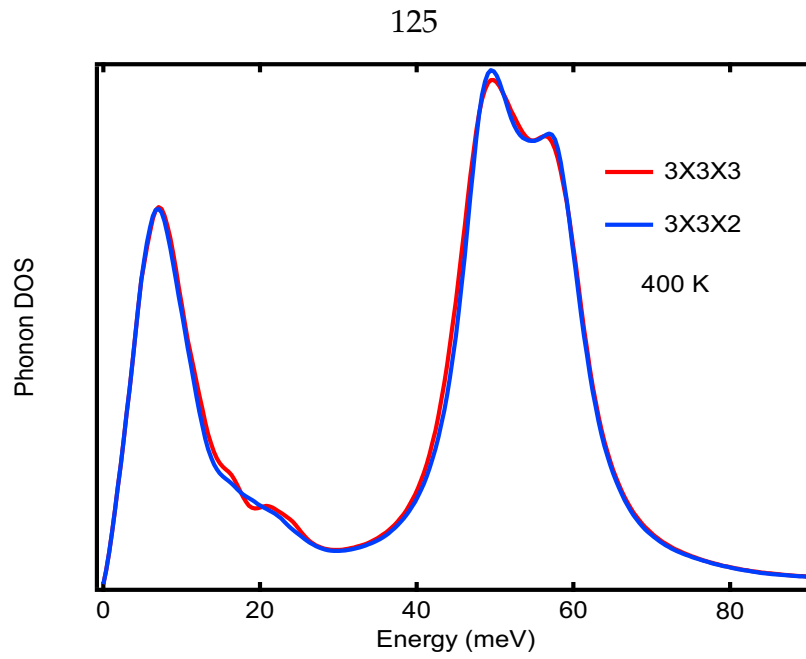


Figure 6.5: The phonon densities of states for two different cells used in molecular dynamics simulations at 400 K.

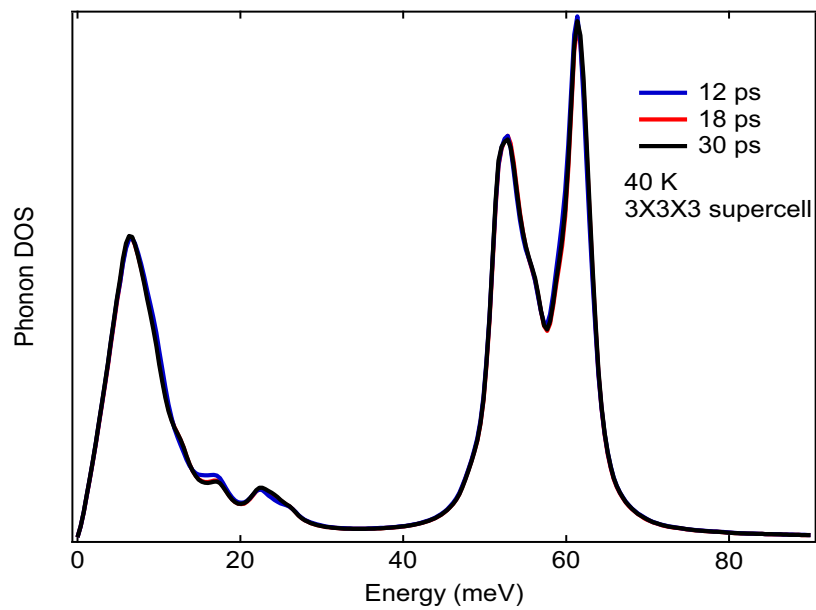


Figure 6.6: The simulated phonon densities of states for 12, 18 and 30 ps at 40 K

6.3.2 Results

Table 6.1 presents results from our MD simulations and experimental data on lattice parameter, bulk modulus, thermal expansivity, and phonon frequencies at the Γ -point. As shown in Fig. 6.7, the MD simulations predicted the NTE very well. On the other hand, consistent with a recent QHA calculation, [126] the NTE calculated with the QHA method was much smaller.

The phonon DOS curves calculated from first-principles MD simulations are shown in Fig. 6.2 with the experimental spectra for comparison. To facilitate visual comparison, in Fig. 6.2(a) the energy axis of the calculated spectra were scaled by 6.8% to correct for underestimates of the force constants in the GGA method. Nevertheless, excellent agreement is found between the simulated phonon DOS and the experimental data, and the calculated thermal broadenings and shifts are in good agreement, too. Gaussian functions were also fit to the calculated spectra, and Fig. 6.3 compares these thermal shifts from experiment and calculation.

Because of the large mass difference between Ag and O atoms, the O-dominated phonon modes are well separated from the Ag-dominated modes. Partial phonon DOS analysis showed that the Ag-dominated modes had similar energies, forming the peak of the phonon DOS below 20 meV (peak 1 in Fig. 6.2), whereas the O-dominated modes had energies above 40 meV (peaks 2 and 3).

Figure 6.8 shows the normal modes from MD simulations, projected to the Γ -point. Six vibrational modes are evident, including the IR-active $F_{1u}^{(1)}$ and $F_{1u}^{(2)}$ modes. The calculated frequencies of these modes at 40 K are listed in Table 6.1, showing good agreement with experiment. Large thermal shifts and broadenings are apparent in the simulated frequencies, consistent with experiment. The calculated peaks were then fitted with Lorentzian functions to extract the centroids and linewidths, which compare well with the FT-IR data as shown in Fig. 6.9.

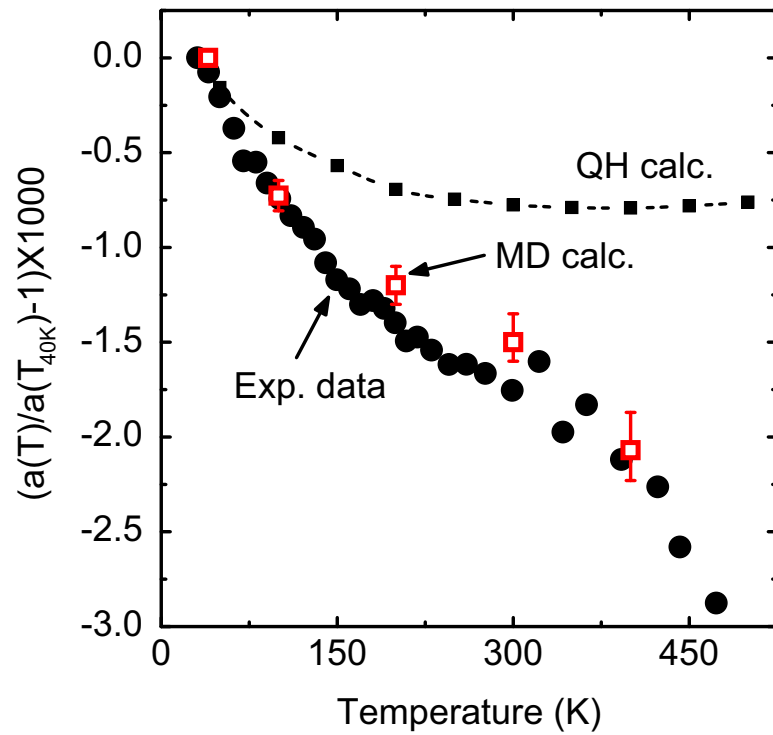


Figure 6.7: Temperature dependence of lattice parameter from experimental data in Ref. [111], quasiharmonic calculations and MD calculations, expressed as the relative changes with respect to their 40 K values, i.e., $a(T)/a(40 \text{ K}) - 1$.

Table 6.1: Properties of Ag_2O with the cuprite structure from present MD calculations, compared to experimental data. Units: lattice parameters in \AA , bulk modulus in GPa, thermal expansion coefficients in 10^{-6}K^{-1} , vibrational frequencies in meV. Lattice parameter at 40 K is from neutron scattering measurements in the present work, which is in good agreement with Refs. [[111, 112]]. Bond linear thermal expansion (LTE) and variance data are from Refs. [[121, 122]]. The IR active mode frequencies are from FT-IR measurements in the present work, and the frequencies of the lowest two modes are from the luminescence spectra in Ref. [141].

	Experiment	Calculation
Lattice Parameter		
a	4.746	4.814
Bulk Modulus		
K	N/A	72
Bond LTE		
$\beta_{\text{Ag-O}}$	12.1–35.0	19.4
$\beta_{\text{Ag-Ag}}$	-9.99	-14.7
Bond Variance		
$\sigma_{\text{Ag-Ag}}$ (40 K)	0.0078	0.0073
$\sigma_{\text{Ag-Ag}}$ (400 K)	0.053	0.067
Mode Frequency		
F_{2u}	5.60	5.58
E_u	8.9	7.45
$F_{1u}^{(1)}$	11.2	11.5
A_{2u}	N/A	29.4
F_{2g}	N/A	48.4
$F_{1u}^{(2)}$	67	63.6

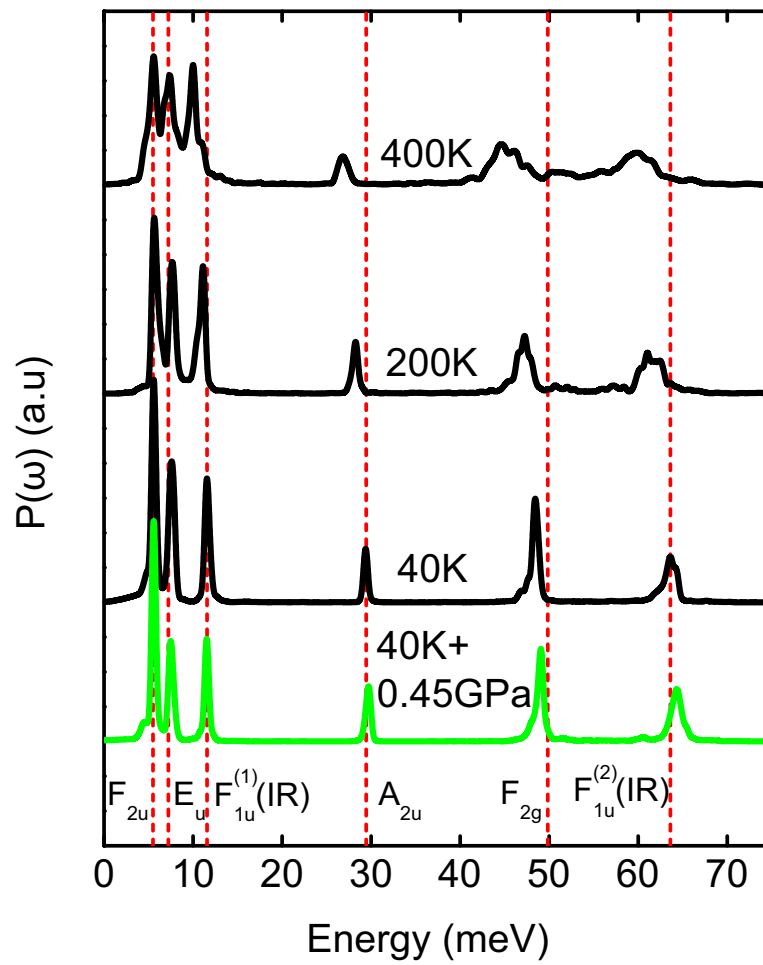


Figure 6.8: Phonon modes simulated by MD and projected on the Γ -point, at temperatures and pressures as labeled. The normal-mode frequencies calculated from harmonic lattice dynamics are shown as vertical dashed lines in red. The group symmetry for each mode is shown at the bottom.

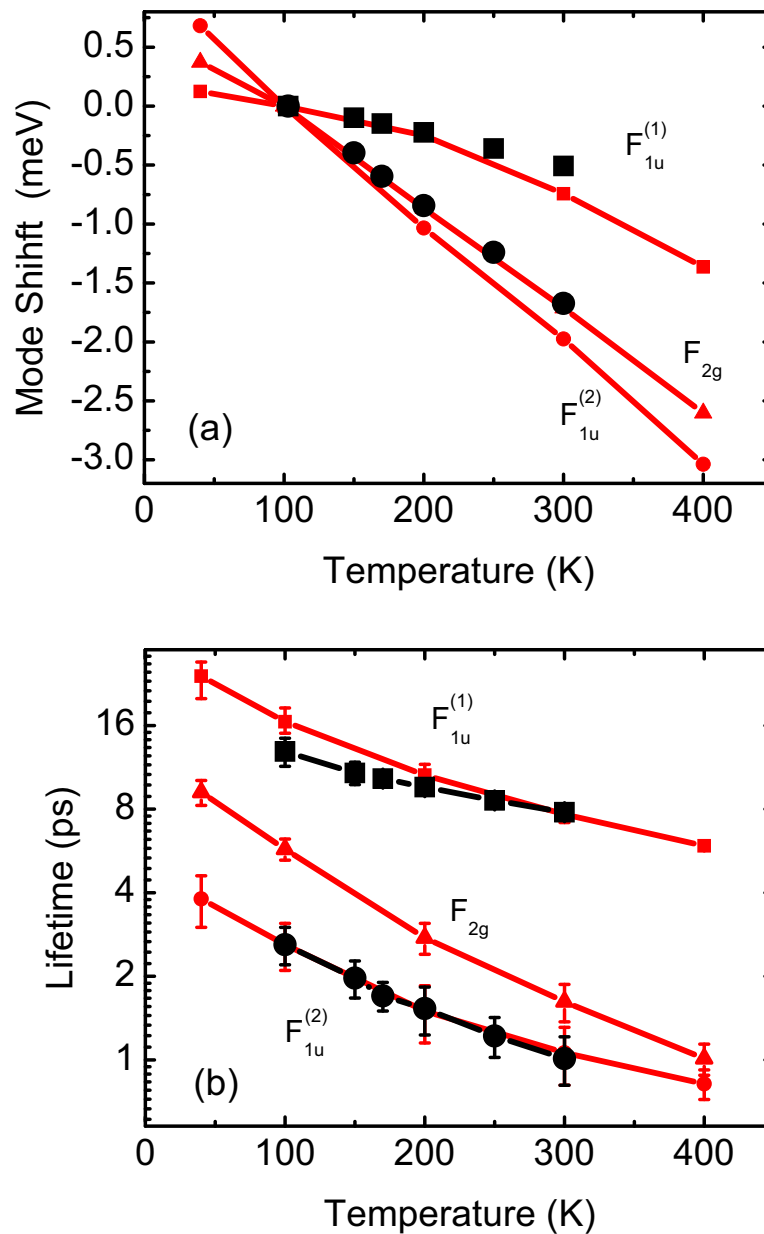


Figure 6.9: (a) Temperature dependent frequency shifts of the Ag-dominated $F_{1u}^{(1)}$ mode and the O-dominated F_{2g} and $F_{1u}^{(2)}$ modes from FT-IR (black), compared with the MD simulated peaks (red) such as in Fig. 6.8. (b) The lifetimes of the corresponding modes at temperatures from 40 to 400 K, from FT-IR (black) and the MD simulated peaks (red).

6.4 Anharmonic Perturbation Theory

6.4.1 Computational Methodology

Cubic anharmonicity gives rise to three-phonon processes, which are an important mechanism of phonon-phonon interactions. The strengths of the three-phonon processes depend on two elements – the cubic anharmonicity tensor that gives the coupling strengths between three phonons, and the kinematical processes described by the two-phonon density of states (TDOS). [2, 48, 142]

From Ipatova, *et al.* [46], an anharmonic tensor element for a process with the initial phonon mode j at the Γ -point and s phonons is

$$V(j; \vec{q}_1 j_1; \dots; \vec{q}_{s-1} j_{s-1}) = \frac{1}{2s!} \left(\frac{\hbar}{2N} \right)^{\frac{s}{2}} N \Delta(\vec{q} + \vec{q}_1 + \dots + \vec{q}_{s-1}) \times [\omega_1 \dots \omega_{s-1}]^{\frac{1}{2}} C(j; \vec{q}_1 j_1; \dots; \vec{q}_{s-1} j_{s-1}) \quad (6.2)$$

where the phonon modes $\{\vec{q}_i j_i\}$ have quasi-harmonic frequencies $\{\omega_i\}$ and occupancies $\{n_i\}$. The $C(\cdot)$'s are expected to be slowly-varying functions of their arguments. [143] We assume the term $C(j; \vec{q}_1 j_1; \dots; \vec{q}_{s-1} j_{s-1})$ is a constant for the initial phonon j , and use it as a parameter when fitting to trends from MD or experiment. Although $C(j; \vec{q}_1 j_1; \vec{q}_2 j_2)$ changes with j_1 and j_2 , an average over modes,

$$\langle C(\cdot) \rangle = \frac{\sum_{1,2} C(j; \vec{q}_1 j_1; \vec{q}_2 j_2)}{\sum_{1,2} 1} \quad (6.3)$$

is found by fitting to experimental or simulational results, where 1, 2 under the summation symbol represent $\vec{q}_i j_i$. We define the cubic fitting parameter as

$$C_j^{(3)} = \langle C(j; \vec{q}_1 j_1; \vec{q}_2 j_2) \rangle \quad (6.4)$$

The second key element of perturbation theory is that interacting phonons satisfy the kinematical conditions of conservation of energy and momentum. This condition is averaged over all phonons with the two-phonon density of states

(TDOS), defined as

$$\begin{aligned}
D(\omega) &= \sum_{\vec{q}_1, j_1} \sum_{\vec{q}_2, j_2} D(\omega, \omega_1, \omega_2) \\
&= \frac{1}{N} \sum_{\vec{q}_1, j_1} \sum_{\vec{q}_2, j_2} \Delta(\vec{q}_1 + \vec{q}_2) \left[(n_1 + n_2 + 1) \delta(\omega - \omega_1 - \omega_2) \right. \\
&\quad \left. + 2(n_1 - n_2) \delta(\omega + \omega_1 - \omega_2) \right] \tag{6.5}
\end{aligned}$$

The first and second terms in square brackets are from down-conversion and up-conversion scattering processes, respectively.

The strength of the cubic phonon anharmonicity can be quantified by the quality factor Q , related to the phonon lifetime as the number of the vibrational periods for the energy to decay to a factor of $1/e$, and $Q = \omega/2\Gamma$, where 2Γ is the linewidth of the phonon peak. Considering Eqs. (6.2) to (6.5), the phonon linewidth is related to the TDOS, $D(\omega)$, weighted by the coupling strength. [131, 143] To leading order, the inverse of the quality factor can be expressed as a function of the TDOS

$$\frac{1}{Q_j} = \frac{\pi\hbar}{32} |C_j^{(3)}|^2 \sum_{\vec{q}_1, j_1} \sum_{\vec{q}_2, j_2} \omega_1 \omega_2 D(\omega, \omega_1, \omega_2) \tag{6.6}$$

The TDOS at various temperatures was calculated from the kinematics of all three-phonon processes, sampling the phonon dispersions with a $16 \times 16 \times 16$ q -point grid for good convergence. The Q from MD simulations were used to approximate the anharmonicity of the phonon modes of different energies, and obtain the the coupling strengths $|C_j^{(3)}|^2$ for the different modes.

6.4.2 Results

Fig. 6.10(a) shows calculated phonon dispersion curves of Ag_2O with the cuprite structure along high-symmetry directions. From these, the TDOS spectra, $D(\omega)$, were obtained at different temperatures, presented in Fig. 6.10(b) for 40 and 400 K. At low temperatures there are two small peaks in the TDOS centered at 15 and

65 meV. Our calculation showed that the peak at 15 meV is from the decay processes of one Ag-dominated mode into two with lower frequencies, i.e., $\text{Ag} \mapsto \text{Ag} + \text{Ag}$. The peak at 65 meV originates from spontaneous decay of one O-dominated mode into another O-dominated mode of lower frequency and one Ag-dominated mode.

At high temperatures there are more down-conversion processes, but an even greater change in up-conversion processes. Figure 6.10(b) shows how the strong down-conversion peaks at low temperatures grow approximately linearly with temperature, following the thermal population of phonon modes involved in the interactions. Near the peak at 65 meV, one up-conversion band centered at 50 meV is also strong. This band comprises scattering channels in which one O-dominated mode is combined with a Ag-dominated mode to form a higher frequency O-dominated mode, i.e., $\text{O} \mapsto \text{O} - \text{Ag}$. At the low energy side, there is another band below 15 meV from two types of up-conversion processes. One is from Ag-dominated modes alone, i.e., $\text{Ag} \mapsto \text{Ag} - \text{Ag}$. The other involves two O-dominated modes, i.e., $\text{Ag} \mapsto \text{O} - \text{O}$, owing to the increased number of higher energy O-dominated modes that can participate in these processes at higher temperatures.

Figure 6.11 shows the inverse of quality factors, $1/Q$, of the $F_{1u}^{(1)}$, F_{2g} , $F_{1u}^{(2)}$ and A_{2u} phonon modes from FT-IR and MD calculations, together with the best theoretical fits with Eq. (6.6). These modes are near the centers of main features of the phonon DOS shown in Fig. 6.2, i.e., the peaks 1, 2, 3 and the gap in between, respectively, and are useful for understanding the overall anharmonicity. As shown in Fig. 6.11, at higher temperatures the quality factors decrease substantially. At 400 K, the $F_{1u}^{(1)}$, F_{2g} , $F_{1u}^{(2)}$ modes have low Q values from 12 to 15, but the A_{2u} mode has a much larger value of 26. With a single parameter $|C_j^{(3)}|^2$ for each mode, good fittings to the quality factors are obtained. The fitting curves and the corresponding values of the parameters $|C_j^{(3)}|^2$ are presented in Fig. 6.11. The $|C_j^{(3)}|^2$ values do not vary much among different modes, so the typical assumption of a slowly varying $C(\cdot)$ seems reasonable.

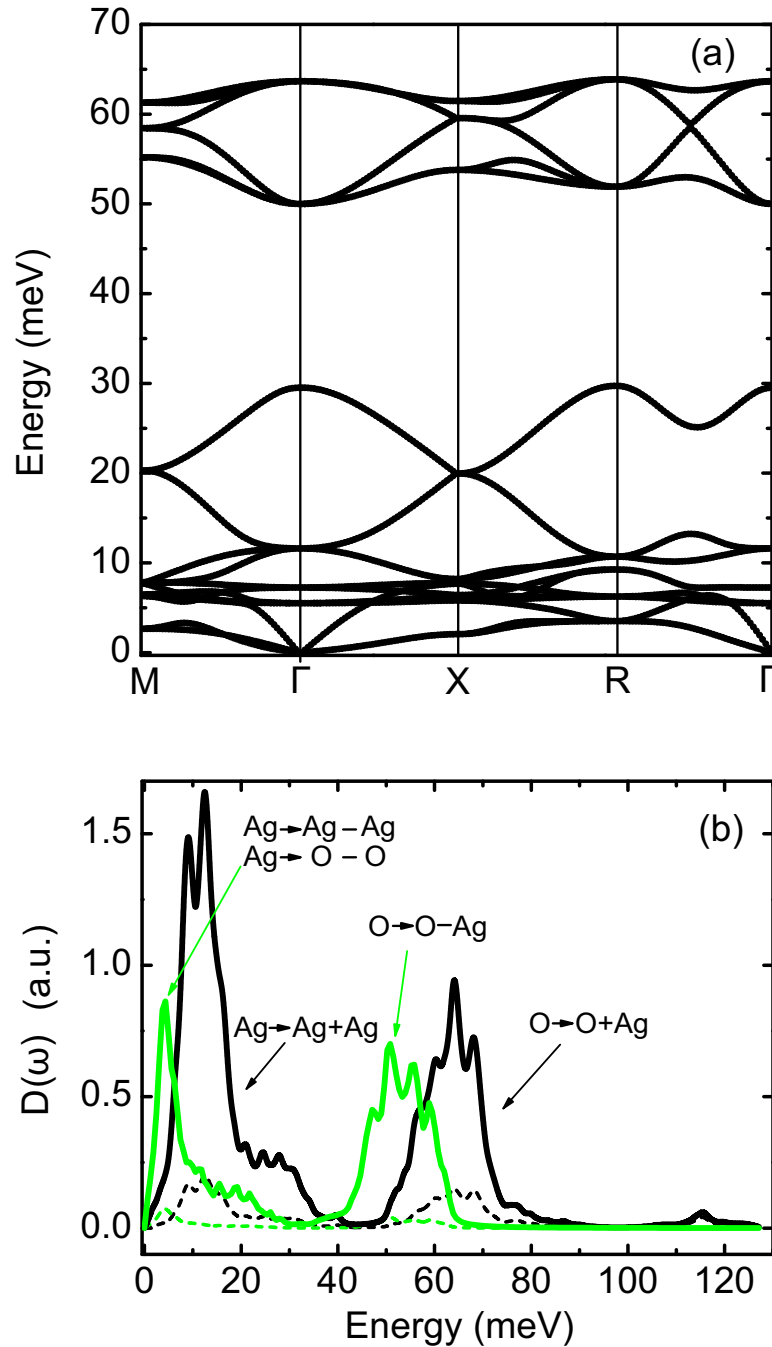


Figure 6.10: (a) Calculated phonon dispersion along high-symmetry directions of Ag_2O with the cuprite structure. Γ (0, 0, 0), M (0.5, 0.5, 0), X (0.5, 0, 0), R (0.5, 0.5, 0.5). (b) The TDOS spectra, $D(\omega)$, at 40 K (dashed) and 400 K (solid). The down-conversion and up-conversion contributions are presented separately as black and green curves, respectively.

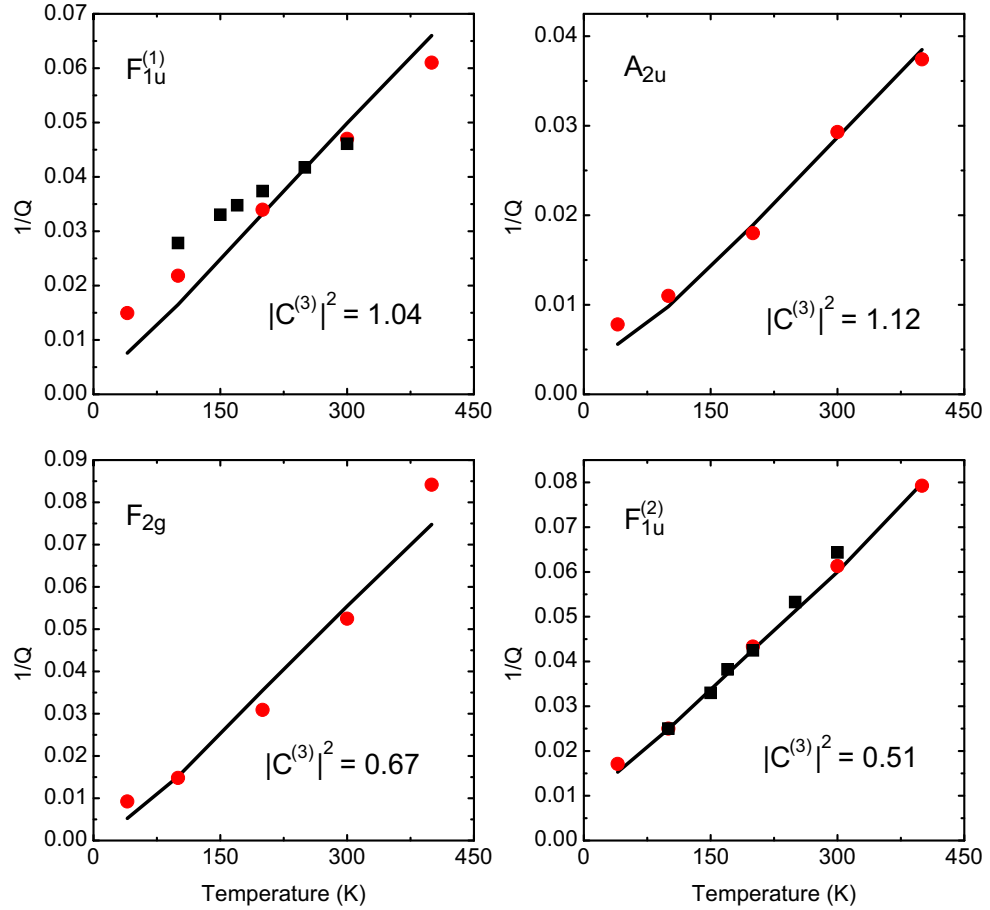


Figure 6.11: Temperature dependence of the inverse of the quality factors $1/Q$ for the $F_{1u}^{(1)}$, A_{2u} , F_{2g} and $F_{1u}^{(2)}$ phonon modes from FT-IR (black squares), MD calculations (red circles) and the theoretical fittings with a full calculation of the TDOS. The unit of the fitting parameter $|C_j^{(3)}|^2$ is 10^{-1} eV^{-1} .

6.5 Discussion

6.5.1 Quasiharmonic Approximation

In the quasiharmonic approximation (QHA), a mode Grüneisen parameter γ_j is defined as the ratio of the fractional change of the mode frequency ω_j to the fractional change of volume V , at constant temperature, $\gamma_j = -\frac{\partial(\ln \omega_j)}{\partial(\ln V)}$. The usual trend is for phonons to soften with lattice expansion, increasing the phonon entropy and

stabilizing the expanded lattice at elevated temperatures. A negative Grüneisen parameter is therefore expected for the special phonon modes associated with NTE, such as RUMs. If all the anharmonicity of Ag_2O with the cuprite structure is attributed to this volume effect, however, the values of Grüneisen parameters are approximately -9 for the high energy modes at peaks 2 and 3 of the phonon DOS, and -20 for the infrared-active F_{1u} mode. These anomalous values may indicate a problem with the QHA. The QHA method also significantly underestimates the NTE, and misses the behavior at temperatures above 250 K.

To separate the effects of quasiharmonicity and explicit anharmonicity, the mode frequency $\omega_j = \omega_j(V, T)$ is expressed as a function of volume and temperature

$$\left(\frac{\partial \ln \omega_j}{\partial T}\right)_P = -\gamma_j \beta + \left(\frac{\partial \ln \omega_j}{\partial T}\right)_V \quad (6.7)$$

where j is the phonon mode index, β is the volume thermal expansivity and γ_j is the mode Grüneisen parameter. The left-hand side is the temperature-dependent frequency shift at constant pressure, and includes contributions from both quasiharmonicity and explicit anharmonicity. The first term on the right-hand side, the isothermal frequency shift as a function of pressure, is the quasiharmonic contribution to the frequency shift. The second term on the right is the pure temperature contribution to the frequency shift from the explicit anharmonicity. From the difference of the isobaric and isothermal frequency shifts, the explicit anharmonicity can be determined.

In a molecular dynamics simulation, the quasiharmonic contribution can be evaluated explicitly by turning off the temperature-dependent anharmonicity. In principle, this method is equivalent to the QHA method implemented with self-consistent lattice dynamics, [119] and in practice we have found this to be true. For example, we performed simulations at 40 K for volumes characteristic of 400 K, which produced a pressure of 0.45 GPa. This calculation therefore removed the temperature effect while preserving the quasiharmonic volume effect at 400 K. The corresponding phonon DOS curves from MD calculations are shown in Fig. 6.12.

By comparing the phonon spectrum of a simulation at 40 K and 0.45 GPa with a simulation at 400 K, the pure temperature dependence is identified. From the spectra of Fig. 6.12, it is found that the explicit anharmonicity dominates the softening and broadening of the phonon spectra. All features in the phonon spectra with the QHA showed little change with temperature, except for small stiffenings at high energies.

As seen in Fig. 6.12 and in Fig. 6.8, the giant negative Grüneisen parameters are inconsistent with the results of MD simulations. The volume change alone does not affect much the phonon lifetimes or frequency shifts. All features in the phonon spectra generated with the MD-implemented QHA showed little change except for small stiffening about 0.6 meV at high energies, in agreement with the recent lattice dynamics QHA calculations. [126]

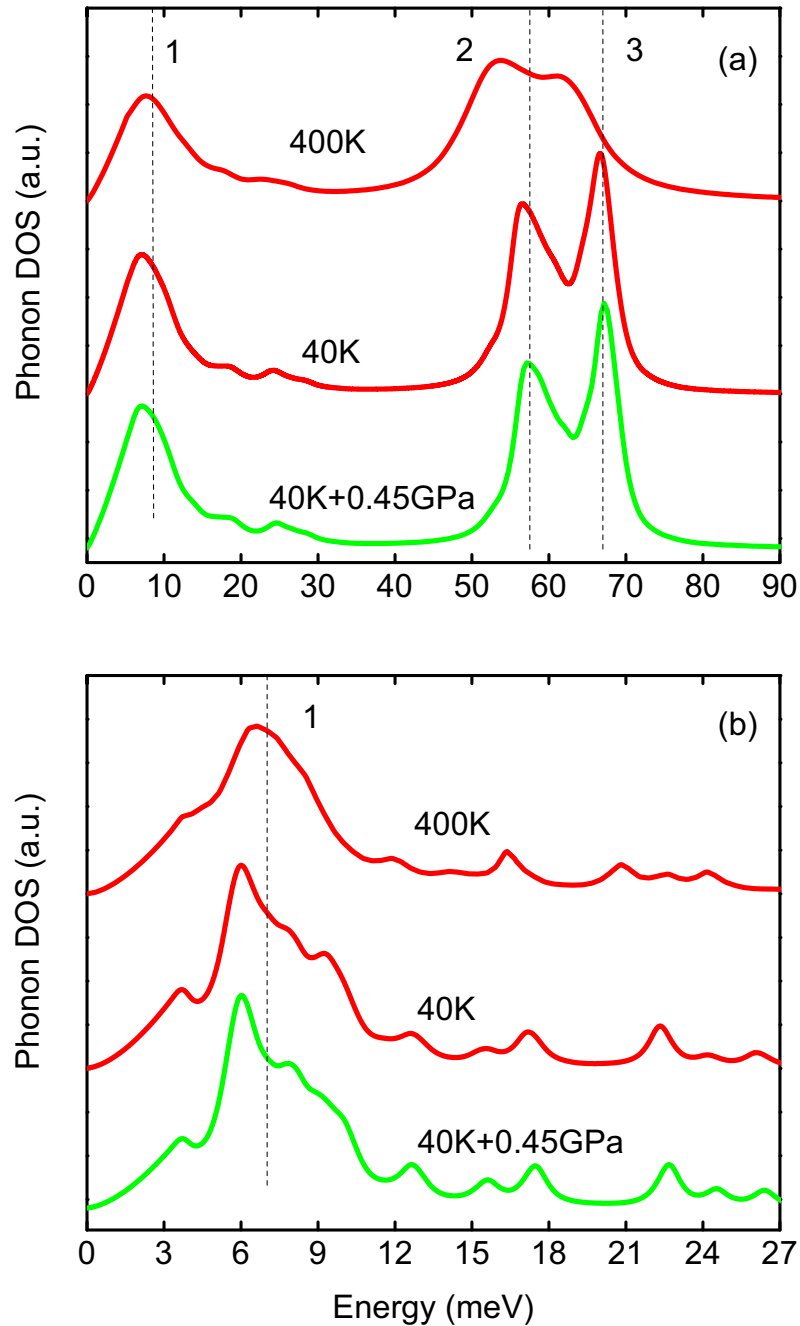


Figure 6.12: Neutron weighted phonon DOS of Ag₂O with the cuprite structure from MD simulations. The green spectrum is the MD simulated phonon DOS at 40K and 0.45 GPa. Vertical dashed lines are aligned to the major peak centers at 40K and labeled by numbers. The incident energy was 100 meV for panel (a), and 30 meV for panel (b). The spectra were convoluted with the resolution function characteristic of ARCS for the different energies of the incident neutron beam.

6.5.2 Negative Thermal Expansion

Our eigenvector analysis of phonon modes showed that the three low-energy Ag-dominated F_{2u} , E_u and F_{1u} modes correspond to two distinct types of vibrations. The F_{2u} mode involves rigid rotations of Ag_4O tetrahedra, and could be considered as RUM. The E_u mode involves the shearing of Ag_4O units by changing the Ag-O-Ag bond angles. The F_{1u} mode measured by infrared spectrometry also shears the Ag_4O units, and includes some displacements of O atoms. Shearing the tetrahedra was shown to reduce the average vertex-vertex distance [134, 144] and contribute to the NTE.

In the cuprite structure, the modes associated with the rigid rotations and the distortions of the Ag_4O tetrahedra have similar energies below 10 meV. They are equally favorable thermodynamically, and both would be active at very low temperature. As a consequence, there is simultaneously a large deformation of Ag_4O units and a strong contraction of the Ag-Ag shell, as observed experimentally and computationally at low temperatures. The large thermal distortions of the Ag_4O tetrahedra involve the Ag atoms at the vertices, and their large mass causes these distortions to occur at low frequencies. Polyhedral units in most other NTE materials are bridged by the lightweight atoms, such as O and C-N, so the polyhedra are distorted at significantly higher energies (usually above 40 meV), and may not distort at lower temperatures.

It is a thermodynamic requirement that the NTE of Fig. 6.7 must go to zero at $T = 0$, but the intervening phase transition at 40 K impedes this measurement. Nevertheless, the steep slope of the lattice parameter with temperature is consistent with the occupancy of phonon modes of 10 meV energy, suggesting that the QHA model of NTE involves the correct modes, such as the F_{2u} mode (which is a RUM). These low-energy modes are dominated by motions of the Ag atoms. This explanation based on the QHA is qualitatively correct, but anharmonic interactions are large enough to cause the QHA to underestimate the NTE by a factor of two.

6.5.3 Explicit Anharmonicity

At temperatures above 250 K, there is a second part of the NTE behavior that is beyond the predictions of quasiharmonic theory. This NTE above 250 K is predicted accurately by the ab-initio MD calculations, so it is evidently a consequence of phonon anharmonicity. The temperature-dependence of this NTE behavior follows the Planck occupancy factor for phonon modes above 50 meV, corresponding to the O-dominated band of optical frequencies. In the QHA these modes above 50 meV do not contribute to the NTE. These modes are highly anharmonic, however, as shown by their large broadenings and shifts.

For cubic anharmonicity, the two-phonon DOS (TDOS) is the spectral quantity parameterizing the number of phonon-phonon interaction channels available to a phonon. For Ag_2O with the cuprite structure, the peaks in the TDOS overlap well with the peaks in the phonon DOS. Most of the phonons therefore have many possible interactions with other phonons, which contributes to the large anharmonicity of Ag_2O with the cuprite structure, and small Q (short lifetimes). Although the Q values of most phonon modes in Ag_2O with the cuprite structure are small and similar, the origins of these lifetime broadenings are intrinsically different. For peak 2 of the phonon DOS, the anharmonicity is largely from the up-conversion processes: $\text{O} \mapsto \text{O} - \text{Ag}$, while for peak 3 it is from the down-conversion processes: $\text{O} \mapsto \text{O} + \text{Ag}$. The anharmonicity of peak 1 is more complicated. It involves both up-conversion and down-conversion processes of Ag-dominated modes. The TDOS also shows why the A_{2u} mode has a larger Q than other modes. Figure 6.10(b) shows that the A_{2u} mode lies in the trough of the TDOS where there are only a few phonon decay channels.

Owing to explicit anharmonicity from phonon-phonon interactions, the thermodynamic properties of Ag_2O with the cuprite structure cannot be understood as a sum of contributions from independent normal modes. The frequency of an anharmonic phonon depends on the level of excitation of other modes. At high temperatures, large vibrational amplitudes increase the anharmonic coupling of

modes, and this increases the correlations between the motions of the Ag and O atoms, as shown by perturbation theory. Couplings in perturbation theory have phase coherence, so the coupling between Ag- and O-dominated modes at higher energies, as seen in the peak of the TDOS, causes correlations between the motions of Ag and O atoms. The ab-initio MD simulations show that anharmonic interactions allow the structure to become more compact with increasing vibrational amplitude. The mutual motions of the O and Ag atoms cause higher density as the atoms fill space more effectively. The large difference in atomic radii of Ag and O may contribute to this effect. Perhaps it also facilitates the irreversible changes in Ag₂O at temperatures above 500 K, but this requires further investigation. For cuprite Cu₂O, which has less of a difference in atomic radii, the thermal expansion is much less anomalous.

6.6 Conclusions

Phonon densities of states of Ag₂O with the cuprite structure at temperatures from 40 to 400 K were measured by inelastic neutron scattering spectrometry. The infrared spectra of phonon modes were also obtained at temperatures from 100 to 300 K. Large anharmonicity was found from both the shifts and broadenings of peaks in the phonon spectra. A normal mode analysis identified the rigid unit modes and the bending modes of the Ag₄O tetrahedra that play key roles in the negative thermal expansion (NTE) at low temperatures. Some of the NTE can be understood by quasiharmonic theory, but this approach is semiquantitative, and limited to temperatures below 250 K.

First principles MD calculations were performed at several temperatures. These calculations accurately accounted for the NTE and local dynamics of Ag₂O with the cuprite structure, such as the contraction of the Ag-Ag shell and the large distortion of the Ag₄O tetrahedra. The phonon DOS obtained from a Fourier-transformed velocity autocorrelation method showed large anharmonic effects in Ag₂O, in excellent agreement with the experimental data. A second part of the NTE

at temperatures above 250 K is due largely to the anharmonicity of phonon-phonon interactions and is not predicted with volume dependent quasiharmonicity.

Phonon perturbation theory with the cubic anharmonicity helped explain the effects of phonon kinematics on phonon anharmonicity of Ag_2O with the cuprite structure. The phonon interaction channels for three-phonon processes are given by the TDOS, weighted approximately by the phonon coupling strength. The phonons that are most broadened are those with energies that lie on peaks in the TDOS. The temperature-dependence of the quality factors Q of individual phonon modes measured by infrared spectrometry were explained well by anharmonic perturbation theory. Perturbation theory also showed strong interactions between the Ag-dominated modes and the O-dominated modes in both up-conversion and down-conversion processes. In particular, the strong interactions of O-dominated modes with Ag-dominated modes causes the second stage of NTE at temperatures above 250 K.

Chapter 7

Conclusions

7.1 Summary

Non-harmonic phonon-phonon interaction in solids is a central but poorly understood topic in condensed matter physics. For example, thermodynamic equilibrium cannot be achieved with non-interacting harmonic phonons. Finite thermal conductivity also requires phonon-phonon interactions. We obtained the data of anharmonic effects in metal oxides (rutile TiO_2 , cuprite Ag_2O , e.g.) from Raman spectroscopy, FTIR spectroscopy and inelastic neutron scattering. The focus of this thesis is more on the models and algorithms we developed, which successfully reproduced the vibrational information on anharmonic lattice dynamics. In particular, we developed the Fourier transformed velocity autocorrelation method to reproduce the anharmonic phonon energy spectra in solids, and we also used perturbation theory to investigate microscopically the phonon interaction channels and interaction intensities in anharmonic processes.

In Chapter 1, fundamental theories of lattice dynamics were reviewed. The focus was on anharmonic lattice dynamics and phonon-phonon interactions, upon which most of work presented in this thesis is based. In particular, the Green's function method for phonon-phonon interactions was derived in detail, and the mathematical expressions for anharmonic phonon energy broadening and shift were proved.

In Chapter 2, the experimental techniques performed in this thesis were dis-

cussed. For Raman scattering, the quantum theory and selection rules based on the group theoretical analysis were discussed in detail. For time-of-flight inelastic neutron scattering, basic principles of neutron scattering were reviewed, and the experimental setup and data reduction procedures were introduced.

In Chapter 3, the main computational methods and algorithms that we used in this study were discussed. This chapter started with a brief review of modern density functional theory, and molecular dynamics simulations. The focus was on the methods for phonon calculations, especially the Fourier-transformed velocity autocorrelation method and the anharmonic phonon-phonon interaction analysis method.

In Chapter 4, we considered the phonon anharmonicity of rutile TiO_2 . Raman spectra of rutile TiO_2 were measured at temperatures from 100 K to 1150 K. A dominant role of phonon-phonon kinematics on phonon shifts and broadenings was reported. Force field MD calculations with the Fourier-transformed velocity autocorrelation method were also used to perform a quantitative study of anharmonic effects, successfully accounting for the anomalous phonon anharmonicity of the B_{1g} mode.

In Chapter 5, we considered the phonon anharmonicity of rutile SnO_2 . Raman spectra of rutile SnO_2 were measured at temperatures from 83 to 873 K. The pure anharmonicity from phonon-phonon interactions was found to be large and comparable to the quasiharmonicity. The broadening of the B_{2g} mode with temperature showed an unusual concave downwards curvature. This curvature is caused by a change with temperature in the number of down-conversion decay channels, originating with the wide band gap in the phonon dispersions.

In Chapter 6, we considered the phonon anharmonicity of Ag_2O with the cuprite structure. Inelastic neutron scattering measurements on Ag_2O were performed at temperatures from 40 to 400 K, and Fourier transform far-infrared spectra were measured from 100 to 300 K. The measured phonon densities of states and the infrared spectra showed unusually large energy shifts with temperature, and large linewidth broadenings. First principles molecular dynamics (MD) calculations

were performed at various temperatures, successfully accounting for the negative thermal expansion (NTE) and local dynamics. Using the Fourier-transformed velocity autocorrelation method, the MD calculations reproduced the large anharmonic effects of Ag_2O , and were in excellent agreement with the neutron scattering data. Strong anharmonic effects were found for both phonons and for the NTE. The lifetime broadenings of Ag_2O were explained by anharmonic perturbation theory, which showed rich interactions between the Ag-dominated modes and the O-dominated modes in both up- and down-conversion processes.

7.2 Future Work

The study of phonon anharmonicity and phonon-phonon interaction is a difficult but exciting field. It is difficult because we must consider how phonons interact with other phonons or with other excitations – an example of a notorious many-body interaction problem. In comparison, our understanding today about the vibrational thermodynamics of materials at low temperatures is broad and deep because it is based on the harmonic model in which phonons are independent, avoiding issues of anharmonic lattice dynamics.

Phonon anharmonicity is an exciting topic because of its fundamental importance and broad applications. With the development of modern experimental techniques and the progress of the anharmonic phonon theories and computational methodologies, we are in a good position to study the relation between the phonon anharmonicity and many important thermodynamic properties of materials, for example, thermodynamic phase stability, thermal expansion and thermal conductivity. Nevertheless, this subject needs new theoretical models and computational algorithms.

I. Thermodynamic Phase Stability

The ability to predict phase equilibria and structural transformations in solids

under pressure and temperature is of great importance to both science and industry. The failure of the harmonic theory mostly arises from the assumption of independent phonons, which becomes increasingly inaccurate at high temperatures. For example, although rutile is the most common and stable crystal structure of TiO_2 , most of the phonon calculations do not agree well with experimental results. For example, the anatase phase was calculated to be more stable than the rutile phase [145]. Moreover, a recent study based on the quasiharmonic approximation found the low energy modes of rutile to be very soft, and some of them decrease to zero frequency upon a 0.5% lattice expansion [71]. This suggests an instability of rutile upon heating. With inelastic neutron scattering data from ARCS, and very recent first principles MD calculations, we found double well potentials with a depth of about 2.5 meV for the modes with negative frequencies upon lattice expansion. This is a classic "Landau potential". Using MD simulation at finite temperatures, the thermal energy of anharmonic modes was found to be considerably larger than the shallow depth of the double wells, ensuring no symmetry break and structure instability. Moreover, at elevated temperatures, it was found that these anharmonic modes explore a potential surface that can be approximated as a quartic form, which accounts for the anomalously large thermal stiffening. This work is coming along well, and is a good example showing how the phonon anharmonicity determines the phase stability.

II. Thermal Expansion

Thermal expansion is another anharmonic effect. Recently, negative thermal expansion (NTE) has been discovered and its potential applications in engineering are attracting much interest. However, most studies about thermal expansion are based on harmonic theory or quasiharmonic theory with non-interacting phonons. In some cases, a harmonic free energy optimization leads to a good estimation of thermal expansivity, but there are many examples showing that the anharmonic contribution is significant. The NTE of Ag_2O presented in this thesis, for example,

is an interesting one [146]. At high temperatures, large vibrational amplitudes increase the anharmonic coupling of modes, and this tends to increase the correlations between the motions of the Ag and O atoms. The ab-initio MD simulations show that anharmonic interactions allow the structure to become more compact with increasing vibrational amplitude. Although we can understand this effect at a qualitative level, a quantitative model is desirable to describe this interaction. Because couplings in perturbation theory have phase coherence, the coupling between Ag- and O-dominated modes at higher energies, as seen in the peak of the TDOS, is expected to cause correlations between the motions of Ag and O atoms, and the study of this correlation could be an interesting direction.

III. Thermal Conductivity

In many cases, harmonic lattice dynamics can still be regarded as the leading order approximation, but such a model predicts an infinite phonon thermal conductivity for a perfect crystal. To obtain a finite thermal conductivity, three-phonon and higher anharmonic processes must be considered. Thermal conductivity can be predicted with the Green-Kubo method by using the heat current generated by MD and taking the autocorrelation [41,42]. The calculation is a little more complex than the velocity autocorrelation method, but the computational logic and structure are exactly the same. Our code should be easily extended to this calculation, which converges fast and is quite robust and accurate.

The Callaway method is also popular [147]. It computes the phonon lifetime directly, but it also requires the phonon group velocity and energy/momentum conservation to be calculated explicitly. Actually, several important components of this method were already developed in the work presented in this thesis. This method has its own benefit because it can investigate thermal conduction in a microscopic manner, i.e., contributions from different modes can be clearly identified. The result from this method can also compare directly with the anharmonic data obtained in real experiments. For example, using inelastic neutron scattering, we

can directly obtain phonon dispersions with lifetime broadening. In our recent neutron experiment, we got such phonon data on a single crystal of silicon (Si). These new data could be an important testbed to develop and implement this method.

IV. Other Theoretical Methods

With the MD calculations and the velocity autocorrelation analysis being well developed, we can incorporate the MD method with the self-consistent lattice dynamics model described in Chapter 1. These methods are promising in the study of anharmonic thermal stability, for example. The benefit of a self-consistent lattice dynamics calculation is that it is based on a lattice dynamics model, and therefore once the parameters in this model are known, it could be more efficient and simpler to get the anharmonic phonon dispersions with very high signal to noise ratio. It is also interesting to compare the self-consistent lattice dynamics model with pure MD results because using a mean field harmonic model could be questionable under very anharmonic conditions.

Another interesting approach might be a frozen "phonon-phonon interaction" method. It is based on the direct frozen phonon method, but we can add one more loop above it. This additional loop would sample different atomic displacements of different frozen phonons and assign with them appropriate amplitudes. In this way, we can still take advantage of the well-established frozen phonon method, but we may also generate an ensemble to simulate the phonon-phonon interactions and their high-dimensional potential surface. The key to this method is that instead of assigning displacements randomly, we should build the ensemble according to the phonon eigenvectors and the target temperature. A MD calculation essentially provides a dynamic phonon-phonon interactions atmosphere, while in this method, we are interested in how to freeze these interactions in a controllable manner, and to extract the potential surface.

Last but not least, the evaluation of anharmonic entropy is quite an interesting

and challenging topic. As we presented before, up to now the vibrational entropy is exclusively based on the harmonic or quasiharmonic approximation, the validity is under question for a strong anharmonic case. This approximation should fail for a highly anharmonic material. Although it is more theoretical, the understanding of the anharmonic vibrational entropy is crucial for advancing the basic theory of lattice dynamics. In this case, approaches with the harmonic partition function may be unreliable, and one possible way is to start from the original definition of entropy, i.e., we can sample the phase space from a MD simulation, and try to obtain the phase volume from those trajectories. Such an approach may include problems of chaotic dynamics, but rich contributions could come from this.

Appendix A

The evaluation of the 2nd order Feynman diagram of phonon-phonon interactions

Following Section 1.6, we can simply translate the 2nd order diagram by replacing the lines and vertices with the corresponding free phonon propagator and anharmonic interaction terms. Because there are two lines connected with two vertices, this gives Eq. A.1a. Here, $\omega_n = \frac{2n\pi}{\beta\hbar}$ is the discrete set of energies by Fourier transforming the complex time τ of the self energy Σ^* , as defined previously for the temperature Green's function; similarly, ω_{n_1} and ω_{n_2} are the corresponding energy sets for the free propagators in the energy space, and $\omega_n = \omega_{n_1} + \omega_{n_2}$. ω_1 and ω_2 are harmonic or quasiharmonic phonon frequencies of phonon mode q , as defined in Section 1.6 for the free phonon propagator.

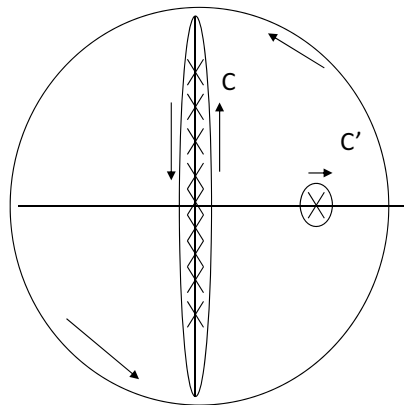


Figure A.1: Contour of evaluation for energy sums

The complete mathematical proof is provided here, followed by the notes for some important and non-obvious steps

$$\Sigma_{\tilde{q}ss'}^*(\omega_n) \quad (\text{A.1a})$$

$$= \frac{18}{\beta\hbar^3} \sum_{q_1, q_2} \sum_{n_1} V^{(3)}(-q, q_1, q_2) V^{(3)}(q', -q_1, -q_2) g^0(q_1, \omega_{n_1}) g^0(q_2, \omega_{n_2})$$

$$= \frac{18}{\hbar^2} \sum_{\omega_1, \omega_2} 4\omega_1\omega_2 V^{(3)}(\dots) V^{(3)}(\dots) \times \quad (\text{A.1b})$$

$$\frac{1}{\beta\hbar} \sum_{n_1} \frac{1}{(\omega_1 - i\omega_{n_1})(\omega_1 + i\omega_{n_1})(\omega_2 - i(\omega_n - \omega_{n_1}))(\omega_2 + i(\omega_n - \omega_{n_1}))}$$

$$= \frac{18}{\hbar^2} \sum_{\omega_1, \omega_2} \frac{4\omega_1\omega_2}{2\pi i} V^{(3)}(\dots) V^{(3)}(\dots) \times \quad (\text{A.1c})$$

$$\int_C \frac{dz}{e^{\beta\hbar z} - 1} \frac{1}{(z - \omega_1)(z + \omega_1)(z + \omega_2 - i\omega_n)(z - \omega_2 - i\omega_n)}$$

$$= \frac{18}{\hbar^2} \sum_{\omega_1, \omega_2} 4\omega_1\omega_2 V^{(3)}(\dots) V^{(3)}(\dots) \times \quad (\text{A.1d})$$

$$\left(\frac{1}{e^{\beta\hbar\omega_1} - 1} \frac{-1}{2\omega_1(\omega_1 + \omega_2 - i\omega_n)(\omega_1 - \omega_2 - i\omega_n)} + \text{similar other 3 terms} \right)$$

$$= \frac{18}{\hbar^2} \sum_{\omega_1, \omega_2} 4\omega_1\omega_2 V^{(3)}(\dots) V^{(3)}(\dots) \left(\frac{n_1}{2\omega_1(\omega_1 + \omega_2 - i\omega_n)(\omega_2 - \omega_1 + i\omega_n)} \right) \quad (\text{A.1e})$$

$$+ \frac{n_1 + 1}{2\omega_1(\omega_2 - \omega_1 - i\omega_n)(\omega_1 + \omega_2 + i\omega_n)} + \frac{n_2}{2\omega_2(\omega_1 - \omega_2 - i\omega_n)(\omega_1 + \omega_2 + i\omega_n)}$$

$$+ \frac{n_2 + 1}{2\omega_2(\omega_1 + \omega_2 - i\omega_n)(\omega_1 - \omega_2 + i\omega_n)} \Bigg)$$

$$= \frac{18}{\hbar^2} \sum_{\omega_1, \omega_2} V^{(3)}(\dots) V^{(3)}(\dots) \left(\frac{n_1 + n_2 + 1}{\omega_1 + \omega_2 - i\omega_n} + \frac{n_2 - n_1}{\omega_1 - \omega_2 + i\omega_n} \right) \quad (\text{A.1f})$$

$$+ \frac{n_1 + n_2 + 1}{\omega_1 + \omega_2 + i\omega_n} + \frac{n_2 - n_1}{\omega_1 - \omega_2 - i\omega_n} \Bigg)$$

Note:

(1) The prefactor 18 comes from the fact that this diagram has 3 degrees of freedom in each vertex and there are hence $3 \times 3 \times 2 = 18$ equivalent diagrams.

(2) From Eq. A.1b to Eq. A.1c, we are using the following equality which is

typical of evaluating summations of a series of excitations in many body physics:

$$\sum_n \frac{1}{i\omega_n - x} = \frac{\beta\hbar}{2\pi i} \int_C \frac{dz}{e^{\beta\hbar z} - 1} \frac{1}{z - x} \quad (\text{A.2})$$

Here the integral is along a contour C encircling the imaginary axis in the positive sense, as shown in Fig. A.1. Notice that the integrand has poles at $z = 2n\pi i/\beta\hbar = i\omega_n$, each with unit residue, then Cauchy's Residue theorem directly gives the Eq. A.2. It is evident that the choice of the integrand is not unique mathematically; But physically, $(e^{\beta\hbar z} - 1)^{-1}$ is preferred because it is connected with the quantum occupation number explicitly and we will see its advantages shortly.

(3) From Eq. A.1c to Eq. A.1d, we are evaluating the integral. As illustrated in Fig. A.1, we deform the contour C to C' , which extends to infinity and only includes a simple pole at $z = x$. Using Residue theorem again, we simply obtain the result

$$\sum_n \frac{1}{i\omega_n - x} = \frac{-\beta\hbar}{e^{\beta\hbar x} - 1} \quad (\text{A.3})$$

(4) From Eq. A.1d to Eq. A.1e, notice that $(e^{\beta\hbar\omega} - 1)^{-1}$ is the phonon occupancy number n , and importantly, $n(i\omega_n + \omega) = n(\omega)$ since $e^{i\beta\hbar\omega_n} = 1$, which amazingly guarantees the original physical meaning of the occupancy number and gives Eq. A.1e.

As discussed in the end of Sec. 1.5.2, though the temperature Green's function is convenient to perform the mathematical calculation, it cannot be directly related to the frequencies and lifetimes of excited states at finite temperature. Those quantities are contained in the real-time retarded Green's function G_R , and we need an analytical continuation to make a transformation. As discussed, by comparing the generating function of $g(\omega_n)$ and $G_R(\omega)$, we can simply replace $i\omega_n$ in Eq. A.1f with $\omega + i\eta$ in which η is positive infinitesimal. Using the following equality,

$$\lim_{\eta \rightarrow 0^+} \frac{1}{\omega + i\eta} = 1/\omega - \pi i\delta(\omega) \quad (\text{A.4})$$

we finally prove the mathematical form of the 2nd order Feynman diagram of

phonon-phonon interactions as presented in Eq. 4.4(a) and (d), which correspond to the energy shift and broadening respectively. We can use the same mathematical manipulation to calculate other diagrams. In particular, that the other two lowest order diagrams in Fig. 1.2 have no phonon lifetime broadening is because these terms turn out to have no ω_n dependence by the end and hence no imaginary part when doing the analytical continuation.

Appendix B

The Correlation method: an example for Ag_2O with curprite structure

Essentially, we are using the character table to transform the symmetry group representation from its natural atomic coordinate basis to its normal basis. Following Eq. 2.31 and the theory discussed in Section 2.1.3.3, we will provide an example showing how to derive the group correlation and the selection rule, and the only tool we need is a character table of point groups that can be found in most books about group theory.

As described in Section 2.1.3.3, we need to establish the correlation between the site group and the factor group by comparing the characters in both groups. Consider first the four equivalent Ag atoms. The D_{3d} sites accommodate four atoms and it can be shown that Ag atoms are indeed on sites of D_{3d} symmetry. Similarly, we can find that the two O atoms are on sites of T_d symmetry. Since cuprite structure belongs to the space group O_h^4 , and for the first order Raman scattering, the factor group inherits the full symmetry of the space group, we therefore need to establish the correlation between the site groups D_{3d} , T_d and the factor group O_h .

Let's correlate D_{3d} with O_h first. To do this, we need compare the characters of the operations common to both groups, and find the representations (or modes in the language of lattice dynamics) of both groups having the same characters. We can simply write the partial character table of factor group O_h , including only the operations common to both D_{3d} and O_h . As shown in Table B.1, the irreducible

Table B.1: Derivation of the correlation table between point group O_h and D_{3d} .

O_h	E	$2C_3$	$2C_2$	i	$2S_6$	$3\sigma_d$	D_{3d}
A_{1g}	1	1	1	1	1	1	A_{1g}
A_{2g}	1	1	-1	1	1	-1	A_{2g}
E_g	2	-1	0	2	-1	0	E_g
F_{1g}	3	0	-1	3	0	-1	$A_{2g} + E_g$
F_{2g}	3	0	1	3	0	1	$A_{1g} + E_g$
A_{1u}	1	1	1	-1	-1	-1	A_{1u}
A_{2u}	1	1	-1	-1	-1	1	A_{2u}
E_u	2	-1	0	-2	1	0	E_u
F_{1u}	3	0	-1	-3	0	1	$A_{2u} + E_u$
F_{2u}	3	0	1	-3	0	-1	$A_{1u} + E_u$

Table B.2: Derivation of the correlation table between point group O_h and T_d .

O_h	E	$8C_3$	$3C_2'$	$6S_4$	$6\sigma_d$	T_d
A_{1g}	1	1	1	1	1	A_1
A_{2g}	1	1	1	-1	-1	A_2
E_g	2	-1	2	0	0	E
F_{1g}	3	0	-1	1	-1	F_1
F_{2g}	3	0	-1	-1	1	F_2
A_{1u}	1	1	1	-1	-1	A_2
A_{2u}	1	1	1	1	1	A_1
E_u	2	-1	2	0	0	E
F_{1u}	3	0	-1	-1	1	F_2
F_{2u}	3	0	-1	1	-1	F_1

representations of both groups have been successfully correlated according to their characters. Adopting the same method, we can also correlate T_d with O_h , and the corresponding correlation table is shown in Table B.2.

After obtaining the correlation, the next step is to pick up those representations from the site group with translational symmetry, i.e., the representations have the basis vectors x, y, z , or equivalently, have the translation tensor operators T_x, T_y, T_z . These representations can be easily identified, for example, by comparing their characters with those of the site group representations with basis x, y, z . As listed in the left sides of Table B.3 and B.4, the corresponding representations of cuprite

Table B.3: Irreducible representation of Ag atoms

Site Group D_{3d}		\Rightarrow	Factor Group D_h	
irr. reps.	trans. type		irr. reps.	degeneracy
A_{2u}	T_z		A_{2u}	1
			F_{1u}	3
E_u	(T_x, T_y)		F_{1u}	3
			E_u	2
			F_{2u}	3

Table B.4: Irreducible representation of O atoms

Site Group T_d		\Rightarrow	Factor Group D_h	
irr. reps.	trans. type		irr. reps.	degeneracy
F_2	(T_x, T_y, T_z)		F_{1u}	3
			F_{2g}	3

structures have been identified. Then we can use the correlation tables that we just built up to map these site group representations to the factor group, which is straightforward at this point. The only issue here is to adjust the number of each factor group representations to maintain the degrees of freedom. Take the Ag atom for example, the degrees of freedom from the site group is simply 4 atoms (per unit cell) times 3 translational degrees of freedom and is hence equal to 12. On the right hand side, evidently, the mode degeneracy times the number of corresponding mode also sum up to 12.

The acoustic modes are also included in this irreducible representation. The acoustic modes are readily identifiable in factor group because they correspond to the translational motions of the system. Therefore we can identify them in exactly the same way as we do for the site group representations with translational symmetry. When we consider only those vibrations at the Γ point, the three acoustic modes are of no physical interest, we can therefore subtract them from the irreducible representation. Finally, we obtain the irreducible representation of Ag_2O

with cuprite structure as follows:

$$\Gamma^{Ag_2O} = \Gamma^{Ag} + \Gamma^O - \Gamma^{acoust} \quad (\text{B.1})$$

$$= (A_{2u} + E_u + 2F_{1u} + F_{2u}) + (F_{1u} + F_{2g}) - F_{1u} \quad (\text{B.2})$$

$$= A_{2u} + E_u + 2F_{1u} + F_{2u} + F_{2g} \quad (\text{B.3})$$

At this point, we just need to apply the **Selection Rule 2**: A mode s is Raman active only if the normal coordinate Q_s transforms in the same way as one of the polarizability tensor components $\alpha_{\mu\nu}$, or equivalently, in the same way as x^2, y^2, z^2, xy, yz or zx . This is easy to accomplish by checking the corresponding characters (the same method as being used for identifying the translational symmetry described above). Actually in some professional handbooks [9, 10], this information is explicitly provided along the character table. We find only mode F_{2g} , a triply degenerate mode, contains the polarizability tensor component and therefore is Raman active. Similarly, we find mode F_{1u} is infrared active because it transforms in the same way as T_x, T_y, T_z . The corresponding eigenvectors can be derived by using the group projection operator as discussed in Section 2.1.3.3. The displacement patterns of the normal modes in this example can be found in Chapter 6.

Appendix C

Raman spectra of two-phase and solid solution phase of $\text{Li}_{0.6}\text{FePO}_4$ at elevated temperatures

Over the past decade, phosphate-based olivine materials have attracted great research interest as a new class of cathods for lithium-ion rechargeable batteries. In particular, with the flat discharge voltage of 3.5 V, a theoretical specific capacity of 169 mAh/g and the environmentally friendly constituents, LiFePO_4 has been the focus of much of this research [148,149]. The electrochemical properties of LiFePO_4 are limited by a low intrinsic electronic conductivity, and efforts are being made to improve this feature [150,151]. The Raman scattering technique clearly represents a suitable way to investigate the dynamic properties of this material. Although it is not the focus of the study presented in this thesis, the data we obtained are interesting and informative for reference and further study.

In particular, Fig. 1 shows the Raman spectra at elevated temperatures of $\text{Li}_{0.6}\text{FePO}_4$. The Raman spectra for the two-phase compound ($\text{LiFePO}_4 + \text{FePO}_4$ with phase boundary) show clear evidences of phase transition from the two-phase to the solid solution above 230 °C. As shown in the figure, the sharp Raman lines diminished at 230 °C, caused by a diffusion transfer of lithium ions across the phase boundary of LiFePO_4 and FePO_4 . Fig. 2 shows evidences that the transition from the two-phase to the solid solution phase may involve some slow kinetic processes. Compared with a short heat time (40 mins, 2 hrs and 40 mins), the spectra at long

heating time (5 hrs and 40 mins) shows additional energy broadening and shift features.

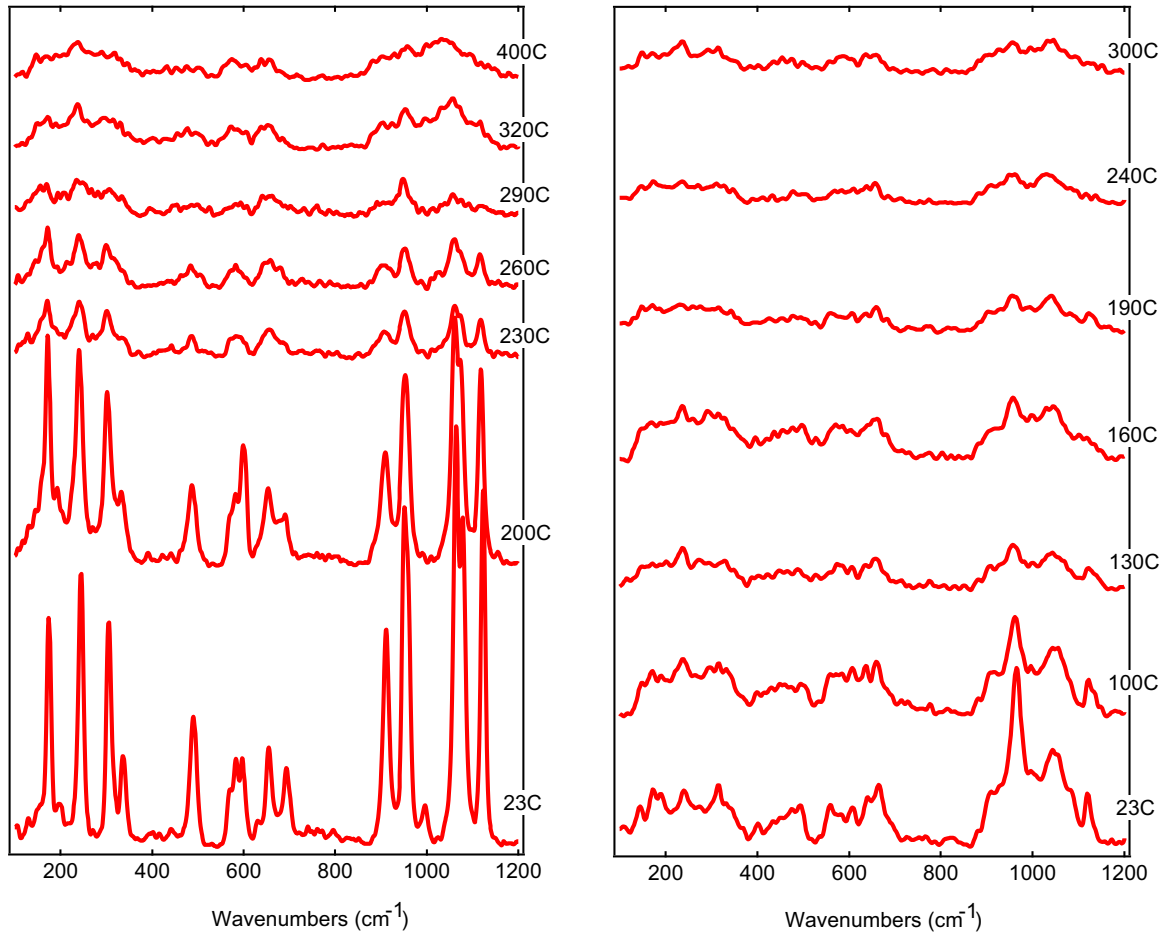


Figure C.1: Raman spectra at elevated temperatures of two-phase $\text{Li}_{0.6}\text{FePO}_4$ (left panel) and solid solution phase quenched at 400 °C(right panel)

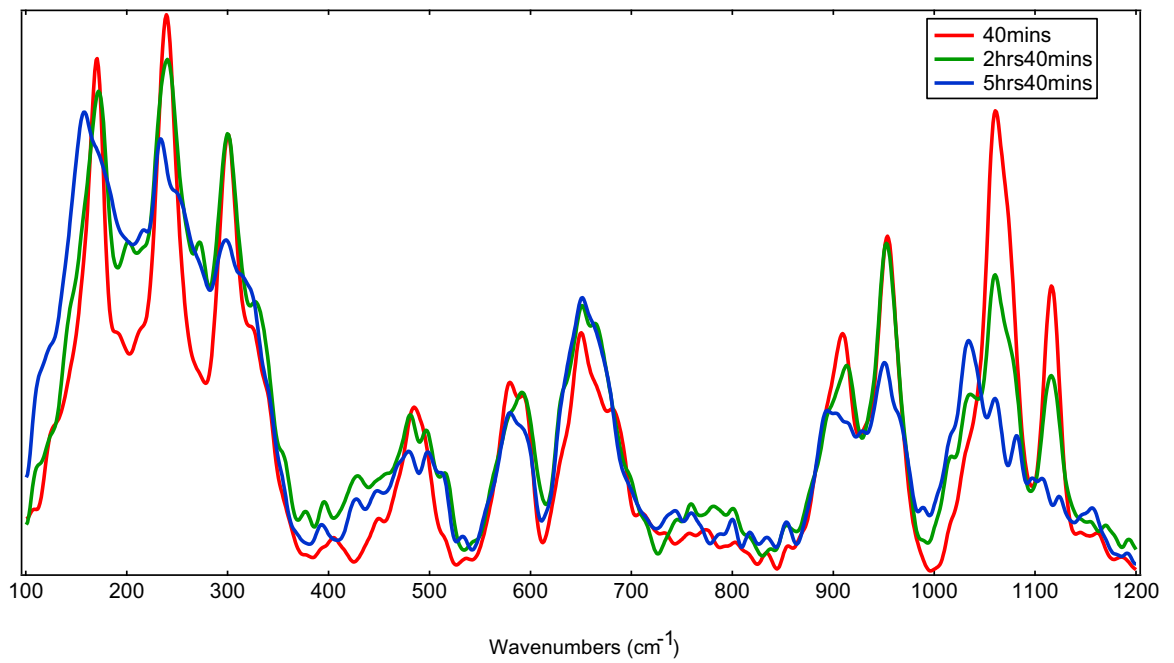


Figure C.2: Raman spectra of two-phase $\text{Li}_{0.6}\text{FePO}_4$ right above the phase transition temperature at $260\text{ }^\circ\text{C}$ but with different heating times.

Bibliography

- [1] A. L. Fetter and J. D. Walecka. *Quantum theory of many particle systems*. Dover, 2003.
- [2] A. A. Maradudin and A. E. Fein. *Phys. Rev.*, 128:2589, 1962.
- [3] J. A. Reissland. *The Physics of Phonons*. John Wiley and Sons LTD, 1973.
- [4] P. Souvatzis, O. Eriksson, M. I. Katsnelson, and S. P. Rudin. *Phys. Rev. Lett.*, 100:095901, 2008.
- [5] O. Hellman, I. A. Abrikosov, and S. I. Simak. *Phys. Rev. B*, 84:180301, 2011.
- [6] R. Loudon. *Advances in Physics*, 13(52):423, 1964.
- [7] A. Compaan and H. Z. Cummins. *Phys. Rev. Lett.*, 31:41, 1973.
- [8] P. Y. Yu and Shen. Y. R. *Phys. Rev. Lett.*, 32:373, 1974.
- [9] T. Inui, Y. Tanabe, and Y. Onodera. *Group theory and its applications in physics*. Springer, 1996.
- [10] W. G. Fately, R. R. Dollish, N. T. McDevitt, and F. F. Bentley. *Infrared and Raman Selection Rules for Molecular and Lattice Vibrations*. John Wiley and Sons, 1972.
- [11] P. Brüesch. *Phonons: Theory and Experiments*. Springer-Verlag, 1982.
- [12] W. L. Chen. *Phonon Anharmonicity of Ionic Compounds and Metals*. PhD thesis, California Institute of Technology, 2012.

- [13] D. L. Abernathy, M. B. Stone, M. J. Loguillo, M. S. Lucas, O. Delaire, X. Tang, J. Y. Y. Lin, and B. Fultz. *Rev. Sci. Instrum.*, 83(1):015114, 2012.
- [14] M. G. Kresch. *Temperature Dependence of Phonons in Elemental Cubic Metals Studied by Inelastic Scattering of Neutrons and X-Rays*. PhD thesis, California Institute of Technology, 2009.
- [15] B. Fultz, T. Kelley, J. Lin, J. Lee, O. Delaire, M. Kresch, M. McKerns, and M. Aivazis. *Experimental inelastic neutron scattering: Introduction to DANSE*, <http://docs.danse.us>. 2009.
- [16] P. Hohenberg and W. Kohn. *Phys. Rev.*, 136:864, 1964.
- [17] W. Kohn and L. J. Sham. *Phys. Rev.*, 140:1133, 1965.
- [18] R. M. Martin. *Electronic Structure: Basic Theory and Practical Methods*. Cambridge University Press, 2008.
- [19] D. M. Ceperley and B. J. Alder. *Phys. Rev. Lett.*, 45:566, 1980.
- [20] J. P. Perdew and A. Zunger. *Phys. Rev. B*, 23:5048, 1981.
- [21] J. P. Perdew and Y. Wang. *Phys. Rev. B*, 45:13244, 1992.
- [22] J. P. Perdew, K. Burke, and M. Ernzerhof. *Phys. Rev. Lett.*, 77:3865, 1996.
- [23] J. C. Slater. *Phys. Rev.*, 51:846, 1937.
- [24] F. Herman. *Rev. Mod. Phys.*, 30:102, 1958.
- [25] D. R. Hamann, M. Schlüter, and C. Chiang. *Phys. Rev. Lett.*, 43:1494, 1979.
- [26] D. Vanderbilt. *Phys. Rev. B*, 41:7892, 1990.
- [27] P. E. Blöchl. *Phys. Rev. B*, 50:17953, 1994.
- [28] G. Kresse and D. Joubert. *Phys. Rev. B*, 59:1758, 1999.

- [29] D. Marx and J. J. Hutter. *Ab Initio Molecular Dynamics: Basic Theory and Advanced Methods*. Cambridge University Press, 2009.
- [30] F. Jensen. *Introduction to Computational Chemistry*. Wiley, 2007.
- [31] M. Griebel. *Numerical Simulation in Molecular Dynamics*. 2007.
- [32] J. A. Morrone and R. Car. *Phys. Rev. Lett.*, 101:017801, 2008.
- [33] L. Lin, J. A. Morrone, R. Car, and M. Parrinello. *Phys. Rev. Lett.*, 105:110602, 2010.
- [34] R. Car and M. Parrinello. *Phys. Rev. Lett.*, 55:2471, 1985.
- [35] L. Verlet. *Phys. Rev.*, 159:98, 1967.
- [36] H. C. Anderson. *J. Chem. Phys.*, 72:2384, 1980.
- [37] S. Nosé. *Mol. Phys.*, 52:255, 1984.
- [38] W. G. Hoover. *Phys. Rev. A*, 31:1695, 1985.
- [39] P. Giannozzi, S. Baroni, N. Bonini, M. Calandra, R. Car, C. Cavazzoni, D. Ceresoli, G. L. Chiarotti, M. Cococcioni, I. Dabo, A. Dal Corso, S. de Gironcoli, S. Fabris, G. Fratesi, R. Gebauer, U. Gerstmann, C. Gougoussis, A. Kokalj, M. Lazzeri, L. Martin-Samos, N. Marzari, F. Mauri, R. Mazzarello, S. Paolini, A. Pasquarello, L. Paulatto, C. Sbraccia, S. Scandolo, G. Sclauzero, A. P. Seitsonen, A. Smogunov, P. Umari, and R. M. Wentzcovitch. *J. Phys.: Condens. Matter.*, 21:395502, 2009.
- [40] S. Baroni, S. de Gironcoli, A. Dal Corso, and P. Giannozzi. *Rev. Mod. Phys.*, 73:515–562, Jul 2001.
- [41] M. S. Green. *J. Chem. Phys.*, 22:398, 1954.
- [42] R. Kubo. *J. Phys. Soc. Jpn.*, 12:570, 1957.

- [43] D. W. Noid, M. L. Koszykowski, and R. A. Marcus. *J. Chem. Phys.*, 67:404, 1977.
- [44] S-T Lin, M. Blanco, and W. A. Goddard. *J. Chem. Phys.*, 119:11792, 2003.
- [45] N. de Koker. *Phys. Rev. Lett.*, 103:125902, 2009.
- [46] I. P. Ipatova, A. A. Maradudin, and R. F. Wallis. *Phys. Rev.*, 155:882–895, 1967.
- [47] X. Tang, C. W. Li, and B. Fultz. *Phys. Rev. B*, 82:184301, Nov 2010.
- [48] X. Tang and B. Fultz. *Phys. Rev. B*, 84:054303, Aug 2011.
- [49] A. L. Linsebigler, G. Lu, and J. T. Yates. catalyst review. *Chem. Rev.*, 95:735, 1995.
- [50] U. G. Akpan and B. H. Hameed. *Appl. Catal. A-Gen.*, 375:1, 2010.
- [51] Y. Du, N. A. Deskins, Z. Zhang, Z. Dohnálek, M. Dupuis, and I. Lyubinetsky. *Phys. Rev. Lett.*, 102:096102, Mar 2009.
- [52] B. O'Regan and M. Grätzel. *Nature(London)*, 353:737, 1991.
- [53] U. Diebold. *Surf. Sci. Rep.*, 48:53, 2003.
- [54] P. Balaya. *Energy Environ. Sci.*, 1(6):645–654, 2008.
- [55] M. K. Nowotny, L. R. Sheppard, T. Bak, and J. Nowotny. *J. Phys. Chem. C*, 112:5275, 2008.
- [56] D. G. Isaak, J. D. Carnes, O. L. Anderson, H. Cynn, and E. Hake. *Phys. Chem. Minerals*, 26:31, 1998.
- [57] P. S. Narayanan. *Proc. Indian Acad. Sci. Sect. A*, 32:279, 1950.
- [58] S. P. S. Porto, P. A. Fleury, and T. C. Damen. *Phys. Rev.*, 154(2):522, 1967.
- [59] G. A. Samara and P. S. Percy. *Phys. Rev. B*, 7(3):1131–1148, 1973.

- [60] U. Balachandran and N. G. Eror. *J. Solid State Chem.*, 42:276, 1982.
- [61] L. G. Liu and T. P. Mernagh. *Eur. J. Mineral.*, 4:45, 1992.
- [62] H. Chang and P. Huang. *J. Raman Spectrosc.*, 29:97, 1998.
- [63] W. Zhang, Y. He, M. Zhang, Z. Yin, and Q. Chen. *J. Phys. D: Appl. Phys.*, 33:912, 2000.
- [64] X. Feng, Y. Guo, J. Chen, and J. Zhang. *J. Biomater. Sci.-Polym. Ed.*, 18:1443, 2007.
- [65] P. S. Peercy and B. Morosin. *Phys. Rev. B*, 7(6):2779, 1972.
- [66] J. Pascual, J. Camassel, P. Merle, B. Gil, and H. Mathieu. *Phys. Rev. B*, 24:2101–2108, Aug 1981.
- [67] A. Perakis, E. Sarantopoulou, Y. S. Raptis, and C. Raptis. *Phys. Rev. B*, 59(2):775–782, 1999.
- [68] D. J. Lockwood, R. S. Katiyar, and V. C. Y. So. *Phys. Rev. B*, 28:1983–1987, Aug 1983.
- [69] P. S. Peercy. *Phys. Rev. B*, 8:6018–6020, Dec 1973.
- [70] B. Montanari and N. M. Harrison. *J. Phys.: Condens. Matter*, 16:273, 2004.
- [71] P. D. Mitev, K. Hermansson, B. Montanari, and K. Refson. *Phys. Rev. B*, 81:134303, 2010.
- [72] J. A. Thomas, J. E. Turney, R. M. Iutzi, C. H. Amon, and A. J. H. McGaughey. *Phys. Rev. B*, 81:081411, 2010.
- [73] G. Kopidakis, C. Z. Wang, C. M. Soukoulis, and K. M. Ho. *J. Phys.: Condens. Matter*, 9:7071, 1997.
- [74] C. W. Li, M. M. McKerns, and B. Fultz. *Phys. Rev. B*, 80:054304, 2009.

- [75] J. D. Gale and A. L. Rohl. *Mol. Simul.*, 29:291, 2003.
- [76] M. Matsui and M. Akaogi. *Mol. Simul.*, 6:239, 1991.
- [77] V. Swamy and J. D. Gale. *Phys. Rev. B*, 62:5406–5412, Sep 2000.
- [78] G. C. Mather, M. S. Islam, and F. M. Figueiredo. *Adv. Func. Mater.*, 17:905, 2007.
- [79] M. Mostoller and J. C. Wang. *Phys. Rev. B*, 32:6773–6786, Nov 1985.
- [80] C. Z. Wang, C. T. Chan, and K. M. Ho. *Phys. Rev. B*, 42:11276–11283, Dec 1990.
- [81] J. Menéndez and M. Cardona. *Phys. Rev. B*, 29:2051–2059, Feb 1984.
- [82] C. M. B Henderson, K. S Knight, and A. R. Lennie. *Open Mineral.J.*, 3:1, 2009.
- [83] J. L. Feldman, L. L. Boyer, P. J. Edwardson, and J. Hardy. *Phys. Rev. B*, 40:4105–4118, Aug 1989.
- [84] E. Liarokapis, E. Anastassakis, and G. A. Kourouklis. *Phys. Rev. B*, 32(12):8346–8355, 1985.
- [85] K. Nishidate and T. Sato. *Phys. Rev. B*, 46:13773–13778, Dec 1992.
- [86] J. Suda and T. Sato. *J Phys. Soc. Japan*, 66:1707, 1996.
- [87] P. G. Klemens. *Phys. Rev.*, 148(2):845, 1966.
- [88] M. Balkanski, R. F Wallis, and E. Haro. *Phys. Rev. B*, 28(4):1928, 1983.
- [89] G. D. Barrera, J. A. O. Bruno, T. H. K. Barron, and N. L. Allan. *J. Phys.: Condens. Matter*, 17:217, 2005.
- [90] J. A. O. Bruno, N. L. Allan, T. H. K. Barron, and A. D. Turner. *Phys. Rev. B*, 58:8416–8427, Oct 1998.
- [91] R. Mittal, S. L. Chaplot, S. K. Mishra, and Preyoshi P. Bose. *Phys. Rev. B*, 75:174303, May 2007.

- [92] P. Merle, J. Pascual, J. Camassel, and H. Mathieu. *Phys. Rev. B*, 21:1617–1626, Feb 1980.
- [93] B. Fultz. *Prog. Mater. Sci.*, 55:247, 2010.
- [94] D. C. Wallace. *Thermodynamics of Crystals*. Dover Publications, Inc, 1998.
- [95] S. J. Smith, R. Stevens, S. Liu, G. Li, A. Navrotsky, J. Boerio-Goates, and B. F. Woodfield. *Am. Miner.*, 94:236, 2009.
- [96] M. Batzill and U. Diebold. *Prog. Surf. Sci.*, 79(2-4):47–154, 2005.
- [97] R. S. Katiyar, P. Dawson, M. M. Hargreave, and G. R. Wilkinson. *J. Phys. C: Solid St. Phys.*, 4:2421, 1971.
- [98] H. Hellwig, A. F. Goncharov, E. Gregoryanz, H-K Mao, and R. J. Hemley. *Phys. Rev. B*, 67:174110, May 2003.
- [99] T. Livneh, Y. Lilach, I. Popov, A. Kolmakov, and M. Moskovits. *J. Phys. Chem. C*, 115:17270, 2011.
- [100] A. Diéguez, A. Romano-Rodríguez, A. Vilà, and J. R. Morante. *J. Appl. Phys.*, 90(3):1550–1557, 2001.
- [101] F. Gervais and W. Kress. *Phys. Rev. B*, 31:4809–4814, Apr 1985.
- [102] T. Sato and T. Asari. *J. Phys. Soc. Japan*, 64:1193, 1995.
- [103] K. Parlinski and Y. Kawazoe. *Eur. Phys. J. B*, 13:679, 2000.
- [104] H. W. Leite Alves, C. C. Silva, A. T. Lino, P. D. Borges, L. M. R. Scolfaro, and E. F. da Silva, Jr. *Appl. Surf. Sci.*, 255(3):752–754, 2008.
- [105] P. D. Borges, L. M. R. Scolfaro, H. W. Leite Alves, and E. F. da Silva, Jr. *Theor. Chem. Acc.*, 126:39–44, 2010.
- [106] T. Lan, X. Tang, and B. Fultz. *Phys. Rev. B*, 85:094305, 2012.

- [107] D. Wang, B. Chen, and J. Zhao. *J. Appl.Phys.*, 101(11):113501, 2007.
- [108] J. F. Mammone, M. Nicol, and S. K. Sharma. *J. Phys. Chem. Solids*, 42:379, 1981.
- [109] A. Debernardi. *Phys. Rev. B*, 57:12847, 1998.
- [110] G. Deinzer, G. Birner, and D. Strauch. *Phys. Rev. B*, 67:144304, 2003.
- [111] W. Tiano, M. Dapiaggi, and G Artioli. *J. Appl. Crystallogr.*, 36:1461, 2003.
- [112] B. J. Kennedy, Y. Kubota, and K. Kato. *Solid State Commun.*, 136:177, 2005.
- [113] S. Bhattacharya and A. Ghosh. *Solid State Ionics*, 161:61, 2003.
- [114] T. Minami. *J. Non-Crys. Solids*, 56:15, 1983.
- [115] W-X Li, C. Stampfl, and M. Scheffler. *Phys. Rev. Lett.*, 90:256102, 2003.
- [116] L. Gou and C. Murphy. *Nano Lett.*, 3:231, 2003.
- [117] A. K. A. Pryde, K. D. Hammonds, M. T. Dove, V. Heine, J. D. Gale, and M. C. Warren. *J. Phys.-Condens. Matter*, 8(50):10973–10982, 1996.
- [118] V. Heine, P. R. L. Welche, and M. T. Dove. *J. Am. Ceram. Soc.*, 82:1793, 1999.
- [119] C. W. Li, X. Tang, J. A. Muñoz, J. B. Keith, S. J. Tracy, D. L. Abernathy, and B. Fultz. *Phys. Rev. Lett.*, 107(19):195504, NOV 4 2011.
- [120] S. a Beccara, G. Dalba, P. Fornasini, R. Grisenti, A. Sanson, and F. Rocca. *Phys. Rev. Lett.*, 89:025503, Jun 2002.
- [121] A. Sanson, F. Rocca, G. Dalba, P. Fornasini, R. Grisenti, M. Dapiaggi, and G. Artioli. *Phys. Rev. B*, 73:214305, Jun 2006.
- [122] K. W. Chapman and P. J. Chupas. *Chem. Mater.*, 21:425, 2009.
- [123] M. Dapiaggi, H. Kim, Emil S. Bozin, S. J. L. Billinge, and G. Artioli. *J. Phys. Chem. Solids*, 69:2182, 2008.

- [124] P. Souvatzis, O. Eriksson, M. I. Katsnelson, and S. P. Rudin. *Phys. Rev. Lett.*, 100:095901, 2008.
- [125] N. Antolin, O. D. Restrepo, and W. Windl. *Phys. Rev. B*, 86:054119, 2012.
- [126] M. K. Gupta, R. Mittal, S. Rols, and S. L. Chaplot. *Physica B*, 407:2146, 2012.
- [127] A. Sanson. *Solid State Commun.*, 151:1452, 2011.
- [128] R. Mittal, S. L. Chaplot, S. K. Mishra, and Preyoshi P. Bose. *Phys. Rev. B*, 75:174303, 2007.
- [129] V. Gava, A. L. Martinotto, and C. A. Perottoni. *Phys. Rev. Lett.*, 109:195503, 2012.
- [130] A. Putrino and M. Parrinello. Anharmonic raman spectra in high-pressure ice from *Ab Initio* simulations. *Phys. Rev. Lett.*, 88:176401, 2002.
- [131] T. Lan, X. Tang, and B. Fultz. *Phys. Rev. B*, 85:094305, 2012.
- [132] K. S. Pitzer and W. V. Smith. *J. Am. Chem. Soc.*, 59:2633, 1937.
- [133] M. Kresch, M. Lucas, O. Delaire, J. Y. Lin, and B. Fultz. *Phys. Rev. B*, 77:024301, 2008.
- [134] G. I. N. Waterhouse, G. A. Bowmaker, and J. B. Metson. *Phys. Chem. Chem. Phys.*, 3:3838, 2001.
- [135] G. Kresse and J. Furthmüller. *Comput. Mater. Sci.*, 6:15, 1996.
- [136] G. Kresse and J. J. Hafner. *Phys. Rev. B*, 47:558, 1993.
- [137] G. Kresse and J. Furthmüller. *Phys. Rev. B*, 54:11169–11186, 1996.
- [138] D. P. Sellan, E. S. Landry, J. E. Turney, A. J. H. McGaughey, and C. H. Amon. *Phys. Rev. B*, 81:214305, 2010.
- [139] A. Togo, F. Oba, and I. Tanaka. *Phys. Rev. B*, 78:134106, Oct 2008.

- [140] P. H. Berens, D. H. J. Mackay, G. M. White, and K. R. Wilson. *J. Chem. Phys.*, 79:2375, 1983.
- [141] F. I. Kreingol'd and B. S. Kulinkin. *Soviet Phys.- Semicond.*, 4:2022, 1970.
- [142] Alberto Debernardi, Stefano Baroni, and Elisa Molinari. *Phys. Rev. Lett.*, 75:1819–1822, 1995.
- [143] T. Lan, C. W. Li, and B. Fultz. *Phys. Rev. B*, 86:134302, 2012.
- [144] A. Sanson. *Solid State Sciences*, 11:1489, 2009.
- [145] F. Labat, P. Baranek, C. Domain, C. Minot, and C. Adamo. *J. Chem. Phys.*, 126:154703, 2007.
- [146] T. Lan, C. W. Li, J. L. Niedziela, H. Smith, D. L. Abernathy, G. R. Rossman, and B. Fultz. *Phys. Rev. B*, 89:054306, 2014.
- [147] J. Callaway. *Phys. Rev.*, 113:1046, 1959.
- [148] A. K. Padhi, K. S. Nanjundaswami, and J. B. Goodenough. *J. Electrochem. Soc.*, 144:1188, 1997.
- [149] C. M. Burba and R. Frech. *J. Electrochem. Soc.*, 151:A1032, 2004.
- [150] C. Delacourt, C. Wurm, L. Laffont, J. B. Leriche, and C. Masquelier. *Solid State Ionics*, 177:333, 2006.
- [151] C. Lu, G. T. Fey, and H. Kao. *J. Power Sources*, 189:155, 2009.